Spectroscopic modeling of oscillating Algol-type stars

Dissertation
zur Erlangung des akademischen Grades
Dr. rer. nat.

vorgelegt dem Rat der Physikalisch-Astronomischen Fakultät
der Friedrich-Schiller-Universität Jena

eingereicht von M. Sc. Andrii Tkachenko
geboren am 03.09.1985 in Simferopol (Ukraine)

Gutachter

1. Prof. Dr. Artie P. Hatzes
Direktor
Thüringer Landessternwarte Tautenburg
Sternwarte 5
D - 07778 Tautenburg
Phone: +49 36427 863 51
Fax: +49 36427 863 29
E-mail: artie@tls-tautenburg.de

2. Prof. Dr. Ulrich Heber
Direktor
Dr. Remeis-Sternwarte Bamberg
Sternwartstrasse 7
D - 96049 Bamberg
Phone: +49 951 95222 14
Fax: +49 951 95222 22
E-mail: ulrich.heber@sternwarte.uni-erlangen.de

3. Prof. i. R. Dr. Werner Weiss
Institut für Astronomie der Universität Wien
Türkenschanzstraße 17 (Sternwarte)
1180 Wien
Phone: +43 1 4277 518 70
Fax: +43 1 4277 9 538
E-mail: werner.weiss@univie.ac.at

Tag der Disputation: 02.11.2010

Zusammenfassung

Das Ziel dieser Arbeit ist die Erstellung eines Computerprogramms, welches Zeitserien von hochaufgelösten Spektren spektroskopischer, bedeckungsveränderlicher Doppelsterne analysiert, um deren Systemparameter und die Sternparameter der Komponenten abzuleiten sowie die Anwendung dieses Programms auf Spektren von oEA Sternen, welche zu einer neuentdeckten Gruppe pulsierender Veränderlicher gehören. Die Mitglieder dieser Gruppe sind Masse akkredierende Algolsterne, deren Hauptkomponenten nichtradiale Pulsationen vom δ Scuti Typ zeigen. Die oEA Sterne sind von außergewöhnlicher Bedeutung für asteroseismologische Studien. Ihre Untersuchung kann die Grundprinzipien der Wechselwirkung zwischen dem magnetischen Aktivitätszyklus der kühlen Sekundärkomponente (Begleiter), dem Auftreten von Phasen starken Masseaustauschs und der Anregung verschiedener Pulsationsmoden des Hauptsterns aufdecken. Ausserdem wirkt der Begleiter während der Bedeckungsphasen als zeitlich variabler Raumfilter und erzeugt damit, in Abhängigkeit von der Art der beobachteten Pulsationsmoden, charakteristische Amplituden- und Phasenmodulationen der Helligkeits- und Linienprofilvariationen.

Für die asteroseismologische Modellierung eines Sterns ist neben einer eindeutigen Identifizierung der Pulsationsmoden in Form ihrer Wellenzahlen auch die Kenntnis präziser Werte der grundlegenden Sternparameter erforderlich. Aktuell gibt es aber einen Mangel an Programmen welche in der Lage sind, diese aus der Spektroskopie der Objekte abzuleiten. Aus diesem Grund haben wir das Rechnerprogramm Shellspec07_inverse entwickelt. Es löst das inverse Problem der Bestimmung der System- und Sternparameter bedeckungsveränderlicher Doppelsterne aus den beobachteten Linienprofilen, welche aus allen Bahnphasen inklusive der Bedeckungen stammen können. Das Programm basiert auf einer schnellen Variante des Levenberg-Marquardt Algorithmus zur nichtlinearen Optimierung, berücksichtigt die nichtsphärische Konfiguration des kühlen Begleiters und nutzt verbesserte Routinen zur Berechnung der Schwere- und Randverdunklungseffekte.

Es werden Zeitserien von Spektren der zwei oEA Sterne RZ Cas und TW Dra analysiert. Wir verwenden dabei das KOREL Programm zur Ableitung präziser Bahnlösungen und zur Trennung der Kompositspektren in die Einzelspektren der Doppelsternkomponenten, das SynthV Programm, um die chemischen Häufigkeiten auf den Sternoberflächen aus den getrennten Spektren zu bestimmen, sowie das neuentwickelte Shellspec07_inverse Programm für eine Feinbestimmung der System- und Sternparameter und um in den Residuen der erhaltenen Lösungen nach dem Einfluss Algol-typischer Effekte zu suchen. Indem wir die getrennten Spektren von TW Dra mit Spektren aus den Bedeckungsphasen vergleichen, können wir zum ersten Mal wirklich beweisen, dass das KOREL Programm zuverlässige Einzelspektren der Komponenten von Mehrfachsystemen liefert.

Die mit Shellspec07_inverse erhaltenen Ergebnisse zeigen, dass es möglich ist, die Parameter der untersuchten Systeme mit einer Genauigkeit zu bestimmen, welche mit der aus der Lichtkurvenanalyse erhaltenen vergleichbar ist. Die Hauptkompenten beider oEA Sterne sind normale Hauptreihensterne vom Spektraltyp A. Die meisten der abgeleiteten Parameter stimmen mit den bekannten photometrischen Werten überein. Lediglich für die Temperatur des Begleiters von RZ Cas erhalten wir einen signifikant höheren Wert, bedingt durch die ungewöhnliche Helligkeitsverteilung auf seiner Oberfläche. Aus den Ergebnissen kann auf die Existenz eines grossen dunklen Flecks geschlossen werden, welcher in Richtung der Hauptkomponente zeigt und wahrscheinlich durch einen Kühlungsmechanismus verursacht wird, der durch den Enthalpietransport über den inneren Lagrangepunkt ausgelöst wird. Der Hauptstern von RZ Cas rotiert synchron zur Bahnbewegung, während der Hauptstern von TW Dra um einen Faktor 1.07 schneller als synchron rotiert.

Beide Sterne wurden in zwei unterschiedlichen Epochen beobachtet. TW Dra konnte aufgrund der in 2007 als auch in 2008 erhaltenen Spektren sehr gut modelliert werden ohne Algol-typische Effekte wie einen Gasstrom oder einen Akkretionsring zu berücksichtigen. Dies trifft auch auf die Beobachtungen von RZ Cas in 2006 zu, während die Residuen der Modellrechnungen für das Jahr 2001 komplexe Strukturen zeigen und auf eine Phase starken Masseaustauschs verweisen. Diese Annahme wird durch die zwischen 2001 und 2006 beobachtete Zunahme der Bahnperiode um 2 Sekunden unterstützt, welche durch einen Drehimpulsaustausch zwischen der beschleunigten Rotation der äußeren Schichten der Hauptkomponente und der Bahnbewegung erklärt werden kann.

Ein erster Versuch, die Berechnung der aus den nichtradialen Pulsationen resultierenden Linienprofilvariationen in das Shellspec07_inverse Programm zu intergieren, ergab ermutigende Resultate. Wir konnten allgemeingültige Zusammenhänge zwischen der Neigung der Rotationsachse der Sterne und den beobachteten Amplituden der Radialgeschwindigkeitsvariationen in Abhängigkeit von der Art der Pulsationsmoden ableiten und zeigen, dass diese Amplituden während der Bedeckung deutlich verstärkt werden. Die ermittelten Verstärkungsfaktoren können in Zukunft zusammen mit der Entdeckung, dass die sektoralen Moden wärend der Bedeckung ein spezielles Verhalten zeigen, welches sie von allen anderen Moden unterscheidet, für eine Modenidentifizierung verwendet werden, basierend auf Radialgeschwindigkeitsbestimmungen und einer verbesserten Modellierung der Pulsationsmoden.

Abstract

The aim of this thesis is to provide a computer program that is able to analyze time series of high-resolution spectra of double-lined spectroscopic eclipsing binaries to derive the stellar and system parameters of their components and to apply the program to spectra of a relatively new class of pulsating stars, the so-called oEA stars. These are mass accreting, eclipsing binaries of Algol-type with primary components showing δ Scuti-like non-radial pulsations. The oEA stars are outstanding objects for asteroseismic investigations. Their study can reveal basic principles of the interaction between the magnetic activity cycle of the cool secondary, the occurrence of rapid mass transfer episodes, and the excitation of different non-radial pulsation modes of the primary. Moreover, the secondary acts as a spatial filter during the primary eclipse, producing specific amplitude and phase changes in the brightness and line profile variations due to pulsation, in dependence on the observed oscillation modes.

Besides a unique mode identification in terms of wavenumbers, the precise knowledge of basic stellar parameters is needed to establish an asteroseismic model of a star. There is a lack of spectroscopic programs that derive these values, however. For that reason, we established the new computer program Shellspec07_inverse. It solves the inverse problem of finding stellar and system parameters of eclipsing binaries from the composite line profiles observed at all orbital phases including the eclipses. The program uses a fast version of the Levenberg-Marquardt algorithm for the non-linear optimization, counts for the non-spherical shape of the Roche-lobe filling secondary, and uses improved routines to calculate the limb and gravity darkening effects.

We analyzed the spectra of the two oEA stars RZ Cas and TW Dra using the KOREL program to derive precise orbital solutions and to decompose the spectra of the binary components, the SynthV program to derive the elemental abundances of the components from the mean, decomposed spectra, and finally the Shellspec07_inverse program for a fine-tuning of the stellar and system parameters and to look in the residuals of our solutions for the influence of Algol-typical effects. Based on single spectra of TW Dra and its visual companion, we could prove, maybe for the first time, that the KOREL program yields precisely decomposed spectra of the components of multiple systems.

The results obtained with Shellspec07_inverse show that it is possible to derive the stellar and system parameters of the two target stars spectroscopically with an accuracy that is comparable to that obtained from the light curve analysis. We could show that the primaries of both stars are normal main sequence A-type stars of about solar abundances. Most of the deduced parameters agree with the photometrically derived ones. Only for the temperature of the secondary of RZ Cas we obtained a significantly higher value, resulting from its unusual surface temperature distribution. We assume that the secondary of RZ Cas shows a large

dark spot on its surface pointing toward the primary, presumably originating from a cooling mechanism by the enthalpy transport via the inner Lagrangian point. No such effect was observed for TW Dra. The primary of RZ Cas rotates synchronously to the orbital motion, whereas the primary of TW Dra rotates supersynchronously by a factor of 1.07.

Both stars have been observed during two different epochs. In 2007 and 2008, the TW Dra system can be well modeled without including any Algol-typical effects like a gas stream or an accretion annulus into the calculations. We conclude that it was in a quiet state during both years. The same result was obtained for RZ Cas when observed in 2006. The O–C residuals of our solution based on the spectra from 2001 show a complex distribution of circumbinary matter, however, pointing to the occurrence of an episode of rapid mass transfer. This assumption is supported by the deduced change of the orbital period of RZ Cas of 2 seconds between the two epochs of observations that can be explained in terms of angular momentum transfer between the accelerated rotation of the outer layers of the primary and the orbit.

A first attempt to include the calculation of line profile variations due to non-radial pulsations into Shellspec07_inverse gave encouraging results. We could derive some common relationships between the inclination of the rotation axis of the oscillating primary and the amplitudes of the induced radial velocity variations in dependence on the pulsation characteristics and show that the spatial filtration effect amplifies these amplitudes during the eclipses remarkably. The derived amplification factors and the detection that the sectoral modes show a completely different behavior during the eclipses compared to all other modes can be used for a future mode identification based on radial velocity measurements and on an improved treatment of the pulsations in the Shellspec07_inverse program.

Contents

Chapter 1

Introduction

Asteroseismology is one of the most rapidly developing fields in astrophysics. It provides a modern tool to explore the internal structure of the stars by analyzing its oscillations. Further progress can be expected from the actual space satellite missions like CoRoT[1] and Kepler[2]. Whereas it is possible to determine the masses, radii and ages of the stars very precise by asteroseismic methods (Thoul et al. 2003), asteroseismology itself needs some basic knowledge about stellar parameters like temperature, surface gravity, spectral type, or the projected equatorial velocity of rotation to identify the observed non-radial pulsation modes and to model the stellar interiors. In particular the mentioned space satellite missions, which are photometric ones and in the case of the Kepler satellite equipped with a white light detector without the possibility to gather any color information about the observed stars, need additional support by ground based observations. Actually, the derivation of the required parameters is mainly based on multi-color photometry and light curve analysis using the Wilson-Devinney program, and on spectrum analysis making use of the observed line strengths and radial velocities. There have only been very few attempts to use the full information provided by the stellar spectra, however.

This thesis describes the development of a computer program to analyze time series of high-resolution composite spectra of double-lined spectroscopic binaries with the aim to derive optimized values of the stellar and system parameters. The program is applied to a new class of pulsating stars, the so-called oEA stars, i.e. eclipsing Algol-type stars with primary components that show δ Scuti-like non-radial pulsations. In the introduction we focus on the special role of the oEA stars within the multiple and the oscillating stars in general and on the different approaches in photometry and spectroscopy to extract information from the observations.

1.1 Binary stars

The majority of stars in our galaxy are members of multiple systems. The fraction of binary stars, i.e. stellar systems consisting of two components revolving around their common center of mass, is more than 50% in the solar neighborhood. Even the nearest star α Centauri is a binary with a primary component similar to the Sun by its brightness, temperature and

---

[1]http://smsc.cnes.fr/COROT/
[2]http://kepler.nasa.gov/

mass, and a faint, cool, and less massive companion. Sirius, the brightest star in the night sky, is a double star consisting of a main sequence primary and a white dwarf as the secondary component. Binary stars can be classified either by the method of how they are detected or by their physical system configurations. According to the method of detection, one speaks about visual, astrometric, and spectroscopic binaries. A *visual binary* is a binary where the angular separation between the stars is large enough to resolve the system by a telescope into the two components. If one of the components is too faint so that only the other one and its movement around the common center of mass can be observed, the star is called an *astrometric binary*. If the double star cannot be resolved, its duality can still be recognized by spectroscopic methods. This is offered by the fact that the components show periodic Doppler shifts during their revolution around the center of mass moving their spectral lines from blue to red and vice versa. Such binaries are called *spectroscopic binaries*. When the inclination of the orbit is large enough so that the observer sees the components passing in front of each other producing dips in the light curve, the system is called an *eclipsing binary*.

According to the type of the system configuration, binaries are divided into three groups: 1) *detached systems*, where both components do not fill their Roche lobes (the region of space around a star within which orbiting material is gravitationally bound to that star) and evolve separately like single stars; 2) *semi-detached systems*, where one of the stars fills its Roche lobe and mass exchange between the components occurs; and 3) *contact systems*, where both components fill their Roche lobes and form a common shell around the stars. In the last two groups of binaries, the evolution of the stellar components is different from that expected for single stars. Due to the mass transfer, stellar evolution happens on a much shorter time scale. Also the tidal interaction between the components and the occurrence of rapid mass transfer episodes in semi-detached binaries, leading to the formation of accretion disks, influence the evolution of the components.

In this work we focus on eclipsing Algol-type systems with pulsating primary components. In the subsequent paragraphs we introduce the role of this type of stars as a laboratory for studying stellar evolution on a short time scale and the role of asteroseismology as an important, modern tool for the investigation of such systems. And we give an overview about the different approaches in deriving the stellar and system parameters of binary stars from the observations and the computer programs that have been developed for this task. Finally, we compare the capabilities of photometric and spectroscopic investigations, stressing the importance of using both simultaneously for a complete analysis.

1.2   Algol-type stars

Algol-type systems are semi-detached, interacting, eclipsing binaries consisting of a main-sequence star of spectral type A–B and an evolved F–K type companion of luminosity class III. The reasons for the existence of two stars in such different evolutionary stages in one physical system have been a great mystery for astronomers for a long time. Moreover, the less massive star in the system is the more evolved one which completely contradicts our knowledge about stellar evolution. This so-called *Algol paradox* was solved by realizing that the presently evolved star was initially the more massive one (see e.g. Batten (1986)). During its evolution it filled its Roche-lobe and transferred then a part of its matter to the companion. The
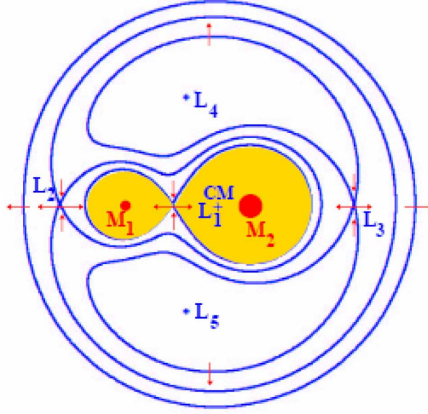
Figure 1.1: Equipotential surfaces and the five Lagrangian points L_1–L_5. The blue cross (CM) is the center of mass of the two stars, it is $M_2 > M_1$.

fraction of transferred matter can reach 30-40% of the total mass. There is some ambiguity in the designation of the system components. Usually, the actually more massive component is called the primary component, as we will do throughout this work. However, in some articles the components are still defined vice versa, reflecting the point of view of stellar evolution.

Algol-type systems are eclipsing binaries and so their stellar and system parameters can be obtained with high accuracy from the light curve analysis combined with spectroscopic investigations. But they are also excellent laboratories for studying accretion processes. Figure 1.1 shows the equipotential surfaces of a binary system together with the points of gravitational equilibrium which are called the Lagrangian points. As it was mentioned, the Roche-lobe is defined as the space around a star within which the orbiting material is gravitationally bound to that star. The equipotential surfaces passing through the inner Lagrangian point L_1 define the outer boundaries of the Roche-lobes of the stars. The underlying Roche model assumes synchronous rotation, circular orbits, and the gravitational potential of the stars to be that of point masses. The formation of accretion structures in Algol-type systems strongly depends on the orbital period. In short-period Algols (orbital period $P < 6^d$), the resulting structures are complicated. The gas stream from the secondary component flows via the inner Lagrangian point L_1 (the point of gravitational equilibrium that is located on the connecting line between the components) and impacts on the photosphere of the primary component. Besides the gas stream, an unstable accretion annulus is formed around the gainer and a part of the material leaves the system via Lagrangian point L_2 (Figure 1.1). In Algols with longer periods ($P > 6^d$), "classical" accretion disks are formed. The Coriolis force that acts on the gas stream allows it to supply the disk with accretion material and prevents any direct impact of the transferred mass on the primary (Albright & Richards 1996). In contrast to the short-period systems, the accretion disks are stable and the term "classical" is used to emphasize this difference.

The secondary components of Algol-type systems are known to be magnetically active. Evidence of such activity can be seen from the formation of starspots or flares on the surfaces

Table 1.1: Algol-type systems with oscillating primary components.

object	m_V	P_{orb} (days)	P_{puls} (min.)	reference
Y Cam	10.6	3.3055	95.74	Kim et al. (2002)
AB Cas	10.3	1.3669	83.93	Rodriguez et al. (2004a)
RZ Cas	6.3	1.1953	22.43	Lehmann & Mkrtichian (2004)
IV Cas	11.0	0.9985	38.22	Kim et al. (2005c)
R CMa	5.7	1.1359	68.5	Mkrtichian & Gamarova (2000)
V346 Cyg	11.8	2.7433	72.3	Kim et al. (2005a)
V469 Cyg	12.8	1.3125	40	Caton (2004)
AS Eri	8.3	2.6642	24.39	Mkrtichian et al. (2004)
TZ Eri	9.7	2.6061	76	Mkrtichian et al. (2006)
TZ Dra	9.3	0.8660	29	Mkrtichian et al. (2006)
TW Dra	7.4	2.8069	80	Kusakin et al. (2001)
CT Her	11.3	1.7863	27	Kim et al. (2004a)
EF Her	11.4	4.7291	145	Kim et al. (2004a)
TU Her	11.2	2.2671	80	Lampens et al. (2004)
RX Hya	9.6	2.2816	74.26	Kim et al. (2003)
AB Per	9.7	7.1603	282.0	Kim et al. (2003)
IU Per	10.5	0.8570	34.3	Kim et al. (2005b)
AO Ser	11.4	0.8793	70	Kim et al. (2004b)
QU Sge	15.2	3.7908	40.1	Jeon et al. (2006)
VV Uma	13.0	0.6874	28.1	Lazaro et al. (2002)

of these cool stars. The starspots can be detected from the timely variations in the shape and depth of the light curves that they produce. The magnetic activity is more difficult to investigate because the secondary component contributes with only about 10% to the total light of the system at optical wavelengths. Here, the eclipse phases play an important role when the variations in both the light curves and the spectral line profiles become more pronounced and can be analyzed much easier (Richards & Albright 1993).

1.3   Algol-type stars with oscillating components (oEA stars)

The new class of oEA stars was introduced by Mkrtichian et al. (2002, 2004) and refers to mass accreting, eclipsing Algol-type systems consisting of an oscillating, main-sequence primary and a Roche-lobe filling, evolved secondary. The pulsation characteristics of the primary components are similar to those of the δ-Scuti stars, showing oscillation periods in the range of hours. Their evolution is speeded up due to the occurrence of rapid mass transfer episodes, however. Table 1.1 lists the 20 oEA stars known up to now, mainly discovered in the result of collaborative efforts (Mkrtichian et al. 2002b; Kim et al. 2003). Figure 1.2 shows the discovery rate of oEA stars. As can be seen, only few objects were detected before the mentioned surveys have been organized. The first detection of δ Scuti-like oscillations in an eclipsing binary star has been reported by Tempesti (1971). The author found short-term
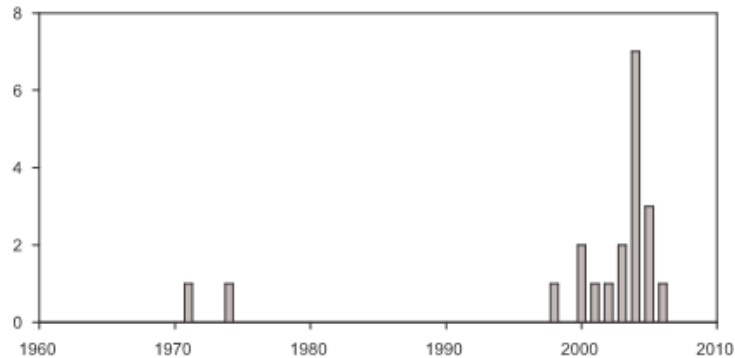
Figure 1.2: The number of discovered oEA stars versus the date of their discovery (figure taken from Mkrtichian et al. (2007)).

variability in the light curve of AB Cas with a period of 84 minutes and an amplitude of $0\overset{m}{.}05$. That time the star was classified as a detached system consisting of a primary of spectral type A3 and an early K-type main sequence secondary, however. Another early discovery of a variable star of δ Scuti type in an eclipsing binary system was reported by Broglia (1973). The author observed the short-term variability of the A7 V primary component of Y Cam with a period of $0\overset{d}{.}063$ and an amplitude of $0\overset{m}{.}04$.

Algol-type systems are known to show long-term variations of their orbital periods, which can be detected from the O–C (observed minus calculated) diagram. In the case of eclipsing binaries, this diagram shows the difference between the observed and the calculated times of minima, plotted versus the time that is usually given in Julian Dates. Any deviation from a straight line in this diagram indicates a change of the orbital period. A sinusoidal curve, e.g., can be caused by the light time effect and points to the existence of a third body in the system (Hoffman et al. 2006). Another mechanism that produces cyclic period changes of the oEA stars can be the magnetic activity of the late-type secondary that periodically changes its oblateness and quadrupole moment which is reflected by a corresponding change in the orbital period (Applegate 1992; Lanza & Rodono 1999).

Besides the orbital period variations, the oEA stars exhibit changes in their pulsation patterns as well as in the amplitudes of their oscillation modes. Lehmann & Mkrtichian (2004) investigated the well-known oEA star RZ Cas based on high-resolution spectra taken in 2001 during an episode of rapid mass transfer. The authors found two pulsation frequencies in the data which means that the primary component of the system changed its oscillation behavior from the previously, photometrically observed mono-periodic pulsation to multi-periodic pulsations. In 2006, when the star was back in a quiet phase, a new pulsation pattern was detected, now showing three modes of different amplitudes (Lehmann & Mkrtichian 2008a).

Mkrtichian et al. (2007) state that the pulsation characteristics of the oEA stars can be affected by the mass transfer episodes in two different ways: by a *direct influence*, when the accreted mass changes the physical properties of the gainer by changing its mean density and the structure of its outer layers, and by an *attenuation effect*, when the accretion annulus around the oscillating primary, formed in the result of mass transfer, alters the observed amplitudes of the oscillation modes. The second effect has been described by Lehmann &

Mkrtichian (2008a) for RZ Cas. They observed that the amplitudes of the oscillation modes were damped in 2001 due to the presence of optically thin circumprimary matter, whereas in 2006, when the star was in a quiet phase, the intrinsic amplitudes could be observed.

More details about our two target stars RZ Cas and TW Dra are given in Section 1.7. The role of the oEA stars in asteroseismic investigations is described in § 1.4.2.

1.4   Asteroseismic modeling

Asteroseismology is a powerful tool in modern astrophysics that allows to study the interiors of the stars by the interpretation of the frequencies, amplitudes and phases of their non-radial oscillation modes. These modes are excited inside the star in zones where, in dependence on the mass and temperature of the star, hydrogen, helium, or iron peak elements are partially ionized and propagate through the star as acoustic (p-modes) or gravity (g-modes) waves of different frequencies. The modes are described in terms of n, l, and m wavenumbers that describe the number of nodes in radial and horizontal directions. n is called the *radial degree*. The *degree l* gives the number of surface nodal lines, while the *azimuthal wavenumber m* gives the number of surface nodal lines that pass through the rotation axis of the star.

1.4.1   Asteroseismic methods

One goal of asteroseismology is to measure the sound speed throughout the star. Since the local sound speed depends on the temperature and molecular weight of the gas (it is higher for gases of higher temperature and lower weight), and since different modes penetrate into different optical depths, it is possible to get information about the temperature distribution inside the star. Based on the obtained temperature distribution, one can evaluate for a given chemical composition the density and pressure from the equations of state. Moreover, due to the coexistence of stellar rotation and pulsation, there is the possibility to estimate the internal rotation rates of the stars based on the *rotational splitting* (Ledoux 1951) of the oscillation modes. Rotation lifts the degeneracy with respect to the azimuthal wavenumber m, and for a certain degree l we observe a multiplet of $2l + 1$ frequencies corresponding to the possible number of different values of m. So, if oscillation modes of different degree l that penetrate the star into different depths are observed and identified, one can map the interior rotation rates. This analysis is hampered by the fact not all possible modes in such a multiplet are excited or have large amplitudes, however. A general problem is that actually a unique identification of pulsation modes is available only for a very small number of stars. Future advance will come both from new observational methods, in particular from the high-accuracy, timely continuous data from space satellites like the CoRoT and Kepler missions and from the further development in mode identification techniques. One of the most recent computer programs established for frequency search and mode identification in oscillating stars is the FAMIAS program package developed by W. Zima. The program considers both photometric and spectroscopic data sets. For the mode identification, the color-amplitude method in the case of light curves, or either the pixel-by-pixel or the moments method in the case of time series of spectra can be used. For a detailed description of the program and the mentioned methods see Zima (2008).

Besides a unique mode identification, the precise knowledge of stellar parameters like mass, radius, effective temperature, gravity, and metalicity is needed for a subsequent construction of an asteroseismic model of a star. Double-star systems, and in particular eclipsing binaries, provide an unique opportunity for measuring most of these parameters, as we will show in Section 1.6.

1.4.2   Application to the oEA stars

The oEA stars, introduced in Section 1.3, are outstanding targets for asteroseismic investigations. Due to the occurrence of mass transfer episodes, most probably triggered by the magnetic activity cycle of the cool secondary, stellar evolution can be studied on short time scales. During or immediately after such phases of rapid mass transfer we observe a change in the excited oscillation modes. Thus, the changing structure of the outer layers of the primary can be investigated by asteroseismic methods. The observations can also reveal basic principles of the interaction between the magnetic activity cycle of the cool secondary, the occurrence of rapid mass transfer episodes, and the excitation of different non-radial pulsation modes of the primary. Due to the strong tidal interaction, the rotation axes of the stars will not be inclined to the normal of the orbital plane. Thus, since the orbital inclination is close to $90°$, we see the pulsating primary component nearly equator-on. Mkrtichian et al. (2004) showed that in this case all oscillation modes with $l + |m| = odd$ are almost smeared out in the disk integrated light which restricts the number of pulsation modes that can be observed. Moreover, the secondary acts as a spatial filter during the primary eclipse phases and produces specific amplitude and phase changes in brightness and line profiles, depending on the observed oscillation modes. By modeling the amplitude modulation at these phases and comparing it with the observed one, one can restrict the range in l and m wavenumbers even more. The method of spatial filtering has been applied photometrically to the oEA stars RZ Cas (Gamarova et al. 2003) and AB Cas (Rodriguez et al. 2004a) with the aim of the identification of low degree modes. It was found that the pulsation amplitude modulation of RZ Cas observed during the primary eclipse can be modeled by an $(l, m) = (2, \pm 2)$ oscillation mode, while the AB Cas system most probably pulsates in a radial mode. Reed et al. (2005) published an extended photometric work related to mode identification making use of the spatial filtration effect. The authors investigated oscillating subdwarf B star binaries and simulated the behavior of the pulsation amplitudes during the eclipse phases. They found in particular that oscillation modes with $l > 2$ become visible during the eclipse of the pulsating component but disappear outside the eclipse. There was only one spectroscopic detection of the spatial filtration effect so far, however. Based on the analysis of the radial velocities (RVs hereafter) of the oEA star RZ Cas, Lehmann & Mkrtichian (2008a) found a strong amplification of the detected oscillation modes during primary eclipse, exactly as suspected from the screening effect. In the present work, we will try to model the spatial filtration effect spectroscopically (Chapter 6) by using the modified Shellspec07_inverse program (§ 2.2). Based on these simulations, we look for systematic relationships between different stellar system and pulsation parameters and the amplitudes of the oscillation modes (Chapter 6).

1.5   Photometric modeling

Here we describe the historical background of the different approaches to the light curve analysis and give a short description of the Wilson-Devinney program, nowadays commonly used for the modeling of the light curves of binaries.

1.5.1   Historical background

The history of light curve modeling most probably starts with the Russell-Merrill model (Russell 1912; Russell & Merrill 1952). This model was restricted to spherical stars revolving around their common center of mass in a circular orbit. A linear limb-darkening law, gravity brightening and a simple treatment of the reflection effect were taken into account. The obtained solutions appeared to be accurate enough for well-separated eclipsing binaries but not for semi-detached or contact systems. A significant step forward in the modeling of the light curves of eclipsing binaries was done by Kopal (1959) who used a more physical approach with respect to the configuration of the stars, based on a quantitative discussion of their equipotential surfaces. The first attempt of a direct computation of synthetic light curves for the W Ursae Majoris-type stars was done by Lucy (1968). These stars are overcontact main-sequence binaries with convective outer layers. Their light curves are strongly affected by the deviations of the stellar shapes from sphericity and the Russell-Merrill model completely fails. Lucy's approach is limited to overcontact systems and assumes the surfaces of such systems to be equipotential surfaces computed from the Roche model. For the calculation of the limb darkening effect the Eddington-Barbier relation is used. The model considers the effect of gravity brightening, while the reflection effect is neglected. Later on, different methods have been developed for the analysis of binaries' light curves based on equipotential surfaces and Roche geometry and successfully applied to various types of double-star systems (Hill & Hutchings 1970; Mochnacki & Doughty 1972; Hill & Rucinski 1993; Wilson & Devinney 1971).

The progress in the light curve modeling was very important for different fields in astronomy because it allowed to solve many problems which could not be explained before, among them for instance the Algol paradox or the structure of the W UMa-type systems. The solution of the Algol paradox was already described in § 1.2. The W UMa stars problem came from the fact that both the solutions based on spherical stars and on stars of ellipsoidal shapes gave detached configurations. On the other hand, the results showed that both stars have almost equal surface temperatures but different masses, which cannot be explained in the case of detached main-sequence stars. Then Kuiper (1948) suggested that W UMa stars are overcontact binaries forming a common envelope that allows for an energy exchange between the stars. In this case the total energy output would correspond to the mass of the primary and the paradox observed before would be solved. This suggestion was later on confirmed by Lucy (1968) who successfully modeled the light curves of the W Ursae Majoris stars based on the Roche model of overcontact binaries.

1.5.2   The Wilson-Devinney model

One of the first attempts of deriving stellar and system parameters from binaries' light curves based on the solution of a least-squares problem was done by Wilson & Devinney (1971). Presently, the Wilson-Devinney code (WD, hereafter) is one of the most commonly used programs for the analysis of binary systems based on their observed light and RV curves. Here we give a brief description of the Wilson-Devinney model that underlies the corresponding WD program and has been used by many different authors as the basis for their own programs, including many useful extensions. The model supports circular as well as eccentric orbits and the distance between the binary's components can be set as a phase-dependent value. Non-synchronous rotation of the components meaning that the ratio of the rotational angular velocity to the mean orbital velocity differs from unity, is considered as well. The surfaces of the components are computed based on the Roche model assuming a complete central condensation for both stars. The flux irradiated by each point on the stellar surface is computed by scaling the polar intensity by different factors, counting e.g. for the gravity and limb darkening or the reflection effect. Von Zeipel's law (von Zeipel 1924) is used for computing the gravity darkening while the limb darkening is taken into account using one of the analytical (linear, quadratic, logarithmic etc.) laws. The program considers single and multiple reflections (Wilson 1990).

The WD program is divided into the two main parts LC and DC. LC is designed for the calculation of either light and velocity curves or spectral line profiles. The DC program is used for an optimization of the stellar and system parameters of the binaries based on the light and RV curves separately or on both simultaneously. There is no possibility to use spectral line profiles for the parameter optimization, however. The WD program uses the Simplex algorithm for the initial parameter search. Either the method of differential corrections or a damped Levenberg-Marquardt algorithm (Levenberg (1944), Marquardt (1963), see Kallrath et al. (1998) for more details and some test results) can be used for the optimization of the parameters.

According to different binary system configurations, the WD program can be used in different modes like for detached, semi-detached, double-contact and overcontact systems, or X-ray binaries. We refer to the paper by Wilson (1993) for more details.

1.6   Spectroscopic modeling

In the previous section we described the WD program that can use both light curves and RVs as an input for the modeling of binary systems. RVs, on the other hand, are not well-defined quantities in the case of stars that show line profile variations because different methods of its determination like the computation of the first order moments of line profiles, the fit of special functions to the line profiles like Gaussians, or the shifts obtained from cross-correlation techniques will give different results. In this case, it will be much better to use the line profiles itself instead of integral quantities, or, in other words, the full information content of the obtained spectra. The probably first attempt in this direction was done by Mukherjee et al. (1996) who introduced the computation of spectral line profiles into the WD code with the aim to measure the rotational velocities of the binaries' components. It was done by

fitting the computed line profiles to the observed ones by means of the method of differential corrections and using the Simplex algorithm. The authors measured in this way the rotational and micro-turbulent velocities of 13 Algol-type systems (Mukherjee et al. (1996)).

One important difference between photometry and spectroscopy is the difference in the spectral resolution defined as $R=\lambda/\Delta\lambda$, where $\Delta\lambda$ represents the bandpass of the instrument or the smallest resolution element in wavelength. The typical resolution of narrow-band photometry is of about 500. For broad- and intermediate-band photometry the resolution is even lower. On the other hand, stellar spectroscopy provides a spectral resolution up to 100 000. Many physical quantities and effects in stellar physics can be determined only from high-resolution spectroscopy, like the chemical abundances in stellar atmospheres, the magnetic fields observed from the Zeeman splitting of spectral lines, or the detection and confirmation of extra-solar planets from the Doppler shifts observed for planet hosting stars in the order of meters or even centimeters per second.

Both the analysis of light- and of radial velocity curves allows to determine the orbital period, eccentricity and orientation of the orbit. The shape of the light curve's minima indicates whether the corresponding eclipse is a partial or a total one. This shape also provides information about th radii of the stars relative to the size of the orbit, about the orbital inclination, and, together with the depths of the minima, about the luminosity ratio between the stars.

Concerning eclipsing binary stars, high-resolution spectroscopy also provides us with important information. So, the Rossiter-McLaughlin effect (Rossiter 1924; McLaughlin 1924) can be observed. This is a pure spectroscopic effect that occurs during the eclipse phases due to the stellar rotation. During both eclipses, the component which passes in front of the disk of the eclipsed star blocks the light coming from the receding or approaching part of the eclipsed disk, producing variations in the observed line profiles. Consequently, the RVs measured from these highly asymmetric line profiles show an anomalous behavior. The strength of the Rossiter effect depends on the rotation velocity of the eclipsed star and on the brightness ratio between the components. If one component is much brighter than the other one, as it is the case in all Algol-type stars, then the Rossiter effect will be much more pronounced during the primary eclipse than during the eclipse of the fainter secondary.

Figure 1.3 shows in its upper panel the RVs of the primary component of the oEA star RZ Cas observed in 2006. The Rossiter effect is well pronounced and can be seen as the S-shaped distortion at phase 1.0 where the primary minimum occurs. The lower panel shows the RV residuals after subtracting the orbital RV curve. Figure 1.4 shows the Rossiter effect in the spectral line profiles, computed at orbital phases of $\phi = 0.95$ and $\phi = 1.05$. At these phases the faint component passes in front of the primary, blocking the light first from the approaching and then from the receding parts of the surface of the primary. This results in highly distorted line profiles with shifted centers of gravity.

The shape of the Rossiter effect is sensitive to various system parameters. It can be used, e.g., to determine the orbital inclination of the binary independently of photometry. Another parameter that strongly influences the shape of the Rossiter effect and that can be determined only from spectroscopy is the inclination angle of the rotation axis of the eclipsed star in the observers plane on the sky (the plane perpendicular to that where $v \sin i$ is measured). A change of this angle by a few degrees results in obvious changes of the shape of the Rossiter
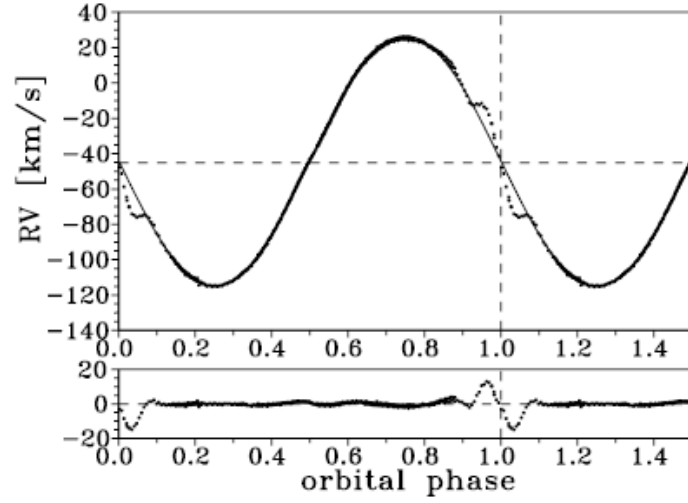
Figure 1.3: RVs of the primary of RZ Cas observed in 2006 (upper panel) and the residuals after subtracting the orbital motion (lower panel). The vertical dashed line indicates the primary minimum while the horizontal line gives the systemic γ-velocity (figure taken from Lehmann & Mkrtichian (2008a)).
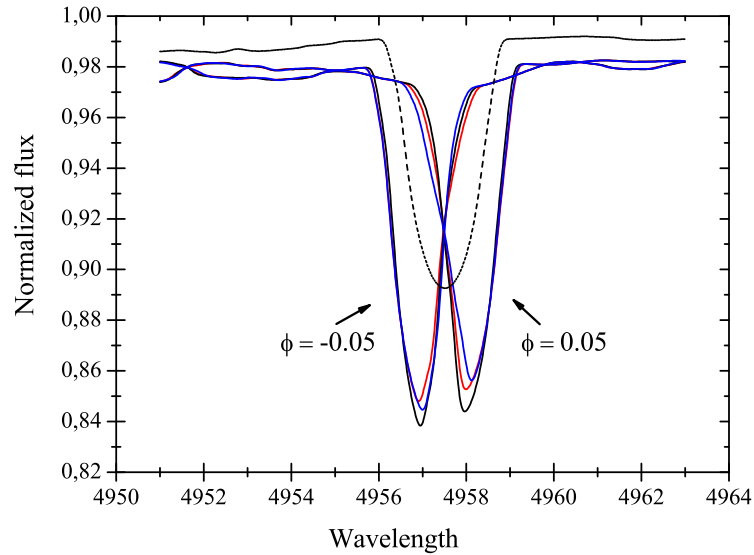
Figure 1.4: Synthetic line profiles computed with Shellspec07_inverse (see Section 2.2) for the eclipse phases $\phi=-0.05$ and $\phi=+0.05$ and for different inclinations of the rotation axis. **Red:** The axis is aligned with the normal to the orbital plane. **Blue:** The axis is inclined to the normal by an angle of $15°$ in the observers plane. **Black:** The axis is inclined to the normal by an angle of $15°$ towards the line of sight. The line profile at out-of eclipse phases is shown by dashes.

effect, as can be seen from Figure 1.4.

The most important parameter of a star is its mass that determines most of its properties and its evolution. It is not possible to determine absolute masses directly from photometry. There is a possibility of an indirect determination of the mass ratio of semi-detached and overcontact binary systems from photometry, however. This method uses the fact that one or both stars fill their Roche lobes. In this case one can estimate the mass ratio from the radii of the stars. The radii give the size of the Roche lobes and, if the Roche model is valid, the mass ratio follows from the size of the Roche lobes (Wilson 1994). From the spectroscopy of single lined binaries in an orbit of eccentricity e one only gets the so-called mass function

$$f(M_{1,2}) = \frac{(M_{1,2}\sin i)^3}{(M_1 + M_2)^2} = 1.036 \cdot 10^{-7} K_{2,1}^3 P(1 - e^2)^{3/2}, \qquad (1.1)$$

where the masses are in solar units, the RV semi-amplitudes K are in $\mathrm{km\,s^{-1}}$, and the orbital period P is in days. In the case of double-lined binaries, the mass ratio follows directly from the ratio of the RV amplitudes, it is $M_2/M_1 = K_1/K_2$. For the absolute masses one obtains a lower limit, it is

$$M_i \sin^3 i = \left(1 + \frac{K_2}{K_1}\right)^2 f(M_i) \qquad (1.2)$$

Only in the case that the orbital inclination i is known one obtains absolute masses. This is the case for double-lined eclipsing binaries, where i can be determined either from photometry or from a spectroscopic analysis of the Rossiter effect as shown before. That one of the reasons why stars of this special type play an outstanding role in astrophysical research.

The best way to get as much information as possible and to be able to compare the results obtained from two independent methods is to combine spectroscopic and photometric observations. For that reasons and with the aim to establish a computer program based on spectroscopic line profiles that is comparable to the WD code in photometry we developed the program Shellspec07_inverse that served as the central engine in deriving the results on oscillating Algol-type stars presented in this work.

1.7   The target stars

In this section we introduce the targets of our investigation, the oscillating Algol-type stars RZ Cassiopeia and TW Draconis and summarize the results obtained by different authors so far.

1.7.1   RZ Cassiopeia

RZ Cassiopeia (HD17138, HIP 13133) belongs to the class of oEA stars. It is a short-period ($P=1^d.1953$) Algol-type system and one of the best studied oEA stars. The primary component is classified as A3 V while the secondary component is of spectral type K0 IV. During primary minimum, a partial eclipse is observed (Narusawa et al. 1994). Olson (1982) and Varricatt et al. (1998) found evidence of circumstellar matter surrounding the primary. Single-peaked emission originating from a structure located between the two stars was detected by Richards & Albright (1999). The spectra and applied Doppler tomography (Richards 2004)
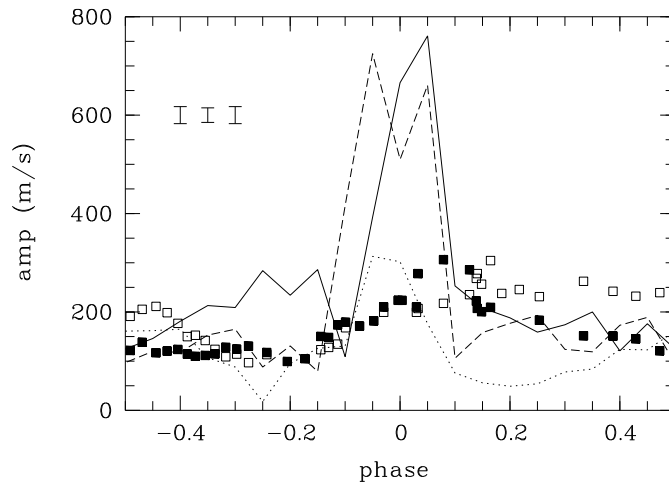
Figure 1.5: Amplitudes of RV variations folded with the orbital period. Curves: observations from 2006. Solid: f_1. Dotted: f_2. Dashed: f_3. Error bars: from left to right for f_1 to f_3. Squares: observations from 2001. Filled squares: f_1. Open squares: f_2 (figure taken from Lehmann & Mkrtichian (2008a)).

indicate that a gas stream was visible during the observations in 1994. The presence of a gas stream is also assumed by Rodriguez et al. (2004b). Based on extended photometric observations in 1999, the authors proposed a hot spot located at the position where this stream impacts the surface of the primary. The discovery that RZ Cas is both an X-ray source (Mc-Cluskey & Kondo 1984) and a variable radio source (Drake et al. 1986) was explained by Umana et al. (1999) by the strong coronal activity of the cool secondary.

RZ Cas was found by Ohshima et al. (1998, 2001) to exhibit short-period light variability. They detected a dominant oscillation mode of the primary with a frequency of 64.2 $c\,d^{-1}$. This was later confirmed by both Mkrtichian et al. (2003) and Rodriguez et al. (2004b), based on the results of dedicated photometric campaigns. An apparently mono-periodic behavior with a dominant frequency of 64.2 $c\,d^{-1}$ was observed from the photometric observations acquired until 2000. Lehmann & Mkrtichian (2004) found multi-periodic oscillations from the spectra taken in 2001, with two dominant frequencies of f_1=64.189 and f_2=56.600 $c\,d^{-1}$. Both are in agreement with the photometric results by Mkrtichian et al. (2003), who also found that the photometric amplitude of the principal mode was lower than in 1997-2000. A detailed investigation of the photometric variability showed an increase in the amplitude of f_1 between the years 2001 and 2006. (Mkrtichian et al. 2007).

In 2006, the star changed its pulsation pattern again. Lehmann & Mkrtichian (2008a) found at least three pulsation frequencies of f_1, f_2, and f_3=62.406 $c\,d^{-1}$, where the third one was observed for the first time. By comparing the spectra taken in 2001 and 2006, the authors observed a changing asymmetry in the Rossiter-McLaughlin effect, a much stronger amplitude modulation of the non-radial pulsation modes due to the spatial filtration effect in 2006 compared to 2001 (Figure 1.5), and an increase of the orbital period. The authors concluded that RZ Cas has undergone a transient phase of rapid mass transfer in 2001, whereas it was in a quiet state in 2006.

Stellar and system parameters of RZ Cas were derived by Maxted et al. (1994) from com-

bined spectroscopy and UBV photometry taken from Chambliss et al. (1976), by Varricatt
et al. (1998) from UBV (Chambliss et al. 1976) and J and K band photometry, by Rodriguez
et al. (2004b) from Stroemgren photometry, by Soydugan et al. (2006) from combined spec-
troscopy and B and V band photometry, and by (Lehmann & Mkrtichian 2004, 2008a) from
spectroscopy. An effective temperature of the primary of $8\,600\,\mathrm{K}$ was derived by Rodriguez
et al. (2004b) from the color indices, in agreement with Maxted et al. (1994), whereas Var-
ricatt et al. (1998) adopted a higher temperature of $8\,720\,\mathrm{K}$. Maxted et al. (1994) derived a
mass ratio of q=0.331. Soydugan et al. (2006) analyzed both the light and radial velocity
curves based on photometric observations in 2002 and spectral data from 2003/2004 by using
the Wilson-Devinney program (Wilson & Devinney 1971; van Hamme & Wilson 2003). For
a fixed surface temperature of the primary of $8\,600\,\mathrm{K}$, the authors derived the temperature
of the secondary to $4\,480\,\mathrm{K}$, the mass ratio to 0.338, the orbital separation to $6.87\,\mathrm{R}_\odot$, and
the orbital inclination to $81°.98$. Varricatt et al. (1998) mentioned that the best-fit model of
the J band light curve is obtained by assuming a dark spot on the surface of the secondary.

In this work we apply the Shellspec07_inverse program (see Section 2.2) to the RZ Cas sys-
tem to derive precise stellar and system parameters. We use the KOREL program (Hadrava
1995, 2004a) to compute the decomposed spectra of the components and an orbital solu-
tion that includes both stars (§ 2.3.1). Ihe individual spectra of the components are then
analyzed with the SynthV code (Tsymbal 1996) based on computed atmosphere models
(§ 2.3.2). The derived stellar and system parameters are then used as starting values in
the Shellspec07_inverse program which does a fine-tuning based on the observed composite
spectra of the binary system. Results of the analysis will be discussed in Chapter 4.

1.7.2   TW Draconis

TW Dra (HD 139319, HIP 76196) is a bright Algol-type system of spectral type A5 V+K0 III
with an orbital period of $2^d.807$. It is in turn the bright component of the visual binary
ADS 9706. The primary eclipse is a total one (Popper 1989). A first photoelectric study
of the light variation was made by Baglow (1952). Kopal & Shapley (1956) estimated the
masses of the components to M_1=1.9 $M_\odot$ and M_2=0.82 $M_\odot$, corresponding to a mass ratio
of q=0.43. Giuricin et al. (1980) analyzed the photoelectric data obtained by Baglow (1952)
and by Walter (1978) and favored the results based on the later data set. They found q=0.47
in good agreement with the value given by Popper (1989) based on the radial velocities.
Al-Naimiy & Al-Sikab (1984) analyzed the star's light curve and determined the radius of
the primary and the separation of the components to 2.5 $R_\odot$ and 12 $R_\odot$, respectively. Their
findings were in good agreement with those by Kopal & Shapley (1956) and Giuricin et al.
(1980). The most comprehensive study so far was that by Zejda et al. (2010). The authors
derived the stelar and system parameters based on the RVs using the FOTEL program
by Hadrava (2004b) and on the light curve analysis using the PHOEBE program (Prša &
Zwitter 2005). The results of this study are presented in Chapter 5 (Table 5.3) and used for
a comparison with our findings.

Kusakin et al. (2001) discovered the short-term light variability with a semi-amplitude of
2 mmag in the primary component of TW Dra, detecting one frequency peak at $17.99\,\mathrm{c\,d}^{-1}$ in
the periodogram. Kim et al. (2003) again investigated the system photometrically and found

a variability of 5 mmag semi-amplitude at orbital phases close to the secondary minimum. The derived oscillation frequency of 18.95 $\mathrm{c\,d^{-1}}$ is assumed to be the 1 $\mathrm{c\,d^{-1}}$ alias of the value given by Kusakin et al. (2001). The authors also found a second frequency close to 27 $\mathrm{c\,d^{-1}}$, suggesting that TW Dra is a multi-periodic pulsator. The first, dominating pulsation mode was also found by Zejda et al. (2006) in the vicinity of the primary minimum. Lehmann et al. (2008b, 2009) detected three oscillation modes of 22.90, 14.06, and 24.72 $\mathrm{c\,d^{-1}}$ from the line profile variations having semi-amplitudes of 0.3 $\mathrm{km\,s^{-1}}$. They could not find the 17.99 $\mathrm{c\,d^{-1}}$ mode detected by Kusakin et al. (2001), however. The authors tried to identify the modes and could limit the range in l and m to 7 to 12. They suggested that these high-degree modes are most likely sectoral modes but no unique identification could be derived.

TW Dra has long been known to show orbital period variations. A historical summary is given in Zejda et al. (2008). Qian & Boonrucksar (2002) found a secular increase of the orbital period by 4.43×10^{-6} $\mathrm{d\,y^{-1}}$ that they attributed to the dynamical mass transfer from the secondary to the primary with a rate of 6.8×10^{-7} $\mathrm{M_\odot y^{-1}}$. Besides on this secular change, the authors report on two irregular period jumps (increases with successive decreases) which they explain by structure variations of the secondary, possibly related to the magnetic activity cycle of this cool giant star. Zejda et al. (2008) inspected the system for orbital period changes again. They found that TW Dra showed an almost constant orbital period during the first observations in 1858–1905 whereas in 1905–1942 the period increased, corresponding to a mass exchange rate of 3.9×10^{-7} $\mathrm{M_\odot yr^{-1}}$. After that period of mass transfer, the star showed alternating cycles of increasing and decreasing orbital period that could be related to the magnetic activity cycle of the evolved secondary. These period changes are overlaid by other cyclic variations of much smaller amplitude caused by the light time effect of a third body with a period of 6.5 years.

In this work, we investigate the TW Dra system using several methods. We use the KOREL program (Hadrava 1995, 2004a) (see § 2.3.1) to compute the orbital solution and the decomposed spectra of the components of the Algol-type system. The derived orbital period and time of primary minimum are used to build the orbital phase binned spectra needed by Shellspec07_inverse (see Section 2.2) for further analysis. The extracted spectra are analyzed with the SynthV program (Tsymbal 1996) (see § 2.3.2) based on atmosphere models calculated with the LLmodels code (Shulyak et al. 2004) (see § 2.3.3). Finally, we apply the Shellspec07_inverse program for the fine-tuning of the stellar and system parameters of TW Dra based on the observed composite spectra. The results are presented in Chapter 5.

Chapter 2

Methods

Besides the already mentioned inclusion of synthetic line profiles into the WD program by Mukherjee et al. (1996), there have also been attempts to use the full information provided by the observed line profiles in computer programs designed for pure spectroscopic investigations. Vincent et al. (1993) and Piskunov (1996) extended existing Doppler imaging programs for the analysis of single stars to eclipsing binaries and were able to reproduce the stellar surface structures its components. Also Shellspec07 (Budaj & Richards 2004; Budaj et al. 2005) is one of the few modern computer programs that uses extended spectroscopic information beyond the RVs for the modeling of eclipsing binary stars. We developed our new program Shellspec07_inverse on the basis of this program and describe it in this chapter in more detail.

For the spectroscopic analysis of our target stars RZ Cas and TW Dra, we additionally use the KOREL (Hadrava 1995, 2004a), SynthV (Tsymbal 1996) and LLmodels (Shulyak et al. 2004) computer programs. The KOREL program allows to decompose the spectra of the individual components of multiple systems, simultaneously determining the corresponding RVs and the orbital elements. The obtained, decomposed spectra are then analyzed to determine the stellar parameters and elemental abundances based on stellar atmosphere models. Synthetic spectra are computed with the SynthV code based on the stellar atmosphere models, which are calculated with the LLmodels program. In the final step, the derived stellar parameters and orbital elements are provided as an initial guess to the Shellspec07_inverse program, which does the fine-tuning based on the observed composite spectra of the binary system.

2.1 The Shellspec07 program

The Fortran 77 code Shellspec07 was designed by Budaj & Richards (2004) for the computation of composite synthetic line profiles of interacting binaries. Structures originating from mass transfer like an accretion disk around the gainer or a gas stream between the stars can be taken into account. The synthetic spectra are computed based on a priori known input parameters, i.e. the program does not solve the inverse problem of deriving the stellar and system parameters from the observations. First, the model of the binary is calculated in the so-called "body frozen" system, centered at the primary component . The Cartesian, body frozen coordinates are x'', y'', z'', where the x''-axis points from the primary to the secondary component, the z''-axis is aligned with the normal to the orbital plane, and the y''-axis lies,
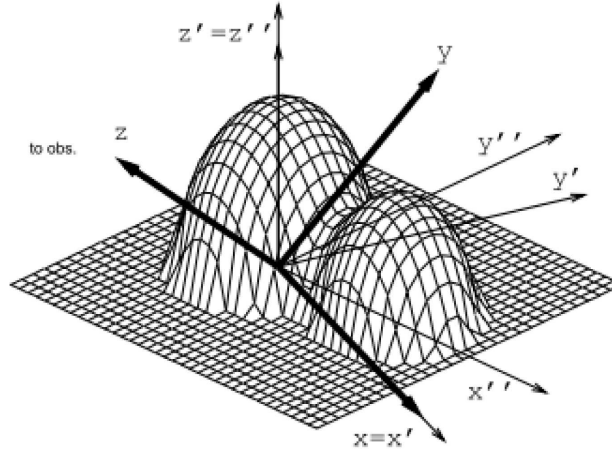
Figure 2.1: Orientation of the axes in the body frozen (x'',y'',z'') and the line-of-sight (x,y,z) Cartesian coordinate systems. The (x',y',z') coordinates correspond to an intermediate system used during the coordinate transformation (figure taken from Budaj & Richards (2004)).

like the x''-axis, in the orbital plane (Figure 2.1).

The program supports the following configurations of binary stars: detached systems, where both stars are considered as spherical objects; semi-detached systems, where one of the components fills its Roche lobe; and contact binaries where both components fill their Roche lobes forming a common shell. Let us consider the semi-detached systems in more detail. In this case, the surface of the evolved secondary is defined by the equipotential surface that passes through the so-called inner substellar point. This is the point located on the surface of the evolved star on the connecting line between the two components. Its location is related to the input parameter F_i, called the fill-in factor, via

$$F_i = R/L_1. \tag{2.1}$$

R is the stellar radius at the inner substellar point. It is measured in units of the distance from the center of the star to the inner Lagrangian point L_1 (see also Figure 1.1). In the case of Algol-type systems, the fill-in factor of the secondary component is usually assumed to be equal to unity while the deviation of the shape of the primary from sphericity is neglected. The equipotential surfaces are computed from the dimensionless Roche potential defined by

$$\Phi(x'', y'', z'') = \frac{2}{1+q} \left(\frac{1}{\sqrt{x''^2 + y''^2 + z''^2}} + \frac{q}{\sqrt{(x''-1)^2 + y''^2 + z''^2}} \right) + \left(x'' - \frac{q}{1+q} \right)^2 + y''^2, \tag{2.2}$$

where q is the mass ratio between the secondary and the primary components. After determining the boundaries in x$''$, the program defines the surface of the star in y$''$ and z$''$ using the Newton-Raphson method (Press et al. 1992). The method works very fast, and normally only few iterations are needed to achieve convergence. After the outer boundaries of the stars are determined, the program computes temperature, density, velocity fields etc. in each point of the body frozen frame. The stars themselves are considered to be non-transparent objects. This is marked by assigning special density values (that have no physical meaning)

to all points inside the stars to distinguish them from all transparent objects. The calculated surface velocity field includes stellar rotation and orbital motion. Synchronized rotation is assumed in the case that the star has a non-spherical configuration. The surface temperature distribution is given by von Zeipel's law (von Zeipel 1924). It is usually called the *gravity darkening* law and gives the variation of the effective temperature with the local gravity according to

$$\frac{T}{T_p} = \left(\frac{g}{g_p}\right)^{\beta}. \tag{2.3}$$

T_p and g_p are the temperature and the gravity at the pole, and β is the gravity darkening exponent. The theory predicts values of β=0.08 for stars with convective envelopes (Lucy 1967), and β=0.25 for stars in hydrostatic and radiative equilibrium (von Zeipel 1924).

In the next step, the program rotates the body frozen system according to the considered orbital phase and orbital inclination. First, the line-of-sight (or observer's) Cartesian coordinate system (x, y, z) is defined. The z-axis points along the line-of-sight toward the observer, the y-axis coincides with the normal to the orbital plane, while the x-axis lies in the orbital plane (Figure 2.1). The transformation between the body frozen and the line-of-sight coordinates is done in two steps. First, by a rotation around the x-axis by the orbital inclination i, and then by a rotation around the z'-axis by an angle α corresponding to the considered orbital phase:

$$
\begin{aligned}
x' &= x & z'' &= z' \\
y' &= y \cos i - z \sin i & y'' &= y' \cos \alpha - x' \sin \alpha \\
z' &= z \cos i + y \sin i & x'' &= x' \cos \alpha + y' \sin \alpha.
\end{aligned}
\tag{2.4}
$$

For the back transformation, the sign of the corresponding angle has to be changed.

Physical values are computed in the body frozen system. For the final integration over the visible disks (and possibly present circumbinary structures) in the observers frame, all the grid points in the observers frame are transformed to the body frozen system, and the physical values are interpolated to the corresponding coordinates. The interpolated values are then back-transformed to the observers frame. In a next step, the last non-transparent point is searched in the x-y plane of the observer's frame along the line-of-sight. This is the point on one of the stellar surfaces (depending on the orbital phase) that is nearest to the observer. For instance, if one looks onto the system from an aspect angle corresponding to the orbital phase of the primary eclipse, the last non-transparent point along the line-of-sight will be a point on the surface of the secondary. If no accretion structures are included, only contributions from the surface points of the non-transparent objects are taken into account when integrating over the x-y plane.

All non-transparent objects may radiate either as black bodies or show pre-calculated intrinsic spectra. The center-to-limb variation of the intensity, also called the *limb darkening effect*, is taken into account using a linear law given by

$$I'(\theta, \varphi) = I(\theta, \varphi)(1 - u + u \cos \theta), \tag{2.5}$$

where u is the limb darkening coefficient, θ is the angle between the line-of-sight and the normal to the stellar surface, and $I(\theta, \varphi)$ is the intrinsic intensity distribution on the stellar

surface. The gravity darkening effect is taken into account by scaling the obtained intensity $I'(\theta, \varphi)$ by a factor that is defined as the ratio of the Planck functions valid for the temperature T at a certain surface point and the temperature T_p at the stellar pole:

$$F_G = B_\nu(T)/B_\nu(T_p). \tag{2.6}$$

If any accretion structures like an accretion disk or gas streams are included into the model, the program solves the radiative transfer along the line-of-sight assuming that the non-transparent objects are embedded in an optically thin environment. The equation of radiative transfer reads

$$\frac{dI_\nu}{ds} = -\alpha_\nu I_\nu + j_\nu, \tag{2.7}$$

where I_ν is the specific intensity at frequency ν, α_ν the opacity, j_ν the emissivity and ds the distance along the beam extension. Since the light radiated by the star may not only be absorbed but also scattered, there are two sources of opacity included: true absorption (line opacity, H I bound-free and H I free-free continuum opacities) and scattering (Thomson and Rayleigh scattering). For the emissivity, contributions from the thermal and from the scattering emissivity are considered (see Budaj & Richards (2004) and Mihalas (1978) for a more detailed description). Once the radiative transfer is solved and the intensity in each point in the x-y plane of the observer's frame is computed, the integration over this plane takes place. Finally, the obtained synthetic composite spectrum is normalized to the continuum which is defined as a straight line between the outermost points of the considered part of the spectrum.

In the next paragraph, we introduce the new computer program Shellspec07_inverse that we established for solving the inverse problem of finding stellar and system parameters of eclipsing binaries from the observed spectra. It uses the core of Shellspec07 as the central subroutine. Besides the non-linear optimization algorithm, significant improvements related to the calculation of the limb- and gravity darkening effects as well as to the normalization of the computed spectra have been implemented.

2.2   The Shellspec07_inverse program

Shellspec07_inverse is a Fortran 90 code that uses the core of the Shellspec07 program (Budaj & Richards 2004). The calculation of the Roche geometry of the stars in the body frozen system, the necessary coordinate transformations according to different orbital phases and the inclination of the binary's orbit, and the integration of the fluxes from the visible stellar surfaces are taken from the Shellspec07 program. In the following, we describe the new features of the Shellspec07_inverse program.

2.2.1   Input and output routines

Shellspec07_inverse is designed for solving the inverse problem of finding stellar and system parameters of binary stars from the observed data. According to this task, new input and output routines have been implemented in the program. The input data consist of time-series of high-resolution spectra together with a list of the corresponding file names and the
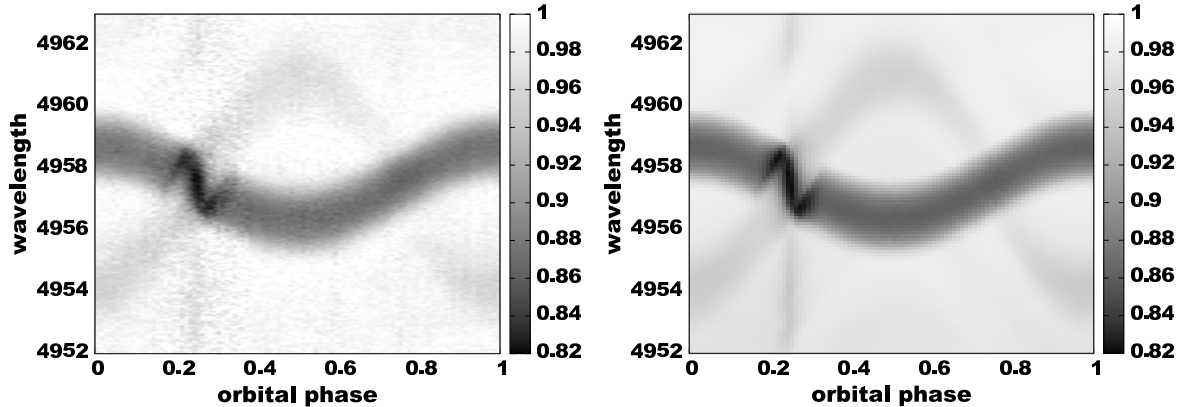
Figure 2.2: Two-dimensional representations of time-series of the observed (left) and calculated (right) Fe I 4957 Å line profiles of RZ Cas taken in 2006, folded with the orbital period. The spectra have been averaged into 100 orbital phase bins. Each mean spectrum (vertical direction) consists of the strong absorption line of the bright primary and the weak line of the faint secondary.

barycentric corrected Julian dates of observations. The spectra are provided in two-column ASCII format with the columns wavelength and normalized intensity. The orbital phase is calculated from the Julian date and the known ephemeris. The program can work in two different modes, optimizing the stellar and system parameters either based on the original spectra or on spectra that have been averaged into a certain number of orbital phase bins. The averaging is done by the program based on the bin size provided by the user. Synthetic spectra are computed for exactly the same orbital phases as given by the input spectra or computed for the averaged spectra.

The output consists of the values of the optimized stellar and system parameters as well as of graphical representations of the observed and computed spectra and the goodness of fit. Figure 2.2 (left panel) shows an example of the graphical output of the new program and illustrates how the input and output data have been organized. It shows in the left panel the composite Fe I 4957 Å line profiles of the RZ Cas system observed in 2006, averaged into 100 orbital phase bins and folded with the orbital period. The right panel shows the synthetic line profiles computed for both components of the oEA star RZ Cas based on the derived, optimized parameters for the RZ Cas system. For a better visualization, the orbital phase was shifted so that the primary minimum occurs at phase 0.25. The S-shaped distortion that can be seen at this phase is due to the Rossiter effect as described in § 1.6. The faint vertical stripe seen in Figure 2.2 at primary minimum originates from the strong enhancement by the Rossiter effect of the line depths of very faint lines that cannot be detected outside the primary minimum.

Figure 2.3 shows an example taken from the program's final output. It gives in the left panel the O-C residuals (observed minus computed line intensities) obtained for the RZ Cas system and in the right panel the corresponding χ^2-distribution. The latter one represents the O-C values normalized to the individual errors of measurement (see § 2.2.5 for a definition). Whereas the scatter in the O-C values strongly depends on the signal-to-noise of the input data that varies due to the different numbers of spectra that fall into one orbital phase bin or
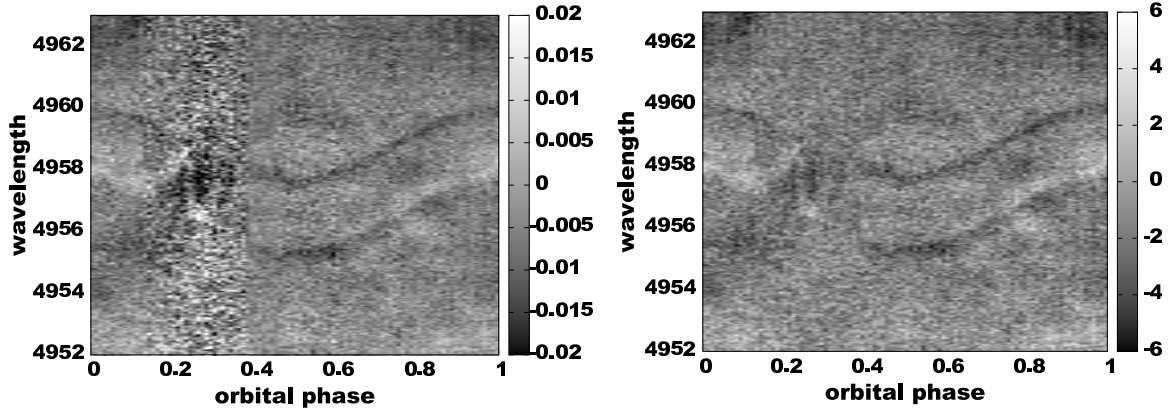
Figure 2.3: O-C residuals line intensity (left) and $the \chi^2$-distribution of the fit (right) computed for the finally derived parameters of the RZ Cas system.

due to the varying brightness of the objects (see the noisy region around primary minimum in), the χ^2-distribution is independent of such effects and is used as a measure of the goodness of fit.

2.2.2   The limb darkening effect

As described in Section 2.1, Shellspec07 assumes constant *intrinsic* stellar line profiles and calculates the center-to-limb variation by using a linear limb darkening law (see Eq. 2.5). This is a rough approximation because it assumes that the variation over the stellar disk can be described by a constant value of the limb darkening coefficient u that is independent of line depth. In reality, u varies strongly with line depth and can even reach negative values at the line center, as it was shown by Townsend (1997) for the Balmer line cores. Instead of using a fixed law, we used the SynthV program (Tsymbal 1996) (see § 2.3.2) to calculate the profiles for nine different values of the angle θ between the line-of-sight and the normal to the stellar surface and interpolate between them according to the desired position on the stellar disk. When we compute the limb darkening coefficient as defined by Eq. 2.5 from our procedure, we clearly see that it strongly varies with line depths. Figure 2.4 shows an example calculated from the Fe I 4957 Å doublet and the atmospheric parameters as derived for the primary component of the RZ Cas system (see Chapter 4). Figure 2.5 shows the difference between the two approaches for the H_β profile. It is obvious that the profile computed from the linear limb darkening law (solid curve) is significantly broader and stronger than that calculated from the wavelength-dependent law (dotted curve) used in the Shellspec07_inverse program. Since we want to model the spectra of our targets with high accuracy, the implementation of the new procedure is important. The second advantage is that we are not restricted to spherical disks but can also calculate the intensity variations produced by different optical depths along the line-of-sight in the case of a non-spherical star.
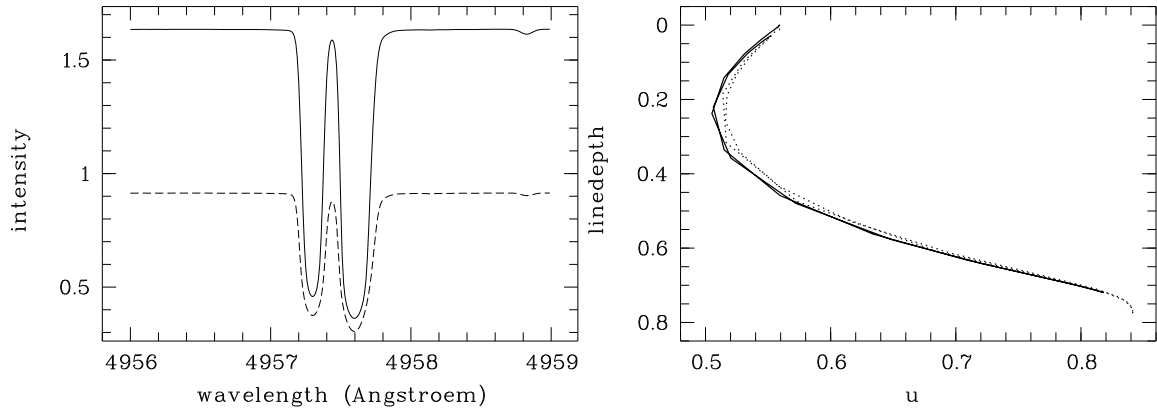
Figure 2.4: The limb darkening effect for the Fe I 4957 Å doublet. **Left:** Intrinsic line profiles calculated with the SynthV program at the center of the stellar disk (solid) and at the limb (dashed). The intensity is given in erg cm^{-2} s^{-1} Hz^{-1} rad^{-1}. **Right:** Limb darkening coefficient for different line depths, derived from the blue (solid curve) and from the red (dotted curve) components of the doublet shown to the left.
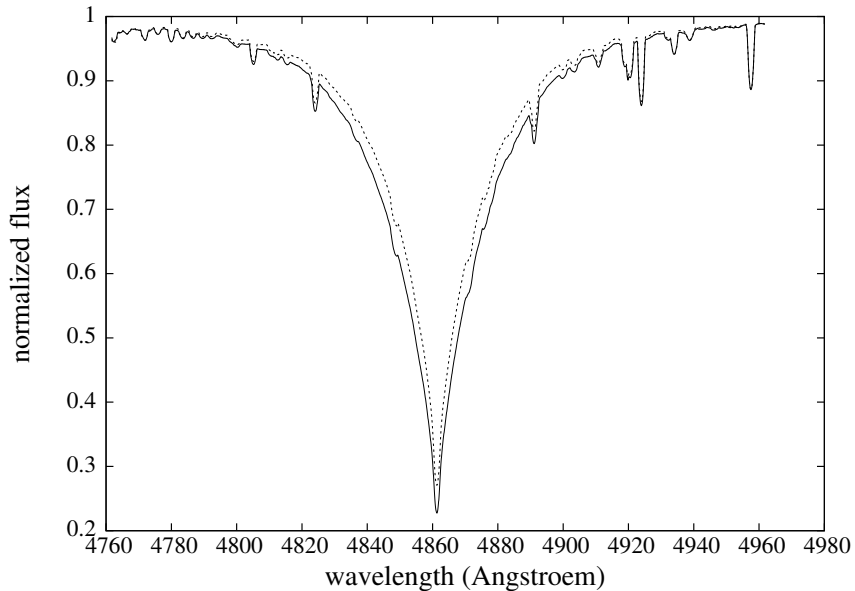

Figure 2.5: H$_\beta$ profiles computed with the linear limb darkening law (solid), and with the wavelength-dependent law (dotted) as used in the Shellspec07_inverse program.
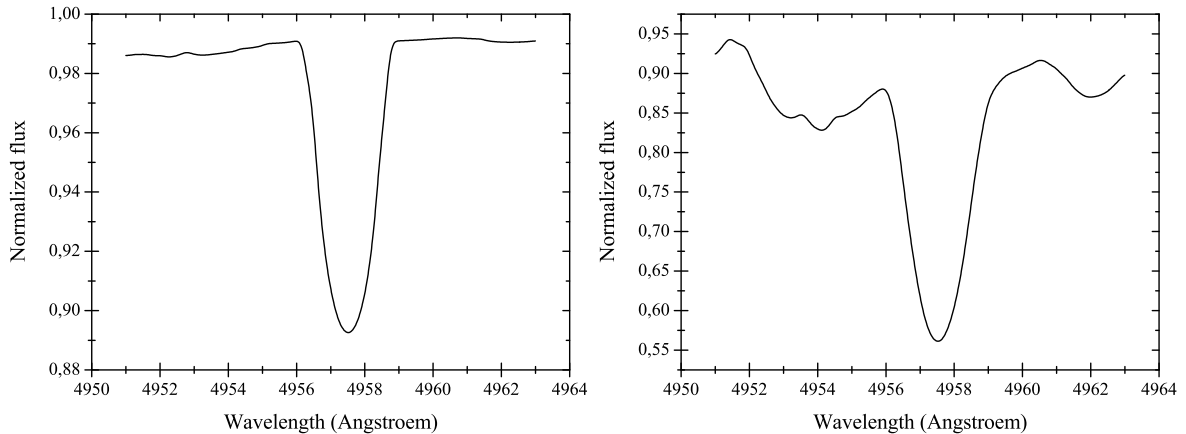
Figure 2.6: Normalized synthetic spectral line profiles computed with the Shellspec07_inverse program. The chosen line is Fe I 4957 Å line which appears in the red wing of H_β line profile. **Left:** T_{eff} = 8900 K, $\log g$ = 4.35. **Right:** T_{eff} = 4800 K, $\log g$ = 3.50.

2.2.3   The gravity darkening effect

Besides the limb darkening of both components, we have to take the gravity darkening of the Roche-lobe filling secondary into account. It results from the variation of the effective temperature with the local gravity on the surface of the non-spherical star according to Eq. 2.3. As described in Section 2.1, the Shellspec07 program takes this effect into account by applying a gravity darkening factor to the surface intensity that is valid for the pole of the star. The calculation of this factor from the ratio of the corresponding Planck functions is also a rough approximation, comparable to those that was made in the case of the limb darkening calculation. Again, we use the SynthV code to calculate the intrinsic line profiles for each point on the stellar surface for exactly the required temperature as given by Eq. 2.3, computing the local gravity from the Roche geometry of the stars.

2.2.4   Normalization of the computed and observed spectra

The Shellspec07 code uses a very simple procedure to normalize the computed spectra, assuming the continuum to be a straight line between the outermost points of the considered spectral range. This a rough approximation for two reasons. First, one cannot be sure that the outermost points will be part of the local continuum, the considered spectral range can also end up in the wings of a line. And second, the shape of the continuum may deviate significantly from a straight line, especially for the broad Balmer lines. Instead of this approximation, we calculate both the line and continuum fluxes with SynthV which makes the normalization of the synthetic spectrum a trivial task. Figure 2.6 illustrates the problem. It shows an example of normalized intensities in the Fe I 4957 Å line region computed with the Shellspec07_inverse program based on two different atmosphere models. In both cases, the profile does not reach unity in the continuum which is explained by the location of the line in the red wing of H_β. Moreover, in the case of the cool atmosphere (right panel), the additional contribution of molecules to the spectrum displaces the apparent continuum level even more from the true one and the approximation of the local continuum by a straight line

between the outermost points of the computed spectrum would never give a correct result.

Figure 2.6 also shows that the normalization of the *observed* spectra is not a trivial task at all. A wrong normalization of the observed spectra must be taken into account but its influence on the calculated model should be minimized. For that reason we introduce a scaling factor α for the observations which is defined by means of a least-squares fit in the sense of

$$(\alpha R_{obs} - R_c)^2 \rightarrow \min. \tag{2.8}$$

Here, R_{obs} is the observed spectrum, R_c is the spectrum computed with the Shellspec07_inverse program.

2.2.5   Non-linear optimization of stellar parameters

In the previous paragraphs we described necessary modifications and additions to the existing Shellspec07 program and the building of a user friendly environment. The task to solve the inverse problem, i.e., the optimization of stellar and system parameters based on the observed spectra, requires a larger effort and changes the program into a new one. For the non-linear optimization we use the Levenberg- Marquardt algorithm (Levenberg 1944; Marquardt 1963). It determines a set of parameters a of a function $y = y(x, a)$ by minimizing the χ^2 merit function

$$\chi^2(a) = \sum_{j=1}^{N} \left(\frac{y_j - y(x_j, a)}{\sigma_j} \right)^2, \tag{2.9}$$

where σ_j represents the error of the measurement of y_j. In our case, we sum up over all wavelength points of the considered spectral interval and over all observed spectra corresponding to different orbital phases. Thus, the χ^2 which is used in our program as a criterion for the goodness of fit, represents the sum over all single elements in Figure 2.3 (right panel). In each step of the iterative procedure, increments δa_l are found by solving the system of linear equations

$$\sum_{l=1}^{M} a'_{kl} \delta a_l = \beta_k. \tag{2.10}$$

Here, a'_{kl} represents a Hessian matrix with modified main diagonal $a'_{jj} = a_{jj}(1 + \lambda)$ which is also called the curvature matrix, while β_k is proportional to the Jacobian matrix of the first partial derivatives. The damping parameter λ influences both the direction and the size of the increments δa_l. If λ is high, the Levenberg-Marquardt algorithm operates in a similar way as the steepest descent method and approaches the Gauss-Newton method if its value is small. We use a modified, fast version of the Levenberg-Marquardt algorithm developed by Piskunov & Kochukhov (2002) that additionally adjusts the value of λ within each iteration step to speed up the calculations, keeping the right-hand side of Eq. 2.10 and the Hessian matrix a_{kl} unchanged.

We used the described algorithm to optimize basic stellar and orbital parameters. These are the effective temperatures T_1 and T_2 and the RV semi-amplitudes K_1 and K_2 of the primary and secondary, the radius R_1 and the $v_1 \sin i$ of the primary, the orbital inclination i, and the γ-velocity of the system.

2.2.6   Non-radial pulsations

Besides the derivation of stellar and system parameters, we want to investigate the influence of the pulsations of the primary components of the oEA stars on the observations, in particular during the eclipse phases. For that purpose we use the Shellspec07_inverse program to model the spatial filtration effect on the observed RVs for different combinations of l and m wavenumbers. This paragraph describes the mathematical background. Our actual model is limited to the surface velocity perturbations caused by the non-radial pulsations and does not include the temperature and surface area perturbations.

Non-radial pulsations cause both radial and horizontal motions of the mass elements. If a star oscillates only in radial direction, i.e. expands and contracts radially with time, it is said to show *radial pulsations*. In this case, the stellar oscillations are characterized by frequency, amplitude and phase, and by the number n of radial *nodal lines* located between the center and the surface of the star. A nodal line, or simply *node*, represents the line where the mass elements do not move during the oscillation cycle. In the case that also horizontal motions occur, one says that non-radial oscillations are observed. This type of oscillations is characterized by two additional wavenumbers l and m which represent the total number of surface nodes and the number of nodes passing through the poles of the star, respectively.

The perturbations are described in terms of spherical harmonics $Y_l^m(\theta, \varphi)$ of degree l and azimuthal wavenumber m. θ is the stellar latitude and φ the longitude. The displacement of a mass element from its equilibrium position is described by the vector $\vec{A}$, it is

$$\vec{A} = (A_r \vec{e_r} + A_\theta \vec{e_\theta} + A_\varphi \vec{e_\varphi}) \exp(-i\omega t), \tag{2.11}$$

where the frequency $\omega = \omega_R + i\omega_I$ is complex. Its imaginary part describes an excitation or damping of the oscillation mode. A_r is the radial and A_θ and A_φ are the horizontal components, defined as

$$A_r = \xi_r(r) Y_l^m$$
$$A_\theta = \xi_h(r) \frac{dY_l^m}{d\theta}$$
$$A_\varphi = \frac{\xi_h(r)}{\sin \theta} \frac{dY_l^m}{d\varphi}. \tag{2.12}$$

ξ_r and ξ_h are the radial and horizontal displacement amplitudes. For a spherically symmetric star, $Y_l^m(\theta, \varphi)$ gives the dependence of the perturbations on θ and φ. It is defined by

$$Y_l^m(\cos\theta, \varphi) = C_{lm} P_l^{|m|}(\cos\theta) \exp(im\varphi), \tag{2.13}$$

where $P_l^{|m|}$ is the associated Legendre polynomial, and C_{lm} is a normalization constant. The associated Legendre polynomial is related to the Legendre polynomial P_l via

$$P_l^{|m|}(x) = (-1)^m \left(1 - x^2\right)^{m/2} \frac{d^m P_l(x)}{dx^m}, \tag{2.14}$$

where

$$P_l(x) = \frac{1}{2^l l!} \frac{d^l \left(x^2 - 1\right)^l}{dx^l}. \tag{2.15}$$

The normalization constant is

$$C_{lm} = (-1)^{\frac{m+|m|}{2}} \sqrt{\frac{(2l+1)(l-|m|)!}{4\pi(l+|m|)}}. \tag{2.16}$$

In practice, recursive relations are used to calculate the associated Legendre polynomials. Starting with a sectoral mode ($l=m$)

$$P_m^m(x) = (-1)^m \frac{(2m)!}{2^m m!} \left(1-x^2\right)^{m/2}, \tag{2.17}$$

one computes the associated Legendre polynomial of degree l from

$$P_{l+1}^m(x) = \frac{(2l+1)}{(l-m+1)} x P_l^m(x) - \frac{(l+m)}{(l-m+1)} P_{l-1}^m(x), \tag{2.18}$$

with $P_{l-1}^m(x){=}0$ if $l{=}m$. For the calculation of the derivatives one can use

$$\left(1-x^2\right) \frac{dP_l^m}{dx} = l x P_l^m(x) - (l+m) P_{l-1}^m(x). \tag{2.19}$$

Alternatively, Eq. 2.11 and 2.12 can be written as

$$\vec{A} = C_{lm} \left(A_r' \vec{e_r} + A_\theta' \vec{e_\theta} + A_\varphi' \vec{e_\varphi} \right) \exp\left(-\omega_I t\right) \tag{2.20}$$

with

$$\begin{aligned}
A_r' &= \xi_r(r) \cos\left(m\varphi - \omega_R t\right) P_l^m \\
A_\theta' &= \xi_h(r) \cos\left(m\varphi - \omega_R t\right) \frac{d}{d\theta}\left(P_l^m\right) \\
A_\varphi' &= \xi_h(r) \frac{P_l^m}{\sin\theta} \frac{d}{d\varphi}[\cos\left(m\varphi - \omega_R t\right)].
\end{aligned} \tag{2.21}$$

From Eq. 2.19 and 2.21 we obtain

$$\begin{aligned}
A_r' &= \quad \xi_r \cos\left(m\varphi - \omega_R t\right) P_l^m \\
A_\theta' &= \quad \xi_h \cos\left(m\varphi - \omega_R t\right) \frac{1}{\sin\theta} \left[(l+m) P_{l-1}^m - l\cos\theta P_l^m\right] \\
A_\varphi' &= -\xi_h \sin\left(m\varphi - \omega_R t\right) \frac{m}{\sin\theta} P_l^m.
\end{aligned} \tag{2.22}$$

The velocity field calculates from $\vec{v} =\mathrm{d}\vec{A}/\mathrm{d}t$, and finally we get

$$\vec{v} = C_{lm} \left(v_r \vec{e_r} + v_\theta \vec{e_\theta} + v_\varphi \vec{e_\varphi} \right) \exp \omega_I t \tag{2.23}$$

with the velocity components

$$\begin{aligned}
v_r &= \xi_r \omega_R \sin\left(m\varphi - \omega_R t\right) P_l^m \\
v_\theta &= \xi_h \omega_R \sin\left(m\varphi - \omega_R t\right) \frac{1}{\sin\theta} \left[(l+m) P_{l-1}^m - l\cos\theta P_l^m\right] \\
v_\varphi &= \xi_h \omega_R \cos\left(m\varphi - \omega_R t\right) \frac{m}{\sin\theta} P_l^m.
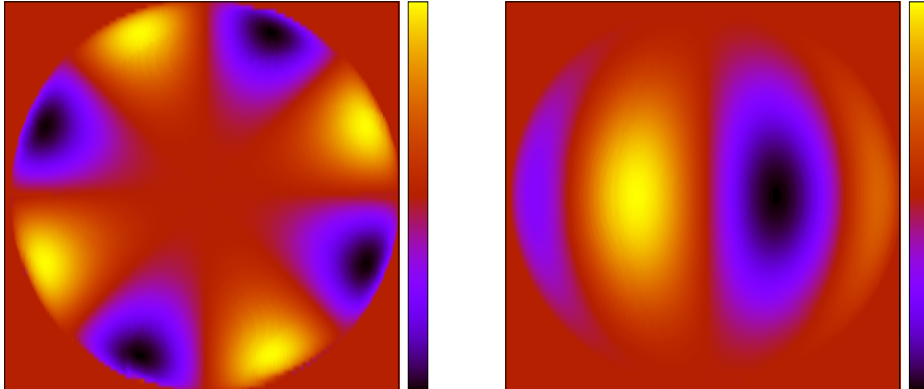\end{aligned} \tag{2.24}$$

Figure 2.7: The RV surface field of a non-rotating star caused by the sectoral pulsation mode $(l, m) = (4, 4)$. Yellow and blue regions indicate positive and negative RVs, respectively. Red regions have close to zero velocity, indicating the nodal lines. In the left panel, the star is seen pole-on, and equator-on in the right panel.

So far, the pulsations have been described in spherical coordinates. Its implementation into Shellspec07_inverse requires the transformation from spherical to Cartesian coordinates and vice versa. We start on a grid of Cartesian coordinates in the line-of-sight system. For the calculation of the non-spherical shape of the secondary and the surface flux distributions, the coordinates of the grid points are transformed into the body frozen system and the desired values are interpolated from the values calculated in the body frozen grid. For the implementation of pulsations, the line-of-sight coordinate system is tilted for the inclination angle i so that the pulsation axis is aligned with the normal to the orbital plane and the velocity field due to the oscillations is computed in the corresponding spherical coordinates. At this point, there is no need for further coordinate transformations as long as we consider synchronous rotation and that the rotation axis of the primary is aligned to the normal of the orbital plane, as we will assume in this simple approach. The components of the velocity field in the Cartesian coordinates are then obtained from

$$
\begin{aligned}
v_x &= v_r \sin\theta \cos\varphi + v_\theta \cos\theta \cos\varphi - v_\varphi \sin\theta \sin\varphi \\
v_y &= v_r \sin\theta \sin\varphi + v_\theta \cos\theta \sin\varphi + v_\varphi \sin\theta \cos\varphi \qquad (2.25) \\
v_z &= v_r \cos\theta - v_\theta \sin\theta.
\end{aligned}
$$

and the final values in the line-of-sight system follow from the back-rotation by the angle i according to Eq. 2.4. The y is then simply the z-component of the velocity field.

Figure 2.7 shows an example of the RV field on the stellar surface caused by a sectoral oscillation mode of degree l=4. It was computed with the Shellspec07_inverse program for two different inclination angles i of the rotation axis to the line-of-sight, showing the star pole-on (i=0) and equator-on (i=90°).

2.3   Additional software used for the spectral analysis

This section gives a short description of additional computer programs that have been used in the present work, including the KOREL program (Hadrava 1995, 2004a) used for the

decomposition of the spectra of the single components and the determination of the orbital elements, the SynthV program (Tsymbal 1996) for the calculation of synthetic spectra and to build libraries of intrinsic line profiles needed by Shellspec07_inverse, and the LLmodels program (Shulyak et al. 2004) used for the calculation of atmosphere models of the early-type primary components.

2.3.1   The KOREL program

The KOREL program (Hadrava 1995, 2004a) is a Fourier transform based computer code that works with time series of spectra of multiple systems. It allows for the simultaneous decomposition of the composite spectra into the spectra of the components, the determination of the RVs from the shifts that are applied to the single input spectra to build the decomposed spectra, and for the determination of the orbital elements for up to five stars in up to 4 hierarchical orbits. If necessary, it also determines the timely variation of the line strengths of the components. The last capability is in particular useful for the investigation of eclipsing stars, where the line strengths of the components vary strongly during the eclipses. It can be used as well to remove the timely varying contributions of telluric lines from the stellar spectra. After applying the heliocentric RV correction to the observed spectra, the telluric lines that originate in the earth atmosphere are included into the model as the lines of an additional star of negligible mass, moving in the apparent orbit of the sun.

   KOREL is not able to yield the individual continua of the decomposed spectra which are normalized to the common continuum of the multiple system. Thus, it is necessary to renormalize the output spectra using additional information, e.g., from the photometry of the stars. A renormalization method is described in Hadrava (2004a) and will be discussed in Chapters 4 and 5 in the context of the application to the target stars.

2.3.2   The SynthV program

SynthV is a Fortran 90 code developed by Tsymbal (1996) for the calculation of synthetic spectra of stars of all spectral types and arbitrary wavelength ranges. The calculation is based on pre-computed atmosphere models that describe the distribution of physical quantities like temperature, pressure, etc. with optical depth. The program assumes a plane-parallel structure of the atmosphere and local thermodynamic equilibrium (LTE). LTE means that at each point of the stellar atmosphere and for all frequencies ν a local temperature T can be defined such that the emission E_ν is given by Kirchhoff's law $E_\nu = A_\nu B_\nu(T)$, where A_ν is the absorption and B_ν is the Planck function. A system is not in LTE if the local kinetic temperature is not equal to the Planckian temperature.

   The parameters of atomic lines used by SynthV are usually taken from the VALD database (Kupka et al. 2000). Synthetic spectra are computed with constant steps in wavelength and all line profiles are approximated by Voigt functions. SynthV allows for the computation of synthetic spectra based on individual elemental abundances. Temperature, pressure, and electron number density distributions with optical depth are taken from a pre-computed atmosphere model which in turn depends on the chosen elemental abundances. Thus, in practice, the atmosphere model and the synthetic spectrum are determined in an iterative procedure. Its application to our target stars is described in Chapter 5.

In its original version, the SynthV program computes specific intensities for seven different angles θ between the line-of-sight and the normal to the visible stellar disk. These intensities are then convolved with rotation, macro-turbulence and the instrumental profile. We extended the number of points on the stellar disk from seven to nine. This is sufficient for using our new procedure to compute the limb darkening as described in Section 2.2.

2.3.3   The LLmodels program

The LLmodels program (Shulyak et al. 2004) was established for the calculation of LTE plane-parallel atmosphere models of early and intermediate spectral type stars. It is based on the so-called ”line-by-line“ method which provides a direct calculation of the line opacity on a fine wavelength grid taking the contributions from neighboring lines into account. A fine grid means a grid of about 0.1 Å step width. Shulyak et al. (2004) showed that there is almost no difference between temperature distributions of models computed with smaller step sizes but that the difference rapidly increases for wider grids reaching a value of up to 100 K in the upper atmospheric layers. The continuum absorption coefficient, on the other hand, can be computed with sufficient accuracy using a step size of 1 Å. Most of the spectral lines cover only a small wavelength range, thus the total opacity at the considered wavelength point is computed by summarizing the opacities from all lines within a range of only ± 2.5 Å. Wide spectral lines like the hydrogen or Ca II H and K lines are treated in a different way where the central regions around the line cores are computed on a fine grid, whereas for the outer wings a step width of 1 Å is used like in the case of the continuum. The list of atomic lines is provided by the VALD database (Kupka et al. 2000).

The two criteria used for the convergence of the model are the constancy of the total flux and the conservation of the radiative equilibrium. Both criteria are checked in each iteration for each atmospheric layer, and the model is assumed to converge if both are fulfilled. The reason to use two criteria is that the total flux constancy alone is not very sensitive to temperature changes in optically thin layers (Shulyak et al. 2004).

The ”line-by-line“ technique does not rely on any statistical methods, like e.g. in the case of the Opacity Distribution Function (ODF) by Gustafsson et al. (1975) or Kurucz (1979), and is free of approximations with respect to the line opacity calculations. It allows for the calculation of atmosphere models using individual abundances with a vertical stratification of the chemical elements in a reasonable time. The ODF technique, for instance, uses pre-tabulated line opacities and requires in the case of elemental stratification the calculation for each atmospheric layer based on the given abundances. It is obvious that such a procedure is much more time consuming.

Chapter 3

Observations and data reduction

3.1   Observations

396 spectra of TW Dra were obtained in April/May 2007 and 479 spectra in March/April 2008. The spectra were taken with the Coude Echelle spectrograph at the 2-m telescope of the Thüringer Landessternwarte Tautenburg (TLS) and with the BOES spectrograph at the 1.8-m telescope of the Bohyunsan Optical Astronomy Observatory (BOAO). RZ Cas was observed at TLS during 2001 and 2006, the data sets contain 951 and 512 spectra, respectively.

The Tautenburg spectrograph is a classical high-resolution Echelle spectrograph working in the Coude focus. Its spectral resolution depends on the chosen width of the entrance slit. A description of the instrument can be found at http://www.tls-tautenburg.de. BOES (BOhyunsan Echelle Spectrograph) is a fiber-fed high-resolution Echelle spectrograph using five fibers of different diameters and corresponding spectral resolutions. A description of the instrument can be found at http://arcsec.sejong.ac.kr.

The TLS spectra have a spectral resolution of 33 000 and cover the wavelength range from 4 700 to 7 400 Å. The BOES spectra have a spectral resolution of 50 000 and cover a larger wavelength range down to 3 600 Å. The typical exposure time was 10 min., the spectra have a typical signal-to-noise ratio of 100. Table 3.1 gives the journal of observations for both stars. The most extended period of continuous observations without gaps comprises 15 consecutive nights in 2007 for TW Dra, and 6 nights in 2001 for RZ Cas.

3.2   Spectrum reduction

The spectrum reduction was completed using standard ESO-MIDAS packages and some special programs developed at TLS. First, the bias and the stray-light was subtracted from the spectra using bias frames taken with zero exposure time as well as the information from the inter-order space in the spectra of the stars. Cosmic rays have been removed by applying a special filter that was adjusted to the given gain and readout-noise of the used CCD. For the flat fielding, i.e. the elimination of the pixel-to-pixel sensitivity variation of the CCD by dividing the stars spectra by the so-called flat field spectra, we used the continuum spectra of halogen lamps placed in front of the telescope. After the positions of the Echelle orders had been determined from the flat field spectra, the Echelle orders have been extracted from the stellar spectra using an optimized procedure with variable extraction slit width that was

Table 3.1: Journal of observations. N is the number of spectra obtained in single nights.

date	N	source	date	N	source	date	N	source
				TW Dra				
2007/04/24	17	TLS	2007/05/07	42	BOAO	2008/03/28	15	TLS
2007/04/25	20	TLS	2007/05/08	19	BOAO	2008/03/29	42	TLS
2007/04/26	32	TLS	2007/05/10	9	BOAO	2008/03/30	12	TLS
2007/04/27	20	TLS	2008/03/17	2	TLS	2008/04/16	43	TLS
2007/04/28	14	TLS	2008/03/18	2	TLS	2008/04/17	24	TLS
2007/04/29	11	TLS	2008/03/21	3	TLS	2008/04/18	3	TLS
2007/04/30	13	TLS	2008/03/23	3	TLS	2008/04/20	28	TLS
2007/05/01	33	TLS	2008/03/24	40	BOAO	2008/04/22	1	TLS
2007/05/02	49	TLS	2008/03/24	1	TLS	2008/04/23	40	TLS
2007/05/03	40	TLS	2008/03/25	2	TLS	2008/04/24	17	TLS
2007/05/04	30	TLS	2008/03/26	69	BOAO	2008/04/25	24	TLS
2007/05/05	29	TLS	2008/03/27	19	BOAO	2008/04/26	40	TLS
2007/05/06	18	TLS	2008/03/27	12	TLS	2008/04/27	37	TLS
				RZ Cas				
2001/09/30	112	TLS	2001/10/10	85	TLS			
2001/10/03	9	TLS	2001/10/11	32	TLS			
2001/10/04	103	TLS	2001/10/12	142	TLS	2006/01/09	123	TLS
2001/10/05	85	TLS	2001/10/13	153	TLS	2006/01/10	128	TLS
2001/10/06	27	TLS	2001/10/14	125	TLS	2006/05/08	36	TLS
2001/10/07	82	TLS	2005/12/13	21	TLS	2006/05/09	37	TLS
2001/10/09	7	TLS	2006/01/08	101	TLS	2006/05/10	52	TLS

adjusted to the signal-to-noise in the different orders. The normalization to the continuum was done by a special procedure working in the pixel-order plane. This procedure has the advantage that it fits the local continuum to the observed absorption spectra in two dimensions using also the cross-order information. In this way, the broad Balmer lines extending over more than one Echelle order can be fitted as well. For the wavelength calibration we used a Th-Ar lamp. The wavelengths of its emission lines were taken from a standard list that was optimized for a resolution of 30 000 and kindly supplied by Herman Hensberge from the Royal Observatory of Belgium in Brussels. All spectra were corrected in wavelength for nightly instrumental shifts by comparing the positions of a large number of telluric O_2 lines with the corresponding laboratory wavelengths. The accuracy in the radial velocity determination achieved in this way is of about 70 m s^{-1} for a single spectrum for both target stars.

Chapter 4

Spectroscopic analysis of RZ Cas

The analysis of the RZ Cas system is based on time-series of high-resolution spectra taken in two different epochs of observations. We start with the KOREL program (Hadrava 2004a) to compute the decomposed spectra of the components and to derive an orbital solution that includes both stars (§ 4.1). A detailed analysis of the disentangled spectra using synthetic spectra calculated with the SynthV program (Tsymbal 1996) yields the chemical abundances of the components. The abundances and the derived stellar and system parameters (§ 4.2) are used as the starting values for a fine-tuning with the Shellspec07_inverse program based on our assumed model (§ 4.3). A discussion of the obtained results will be given in § 4.4.

4.1   Determination of basic parameters using KOREL

We used KOREL (Hadrava 2004a), a Fourier transform based program that calculates the optimum orbital elements and the mean decomposed spectra of the components of multiple systems from a time series of spectra as described in § 2.3.1. From both data sets obtained in 2001 and 2006, we selected all spectra of S/N>60. The analysis based on the wavelength range 4950-5680 Å. The conversion from the wavelength to the RV scale resulted in $8\,192$ bins of $5\ \mathrm{km\,s^{-1}}$ each, corresponding to a spectral two-pixel resolution of $30\,000$.

4.1.1   Orbital solutions

We started by analyzing the two data sets from 2001 and 2006 separately, assuming circular orbits and allowing for variable line strengths in the solution. The upper two panels in Figure 4.1 show the RVs of the primary (black) and the secondary (red) derived from the spectra taken in 2001 and 2006 and folded with the corresponding orbital periods. The solid curves show the calculated orbital solutions, the zero phase corresponds to the phase of maximum separation. The Rossiter effect in the RVs of the primary at the primary eclipse is clearly evident. In both 2001 and 2006, a stronger deviation in the RVs from those expected on the basis of Keplerian motion can also be seen in a broad region around the secondary minimum. These regions are too extended to be caused by the Rossiter effect during secondary eclipse. We discuss the underlying effect in more detail in § 4.3. Besides this large-scale deviation, the RVs obtained from the spectra taken in 2001 show variations over short ranges in orbital phase that cannot be found in the data from 2006. The bottom
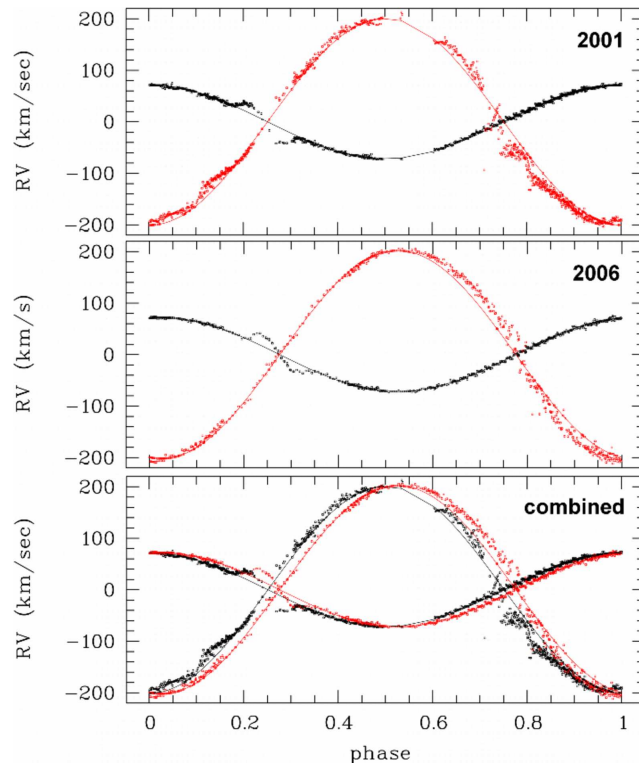
Figure 4.1: RVs of RZ Cas determined with KOREL, shown for the observations in 2001 and 2006 and folded with the corresponding orbital periods, and for the combined solution folded with the orbital solution derived from the spectra taken in from 2006.
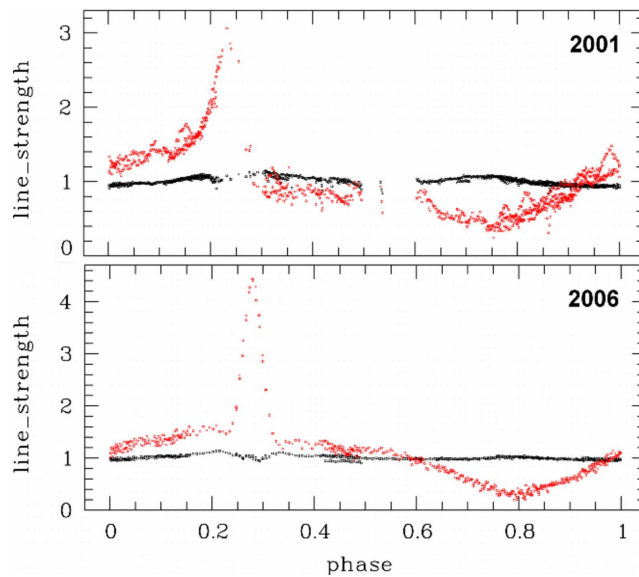

Figure 4.2: Line strength variations of the primary (black) and the secondary (red) of RZ Cas calculated with KOREL for the spectra taken in 2001 and 2006.

Table 4.1: Orbital elements of RZ Cas derived with KOREL and by Lehmann & Mkrtichian (2008a).

	2001	2006	combined	L&M (2008)	
P	1.19501(15)	1.195232(20)	1.195243(19)	1.1952410(77)	d
K_1	71.55(26)	71.72(25)	72.01(25)	71.311(78)	$\mathrm{km\,s^{-1}}$
K_2	200.50(69)	201.91(60)	199.03(59)	—	$\mathrm{km\,s^{-1}}$
q	0.3569(25)	0.3552(23)	0.3618(23)	—	
T	2193.39011(59)	3866.746(75)	2193.38931(57)	2193.38482(20)	
$\dot{P}$	—	—	0.66(39)	0.37(16)	$\mathrm{s\,y^{-1}}$
$\dot{K}$	—	—	−0.104(87	−0.135(27)	$\mathrm{km\,s^{-1}\,y^{-1}}$

panel of Figure 4.1 shows the RVs of both components for the data obtained in 2001 (black) and 2006 (red) folded with the period observed in 2006. The observed shift in orbital phase between the two data sets can be explained by a shift in the orbital period, as we will show below.

Figure 4.2 shows the variations in relative line strengths during both epochs of observation. Whereas the increase in the line strength of the secondary during the primary eclipse is expected from the obscuration of the light of the primary, its decrease during the secondary eclipse covers a region in orbital phase that is much broader than the duration of the eclipse and resembles the region of the RV deviations as discussed before.

Table 4.1 lists the derived orbital elements. T refers to the time of primary minimum (2 450 000+). The results obtained by Lehmann & Mkrtichian (2008a) are given for comparison. The KOREL program does not allow to determine the errors in the deduced parameters. For that reason, we applied a separate program based on the method of differential corrections to the RVs derived with KOREL to estimate the errors in the orbital elements. They are given in Table 4.1 in parentheses, in units of the last digits.

The derived values of the orbital period in the two epochs of observation differ significantly, as already reported by Lehmann & Mkrtichian (2008a), where the authors determined the RVs of only the primary from the cross-correlation with a template spectrum. For an additional check, we computed the orbital solution with KOREL from the combined 2001 and 2006 data allowing for a linear trend in orbital period and RV semi-amplitudes. We obtained a rate of period change of $\dot{P}$=(0.66±0.39) s y^{-1} and $\dot{K}$=(0.104±87) km s^{-1} y^{-1} for the change in RV semi-amplitudes (Table 4.1). We assume that the large error of $\dot{P}$ results from the short time base of 7 days of the observations in 2001 (see also the large error in P obtained from the 2001 data) and, in contrast to the results obtained in Lehmann & Mkrtichian (2008a), that the variation in the K-values is non-significant. From the difference of 1583 d between the two epochs of observations we calculate that the orbital period changed by (2.9±1.7) s during the total period of 5 years.

Alternatively, the period change can also be determined by using the phase shift information. In this case, the accuracy does not depend on the duration of the observing periods but on the time span Δt between the two epochs. In our case, the period change can be

much more precisely determined in this way. If we observe an orbital period of P in 2001 and of $P+\Delta P$ in 2006 and fold the RVs measured from both epochs with $P+\Delta P$, we obtain a phase shift of

$$\Delta\phi = \frac{2\pi}{P}\frac{\Delta P}{P}\Delta t \qquad (4.1)$$

between the RVs from 2006 and 2001. It follows that

$$\Delta P = 86\,400\frac{P^2}{\Delta t}\frac{\Delta\phi}{2\pi}, \qquad (4.2)$$

where ΔP is in seconds and both the period and epoch difference are in days. In the bottom panel of Figure 4.1, we folded all RVs in this way using the period from 2006. We observe a phase shift of $\Delta\phi/2\pi = 0.026$. Assuming an error in the derived phase shift of 0.001 and an error in the epoch difference of 10% of the longer period of observations (29 d in 2006), we deduce an orbital period change of $(2.0\pm0.1)\,\mathrm{s}$.

4.1.2   Decomposing of spectra

We used all spectra obtained outside the primary minimum in 2006 to compute the mean spectrum of the primary, and all spectra outside the secondary eclipse for the mean spectrum of the secondary. We preferred to use only the spectra from 2006 because the RVs obtained in 2001 show distortions, presumably related to accretion structures that appeared during or shortly after a phase of rapid mass transfer. For the secondary, we also rejected all spectra with a deviation of the individual RVs from the orbital curve larger than $7\,\mathrm{km\,s^{-1}}$ to exclude the spectra in a larger range around the secondary eclipse where we observed a deviation of the RV curve from a Keplerian one. Finally, we had 470 spectra of the primary and 247 spectra of the secondary at our disposal to build the decomposed spectra with KOREL.

The composed KOREL output spectra are normalized to the common continuum of both stars, as it is the case for the composite input spectra. The normalization to the individual continua was completed by using the *uvby* luminosities derived from the Stroemgren photometry of RZ Cas by Mkrtichian et al. (2010). From an interpolation of the *uvby* luminosity ratios (the WD solution with hot spot in Mkrtichian et al. (2010)), we derived

$$\alpha = \frac{C_2}{C_1} = -0.1456 + 4.100 \times 10^{-5}\mathring{A}^{-1} \cdot \lambda \qquad (4.3)$$

for the wavelength dependence of the continuum flux ratio of the two stars in the considered spectral range. The decomposed spectra R'_i have been normalized according to

$$R_i = 1 - (1 + \alpha_i)\left(1 - R'_i + \Delta_i\right), i = 1, 2 \qquad (4.4)$$

where $\alpha_1 = \alpha$ for the primary and $\alpha_2 = \alpha^{-1}$ for the secondary. Δ_i are the a priori unknown shifts of the KOREL output spectra (see Hadrava (2004a)). They were first adapted to provide the best (most reliable) local continua of the normalized spectra and fine-tuned in a later step of the analysis.
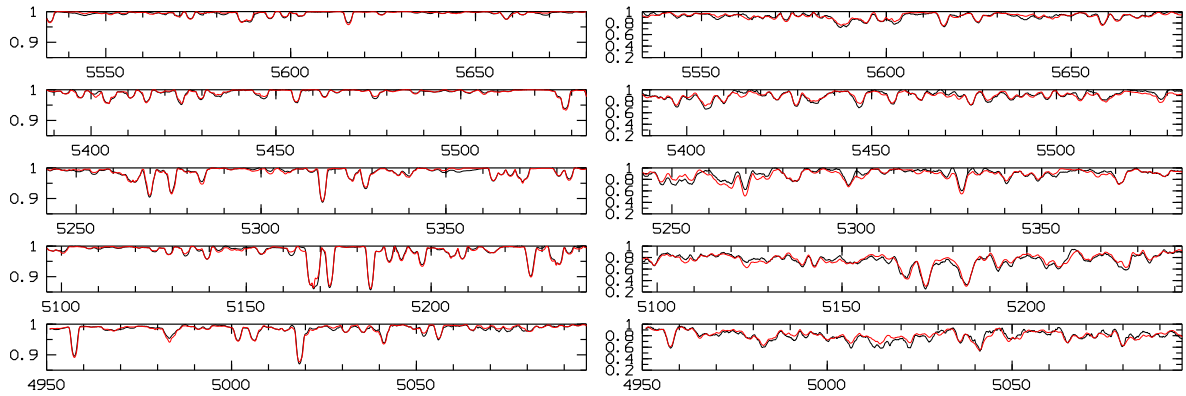
Figure 4.3: Observed (black) and calculated (red) spectra of the primary (left) and the secondary (right) of the RZ Cas system.

4.2   Spectrum analysis with SynthV

The synthetic spectra were calculated with the SynthV program (Tsymbal 1996) (see § 2.3.2). The atomic line list was taken from the VALD database (Kupka et al. 2000). The model atmosphere for the hot primary was calculated with the LLmodels program (Shulyak et al. 2004) (see § 2.3.3), whereas we used MARCS atmosphere models (Gustafsson et al. 2008) and included an additional molecular line list taken from the Kurucz CDs (Kurucz 1995) for the cool secondary. For both the primary and the secondary, we fixed the $\log g$ to the values of 4.35 for the primary and 3.7 for the secondary obtained from the photometry (Lehmann & Mkrtichian 2008a). We used T_{eff}, v, $v \sin i$, and the elemental abundances as free parameters in general. In the case of the primary, we also iterated the value of the micro-turbulent velocity ξ_{turb}, whereas it was impossible to disentangle $v \sin i$ and ξ_{turb} for the late-type secondary with its non-spherical configuration and not so well determined continuum. We therefore fixed its micro-turbulent velocity to $2 \, \mathrm{km \, s^{-1}}$. To correct for the unknown shifts Δ_i of the continua of the decomposed spectra in a more accurate way than described in the previous section, we used corrections to the already applied shifts as additional free parameters in the least-squares fit of the observed by the synthetic spectra. The resulting corrections have always been very small, so in principle they could be neglected.

Figure 4.3 shows the observed and calculated spectra. It shows that the spectrum observed for the primary is almost perfectly fitted. The fit is not as good in the case of the secondary, mainly because of the larger uncertainties in determining the observed local continuum of this late-type star. Also the stellar parameters obtained from the best fit of the spectrum of the secondary are not as well constrained. This comes from the fact that the spectrum of the cool secondary is dominated by the Fe I lines which have a low sensitivity to temperature changes in the range of 4 500 to 5 000 K. For the primary, we obtained $v \sin i = (66.0 \pm 0.5) \, \mathrm{km \, s^{-1}}$, $\xi_{\mathrm{turb}} = (3.0 \pm 0.2) \, \mathrm{km \, s^{-1}}$, and $T_{\mathrm{eff}} = (8\,850 \pm 25)$ K, with $\log g$ fixed to 4.35. Table 4.2 lists the deviations of the derived abundances from solar, the mean error of measurement is 0.03 dex. The Si abundance of the primary is depleted by a factor of 2.5, all other abundances are close to the solar values. For the secondary, we found $v \sin i = (81 \pm 2) \, \mathrm{km \, s^{-1}}$ and $T_{\mathrm{eff}} = (4\,800 \pm 100)$ K, with $\log g$ fixed to 3.7. Fe is underabundant

Table 4.2: Derived surface abundances of RZ Cas relative to standard solar values in dex. Positive values mean enhancement.

primary									
C	-0.03	O	-0.13	Mg	+0.14	Si	-0.39	Ca	-0.13
Sc	+0.09	Ti	-0.09	Cr	-0.08	Fe	-0.16	Ni	-0.11
secondary									
Na	+0.2	Mg	±0.0	Ca	±0.0	Ti	+0.1		
Cr	-0.6	Mn	+0.1	Fe	-0.4	Ni	-0.2		

by a factor of about 3 and Cr by a factor of 4, all other abundances are close to the solar values (Table 4.2). The mean error of measurement is 0.1 dex.

4.3   Spectroscopic modeling of RZ Cas

Lehmann & Mkrtichian (2008a) did a first attempt to model the composite spectrum of RZ Cas, based on simple approximations like spherical configurations of both stars and Gaussian intrinsic line profiles. In the present work, we use the Shellspec07_inverse program described in Section 2.2 for modeling the spectral line profiles of RZ Cas at arbitrary orbital phases including the eclipses by taking the non-spherical shape and the gravity darkening of the secondary component into account. Since the program is based on the Shellspec07 code that can handle an optical thin accretion disk and a gas stream, we used this possibility to include circumstellar matter formed in the active phase of the system in 2001 into our model and to study its effects on the observed line profiles.

4.3.1   Application to the spectra from 2006

According to the conclusion drawn in Lehmann & Mkrtichian (2008a) that the star was in a quiet state in 2006, we started with the analysis of the mainly undisturbed spectra taken in 2006 by including only the two stars into the model, without considering any effects coming from the circumbinary matter. We neglect the deviation of the primary from spherical shape and assume that the secondary fills its Roche lobe and rotates synchronously to its motion in a circular orbit.

For the analysis, we averaged the 512 spectra of RZ Cas into 100 orbital phase bins based on the derived orbital period and focused onto the four most unblended, stronger metal lines, which are Fe I 4957, 5056, 5616, and 5625 Å. We already showed the phase-binned observed profiles of one of these lines folded with the orbital period and the computed synthetic lines in Figure 2.2. The Rossiter effect is clearly evident in both panels of this figure as the S-shaped distortion of the line profiles at the phase of the primary eclipse. Figure 4.4 shows the results obtained by using different gravity darkening exponents for the cool secondary. We give the surface intensity distribution in the left row of panels. The intensity is in $\mathrm{erg\,cm^{-2}\,s^{-1}\,Hz^{-1}\,rad^{-1}}$ on a logarithmic scale, distances are in units of the separation of the components. The center row shows the O-C line intensity residuals for the

Fe I 4957 Å profiles obtained in 2006, and the right row those for 2001. For the gravity darkening exponent of the Roche lobe filling secondary, we first assumed the value of $\beta=0.08$ as predicted by the theory in the case of a star with a convective envelope (Lucy 1967). This model results in a smooth solution for all orbital phases except for a larger region around secondary minimum, that appears to be brighter (which means that the calculated line of the secondary is stronger than the observed one). This brightening, covering about one fifth of the orbit, corresponds to an attenuation of the light of the secondary, as already found for the same region by Lehmann & Mkrtichian (2008a) and that can also be seen in form of a deviation of the RVs from the Keplerian orbital curve in our KOREL solution (Figure 4.1). The χ^2 of the Levenberg-Marquardt solution including all orbital phases is 2.21.

In the next step, we tried to model the observed deviations in the region around secondary minimum assuming that they are caused by some intrinsic property of the secondary itself. The most reliable explanation may be that the star shows a different temperature distribution on its surface than we assumed in our first model. We therefore examined whether an adjustment of the gravity darkening exponent would improve the χ^2 of our spectroscopic solution. Figure 4.4 d shows the residuals in the case of $\beta=0.5$ (for a discussion of such an ultra-high value see Section 4.4). The model fits the observed line profiles in the region around secondary minimum well but completely fails at phases close to the primary eclipse, where the calculated line profiles are much too weak and a dark region in the O-C frame appears. The resulting χ^2 of 2.56 is higher than the value derived for $\beta=0.08$.

Finally, we divided the stellar surface of the secondary into two regions by using $\beta=0.5$ for the hemisphere pointing towards the primary and the normal value of $\beta=0.08$ for the opposite side (Figure 4.4 e). The previously bright region around secondary minimum is now almost perfectly fitted and no difference with respect to the first solution ($\beta=0.08$ for the entire surface) can be seen in the O-C distribution around primary minimum (Figure 4.4 f). The resulting χ^2 is 1.93. The remaining, faint structures in the O-C distribution are caused by the outermost parts of the wings of the lines of the primary where the observations show a slightly smoother transition than the calculated profiles, i.e. the sharp edges of the ellipse-shaped rotation profiles are smeared out in the observed profiles.
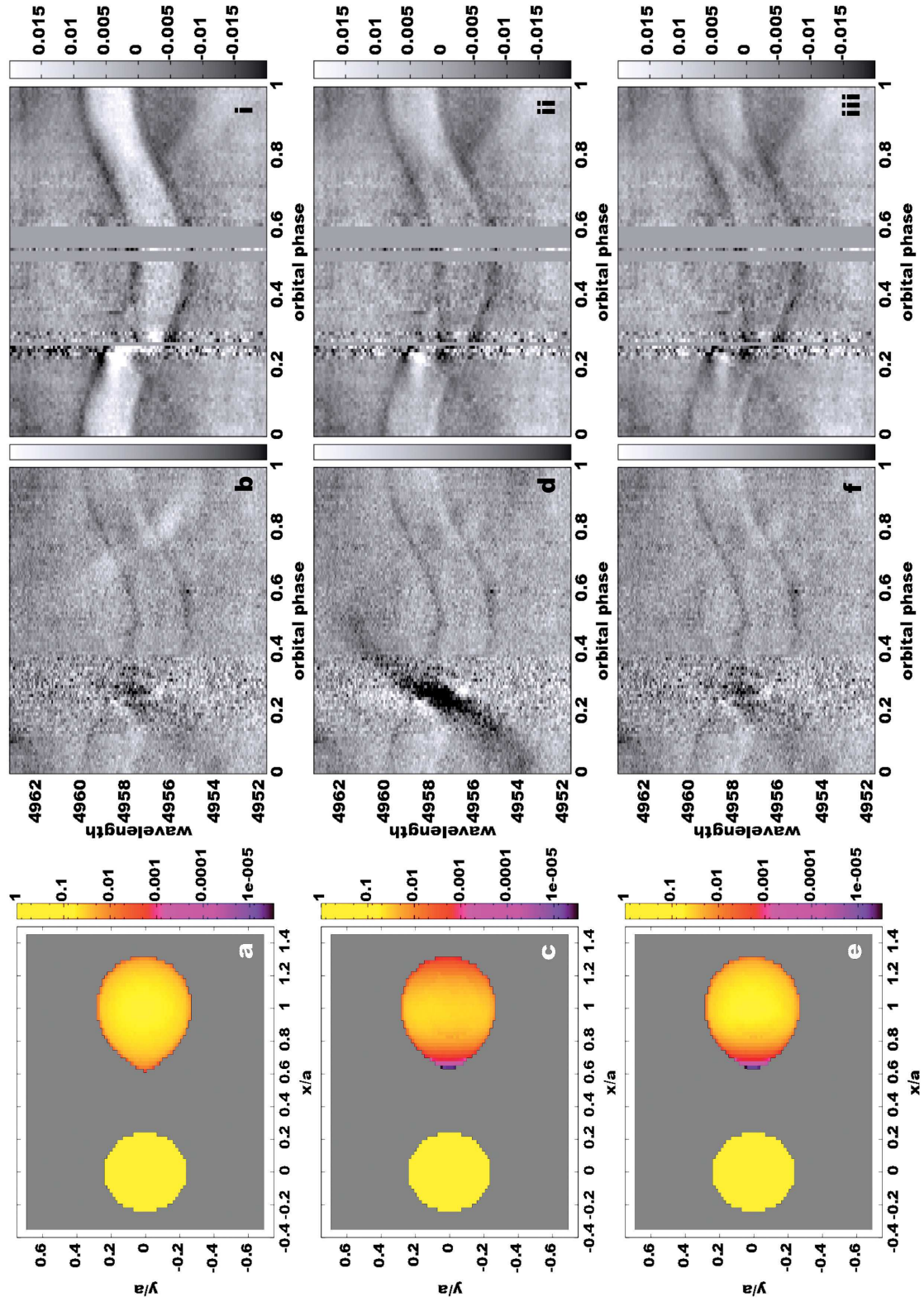
Figure 4.4: **Left column:** Surface intensity distributions of the secondary based on $\beta=0.08$ (a), $\beta=0.5$ (c), and on the combined model (e). **Middle column:** Corresponding O-C line intensity residuals for the spectra from 2006, folded with the orbital period. **Right column:** O-C values for the spectra from 2001, based on the final solution for 2006 (i), including a homogeneous disk (ii), and a disk of variable density (iii).

Table 4.3: Parameters of the RZ Cas system derived with Shellspec07_inverse.

T_1	T_2	$\log g_1$	$\log g_2$	R_1	R_2	M_1	M_2	q	a	i
(K)	(K)			$(R_\odot)$	$(R_\odot)$	$(M_\odot)$	$(M_\odot)$		$(R_\odot)$	(deg)
8907(15)	4797(20)	[4.35]	[3.7]	1.61(1)	1.93	2.01(2)	0.69(1)	0.342(2)	6.59(3)	82.0(3)
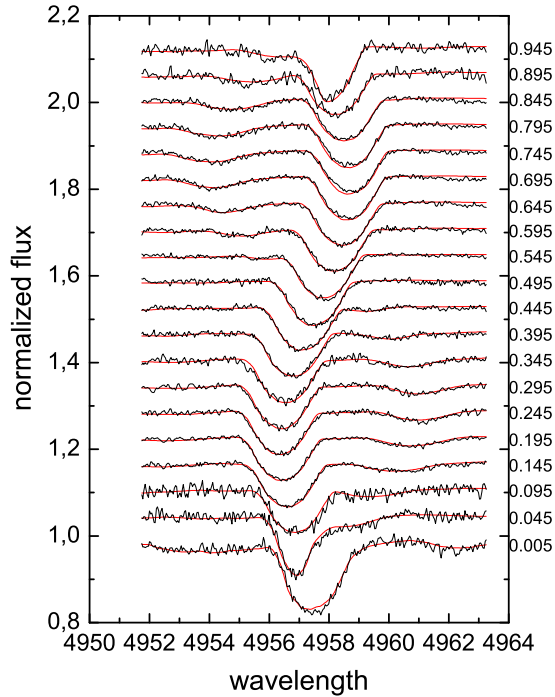
Figure 4.5: Comparison between the observed (black) and the calculated (red) Fe I 4957 Å line profiles. The orbital phase is marked to the right. Primary minimum occurs at phase 0.0.

To each of the solutions shown in Figure 4.4 belongs a set of optimized stellar and system parameters calculated with Shellspec07_inverse. Table 4.3 lists the parameters obtained from the final solution, assuming the two-hemispheres model. The errors of measurement are given in parentheses, in units of the last digit. The radius of the secondary is derived from the orbital period obtained from the KOREL analysis and the $v \sin i$ and represents some mean value of the radius of the non-spherical secondary. All the obtained values are compared in Section 4.4 with previously obtained values from the literature. Figure 4.5 shows, for a certain number of selected phase bins, a comparison between the observed and calculated line profiles based on the final solution (the line profiles are shifted by a constant value for a better visualization).

4.3.2   Application to the spectra from 2001

We applied the derived model to the spectra taken in 2001, first without changing any of the parameter values. Figure 4.4 i shows the resulting O-C distribution. We see that the line profile of the primary observed in 2001 is weaker than in 2006, there is a strong attenuation

along the full orbit.

We tried to model this attenuation by adding optical thin circumprimary matter of disk-like structure and constant temperature and density to the model. The density of this disk of $3.0{\times}10^{-9}$ g cm^{-3} and the disk temperature of 1050 K were taken from an unpublished 3D-hydrodynamic simulation of the mass-transfer in the RZ Cas system (Mkrtichian et al. 2010), computed with a program written by Nazarenko (Nazarenko et al. 2001). The radial extension and thickness of the disk were adjusted manually. Finally, we assumed a disk with a thickness of 3 R$_\odot$ (comparable to the diameter of the primary) and a radial extension from 1.6 R$_\odot$ (close to the surface of the primary) to 3 R$_\odot$. This model allows us to adjust the mean line strength of the primary for all orbital phases and gives a much better solution of lower χ^2, although many structures remain, as can be seen from Figure 4.4 ii. Most obvious is the difference in line strength of the primary between the two half-orbits around first and second quadrature. Finally, Figure 4.4 iii shows the solution obtained by assuming two different values of the density of the circumprimary disk of $6.5{\times}10^{-9}$ g cm^{-3} for the "bright" line profiles of the primary and $3.0{\times}10^{-9}$ g cm^{-3} for the "dark" part. The large-scale differences in line strength have been reduced in this way.

4.4 Discussion

By combining several methods based on the KOREL, SynthV, and Shellspec07_inverse programs, we have reinvestigated the RZ Cas system based on time series of spectroscopic observations taken in 2001 and 2006. The new spectroscopic orbits obtained with KOREL are based on a different method than those applied in Lehmann & Mkrtichian (2004) and Lehmann & Mkrtichian (2008a). It combines the measurement of the RVs of both components with the use of a wider spectral range, considering all orbital phases. And KOREL allows to compute the timely variation of line strengths and weights the data accordingly. Our new solution does not reach the formal accuracy of the orbital elements derived from the cross-correlation of the lines of the primary with a template as it was done by (Lehmann & Mkrtichian 2004). On the other hand, the full information from the composite lines formed in all orbital phases is used. The analysis includes for the first time the secondary based on the spectra from 2006, and allows for a comparison of the orbital elements derived from the data from 2001 and 2006.

Based on the observed phase shift between the two epochs of observation, we can determine the difference in orbital period very precisely to $(2.0{\pm}0.1)$ seconds. In Lehmann & Mkrtichian (2008a), the authors also discussed a decrease in the RV semi-amplitudes by 0.6 km s^{-1} between the years 2001 and 2006. They showed that a decrease by such an amount cannot be explained by mass transfer effects and suggested that the decrease is feigned by distortions in the RVs measured in the active phase of RZ Cas in 2001. We have confirmed this assumption. The results of the KOREL analysis show that there is no significant difference between the K-values obtained from the solutions for the spectra from 2001 and 2006.

We investigate two possible scenarios to explain the observed period change. The first is based on the mass transfer occuring between the two epochs of observations in 2001 and 2006, the second on the transfer of angular momentum that was stored during the rapid mass transfer episode in the outer layers of RZ Cas and brought back into the orbit afterward (B-H

model by Biermann & Hall (1973)). In the following estimations we will use the equations taken from Biermann & Hall (1973), these equations can also be derived from a paper by Kruszewski (1966). The first effect, the change of the orbital angular momentum by the mass transfer, results in an increase $\mathrm{d}P$ of the orbital period P by

$$\frac{\mathrm{d}P}{P} = 3 \left(\frac{M}{M_2} - \frac{M}{M_1} \right) \frac{\mathrm{d}M_1}{M}, \qquad (4.5)$$

where $\mathrm{d}M_1$ is the mass transferred to the primary and M is the total mass of both components. Inserting the values for RZ Cas taken from Table 4.3, we obtain $\mathrm{d}M_1 = 6.8 \cdot 10^{-6}$ $\mathrm{M}_\odot$. This is a lower limit of the mass transfer rate assuming conservative mass transfer, i.e. that all the mass transferred from the secondary will reach the primary and no mass outflow from the system occurs. If we assume that we observed RZ Cas in 2001 shortly after a phase of rapid mass transfer and that it was in a quit state until 2006, the mass transfer rate of about $1.4 \cdot 10^{-6}$ $\mathrm{M}_\odot\,\mathrm{y}^{-1}$ derived in this way seems to be too high to explain the observed increase in the orbital period. The second scenario is based on the B-H model and assumes that during the phase of rapid mass transfer shortly before 2001 a large amount of angular momentum, transported by the mass flow, was stored in the outer layers of the primary, speeding up their rotation so that the outer layers rotated supersynchronously with respect to the orbital angular velocity. The angular momentum J_L that is stored in these outer layers, compared to the total angular momentum J of the system is

$$\frac{J_L}{J} = \frac{M_L\,M}{M_1 M_2} \left(\frac{R_L}{a} \right)^2 \frac{\omega_L}{\omega}, \qquad (4.6)$$

where M_L is the mass of the faster rotating surface layers at a radius R_L, a is the separation of the components, and ω_L/ω is the synchronisation factor in angular velocity. When the system goes back to the quiet state, a part $\mathrm{d}J$ of the angular momentum is transferred back from the rotation of the primary to the orbit and the orbital period increases by

$$\frac{\mathrm{d}P}{P} = 3 \frac{\mathrm{d}J}{J} \qquad (4.7)$$

Narusawa et al. (1994) derived an orbital period of RZ Cas of 1.1952572(6) d, based on the observations by Nakamura et al. (1991) in 1990. This value precisely agrees with the value that we obtained from the observations in 2006. So we assume that RZ Cas showed in 1990, before the phase of mass rapid transfer occured, the same orbital period as after this phase in 2006, whereas in 2001 the period was by 2 seconds shorter. If our scenario as sketched above is valid, it means that the total amount of angular momentum that was transferred during the rapid mass transfer episode to the primary was put back into the orbit afterward. Then we can use Equations 4.6 and 4.7 and set $J_L = \mathrm{d}J$ to derive

$$M_L = \frac{1}{3} \frac{M_1 M_2}{M} \left(\frac{a}{R_L} \right)^2 \frac{\omega}{\omega_L} \frac{\mathrm{d}P}{P} \qquad (4.8)$$

For an estimation of M_L by order, we set R_L to the radius of the primary and $\omega_L/\omega = 1$ and obtain for the mass that was involved in the accelerated outer layers of the primary $M_L \approx 6 \cdot 10^{-5}$ $\mathrm{M}_\odot$. This value is about 3 times higher than obtained by Biermann & Hall

(1973) from a similar investigation of the Algol-type star U Cep. Both results are of the same order and, with regard to the different objects and the applied approximations, in a good agreement.

The analysis of the decomposed spectra of the components of RZ Cas using the SynthV program resulted in an almost perfect fit of the observed spectrum of the primary by the computed synthetic spectrum, whereas the spectrum of the secondary could be modeled with less accuracy. Reasons for this are the lower S/N and the less clearly defined continuum of the fainter, late-type star, and the fact that the SynthV analysis assumes a spherical star. We did not find any strong metal underabundance of iron peak elements or λ Boo signatures of the primary component as reported by Narusawa et al. (2006), who found Cr, Ti, Mg and Fe underabundances of -0.95, -0.45, -0.55 and -0.63 dex, respectively. Both Cr and Ti have solar abundance within the errors of measurement. The abundances of Mg (+0.14 dex) and Fe (-0.16 dex) can also be considered to be close to solar values. The only remarkable deficiency of -0.39 dex was found for Si (-0.59 dex by Narusawa). We conclude that the primary component of RZ Cas is a normal A-type star of close to solar abundance.

The application of Shellspec07_inverse to derive stellar and system parameters of RZ Cas from a non-linear optimization using time series of line profiles was successful in the case of the relatively undistorted spectra obtained in the quiet phase of RZ Cas in 2006. In the following, we compare the results obtained from different methods. The spectra decomposed with KOREL represent the mean spectra of the components from all out-of-eclipse phases. Its analysis using SynthV is based on the assumption of spherical configurations of both stars. Shellspec07_inverse includes the composite spectra from all orbital phases and considers Roche geometry and gravity darkening of the secondary. And it is able to derive the orbital inclination and the radius of the primary directly from the observed spectra. Since it considers synchronized rotation and a Roche-lobe filling secondary, it will not give values for the radius of the secondary or its $v \sin i$, however. These values are implicitly given, depending on the derived mass ratio, orbital separation, and inclination. The effective temperatures of the two stars were derived by Shellspec07_inverse from the analysis of only four Fe I lines. In a narrow sense, they represent only mean line strength scaling factors for these special lines. Effective temperatures of the same physical meaning as derived from the decomposed spectra can be obtained with Shellspec07_inverse only if we investigate a wider spectral region. This much more computer time consuming application can be explored in the future by using, for instance, the least-squares deconvolution (LSD, Donati et al. (1997)) technique to compute mean line profiles from a wide spectral range.

The following comparison of system parameters is based on Table 4.4. It lists the values derived from the spectra taken in 2006 and compares them with the results from literature. Values that were assumed by the authors but not derived are in brackets. Errors in units of the last digit are given in parentheses. Our value of T_{eff} for the primary of 8 907 K is only slightly higher than those derived from the analysis of the disentangled spectrum but more than 300 K higher than the value of 8 600 K derived by both Maxted et al. (1994) and Rodriguez et al. (2004b), and also higher than the 8 720 K found by Varricatt et al. (1998). Based on both the Shellspec07_inverse results and on the analysis of the decomposed spectrum, we can exclude these lower temperatures. The spectral type that we derive for the primary using the tables by de Jager & Nieuwenhuijzen (1987) is A2 V. For the secondary, we

Table 4.4: Parameters of the RZ Cas system from literature and obtained with Shellspec07_inverse.

ref	T_1 (K)	T_2 (K)	$\log g_1$	$\log g_2$	R_1 ($R_\odot$)	R_2 ($R_\odot$)	M_1 ($M_\odot$)	M_2 ($M_\odot$)	q	a ($R_\odot$)	i (deg)
A)	8600(100)	4700(200)	4.34(2)	3.73(2)	1.67(3)	1.94(3)	2.21(8)	0.73(2)	0.331(8)	6.77(1)	83.01(1)
B)	[8720]	4257(26)	4.33(2)	3.72(1)	1.69(6)	1.95(6)	2.2(3)	0.73(7)	[0.331]	6.8(3)	83.20(3)
C)	8600	4370(60)	4.33(3)	3.72(3)	1.67(2)	1.95(3)	2.18(7)	0.72(2)	[0.331]	6.76(9)	83.1(2)
D)	[8600]	4480(13)	4.38(2)	3.73(3)	1.62(2)	1.99(3)	2.28(9)	0.77(3)	0.338(2)	6.87(8)	81.98(5)
E)	8907(15)	4797(20)	[4.35]	[3.7]	1.61(1)	1.93	2.01(2)	0.69(1)	0.342(2)	6.59(3)	82.0(3)

The sources are A) Maxted et al. (1994), B) Varricatt et al. (1998), C) Rodriguez et al. (2004b), D) Soydugan et al. (2006), and E) the present work

obtain T_{eff}=4 800 K. This value is significantly higher than in all previous findings, except for the temperature given by Maxted et al. (1994), and would correspond to spectral type G8. We note, however, that the temperature derived with Shellspec07_inverse represents the effective temperature of the non-spherical secondary at the pole. The temperature in most parts of its surface will be lower due to the gravity darkening (see the discussion below). Moreover, the observed effective temperature in terms of some average value across the surface will change with orbital phase, as we see from the changing line depths of the secondary around secondary minimum in Figure 4.4, and so will do the "spectral type".

The RV semi-amplitudes derived from RVs measured from the line centroids are based on a model that does not include any non-sphericity effects or effects that occur during the eclipses (Rossiter effect). KOREL derives the orbital solution from RVs weighted by the derived line strengths and suppresses in this way the influence of the Rossiter effect on the orbital solution, but does not consider non-sphericity effects. Shellspec07_inverse derives the RV semi-amplitudes by considering the effects of non-sphericity on the line shapes as well as the line asymmetries during the eclipses (eclipse mapping). Thus, it should provide the most reliable mass ratio of the stars that we determined to 0.342±0.002. This value is clearly higher than the values between 0.331 and 0.338 determined by previous authors. The derived mass of the secondary agrees within the errors of measurement with the values derived by other authors, except for Soydugan et al. (2006). Thus, the higher value of the mass ratio is caused by the lower value of the mass of the primary of (2.01±0.02) $M_\odot$ that we obtained, and the smaller separation of (6.59±0.03) $R_\odot$. The derived radius of the primary of (1.61±0.01) $R_\odot$ and the orbital inclination of (82.0±0.3)° agree well with the values derived by Soydugan et al. (2006).

Comparing the rotational period of the primary of (1.190±0.013) d derived from the radius and $v \sin i$ with the orbital period, we find, within the errors of measurement, that the primary rotates synchronously.

If we assume that the surface intensity distribution of the secondary is only influenced by limb and gravity darkening, the most accurate solution is found by applying a gravity darkening exponent of 0.5 to the hemisphere of the secondary pointing towards the primary, and the usual value of 0.08 to the opposite hemisphere. We are aware, of course, that we derived such an exotic value of β=0.5 because we tried to model some inhomogeneous surface intensity distribution that may arise e.g., from the presence of spots by applying a law that describes a completely different physical effect. This assumption is supported

by previous photometric results. Kitamura & Nakamura (1987) found, from a quantitative analysis of the observed ellipticity effect in nine semi-detached binary systems, that the gravity darkening coefficient α deduced for the secondaries is significantly larger than unity (or, with our definition of the gravity darkening exponent $\beta=\alpha/4$, that $\beta > 0.25$). For RZ Cas, they obtained the unusually large value of the gravity darkening exponent of 0.56 ± 0.04. Authors wrote that such large values "could not be reconciled by any adjustment of the physical elements used as the input parameters within the extent of reduction errors". Unno et al. (1994) explain the anomalous high correlation of the surface brightness to the surface gravity on the secondaries of semi-detached systems by the enthalpy transport associated with the mass outflow from the secondary. Their calculations show that in the consequence of the mass outflow via the Lagrangian point L_1 dark spots are formed at low gravity regions on the front and back sides of the secondary toward the primary. Our improved modeling of the observations provided by the high value of β partly confirms this assumption and suggests the presence of a large dark spot that dominates the surface region pointing toward the primary and that may have a smooth transition to the other parts of the surface. If the reflection effect is taken into account, we expect to measure an even higher value of the gravity darkening exponent since this effect would brighten in particular the surface covered by the dark spot. However, we found no evidence of such a cool dark spot on the back side of the secondary, in agreement with the results by Varricatt et al. (1998) obtained from an analysis of the J and K band infrared light curves.

The application of the model derived from the spectra taken in 2006 to those from 2001 shows a strong attenuation of the line of the primary, inferring that there is dense circum-primary matter and that a transient phase of rapid mass-transfer occurred shortly before the observing period in 2001 as already suggested by Lehmann & Mkrtichian (2008a). The attempt to model this attenuation by introducing optically thin circumprimary matter of disk-like structure in Shellspec07_inverse provided a significantly improved solution of lower χ^2. The χ^2 decreases even more if we assume different densities of the disk in two different regions of the orbit. Our results confirm the suggestion by Lehmann & Mkrtichian (2008a) that RZ Cas has undergone a transient phase of rapid mass-transfer and that an accretion annulus around the primary was formed at this epoch. The small-scale, regional structures of high contrast that remain in the residuals (Figure 4.4 iii) point to complex hydrodynamic structures of the circumprimary matter during the stage of rapid mass transfer that cannot be modeled with Shellspec07_inverse without additional input from hydrodynamic simulations.

The results presented in this chapter have been published in Tkachenko et al. (2009).

Chapter 5

Spectral analysis of TW Dra

We investigate the time series of high-resolution spectra of TW Dra taken in 2007 and 2008 using all of the methods that we applied to RZ Cas. The analysis was complicated due to the presence of a third star in the TW Dra system, however, leading to a necessary adaption of some of the methods.

5.1   Light from the third component

TW Dra is the bright component of the visual binary ADS 9706. It consists of the unresolved Algol-type system (components A and B) and a third component in a distance of 3 arcsec. The observed spectra of TW Dra include an unpredictable amount of light from the third component, in dependence on the slit orientation of the spectrograph (the field of view of the Coude spectrograph rotates with the hour angle) and on the seeing conditions during the observations (the typical seeing was 2 arcsec). Figure 5.1 (left) shows the time series of line profiles obtained in 2007 folded with the orbital period. The horizontal axis spans ± 300 km s^{-1}, the vertical axis gives the orbital phase from -0.25 (bottom) to +0.75 (top). Line profiles were built by co-adding the 9 most unblended stronger metal lines, which are Fe I 4958 (narrow doublet), 5456 (narrow doublet), 5616, 5625, 6065, and 6192 Å, Ca I 6122 Å, and Si II 6371, 6347 Å and by averaging the resulting mean line profiles into 50 equidistant orbital phase bins. From Figure 5.1 we clearly see the varying contribution of the third component in form of the straight and sharp vertical lines that show no visible RV variation with the orbital phase. The Rossiter-McLaughlin effect can be seen as the S-shaped dark feature during primary eclipse (phase zero), and less pronounced during secondary eclipse. The horizontal gray lines are due to the incomplete phase coverage.

The unpredictable contribution of the third component causes serious complications in the line profile analysis. Figure 5.1 (right) shows one of the profiles. Here, the contribution of the third component can be seen as the distortion in the blue wing of the deep line of the primary. A fit by three Gaussians, e.g., gives only a rough approximation and works only at orbital phases of largest RV-separation.
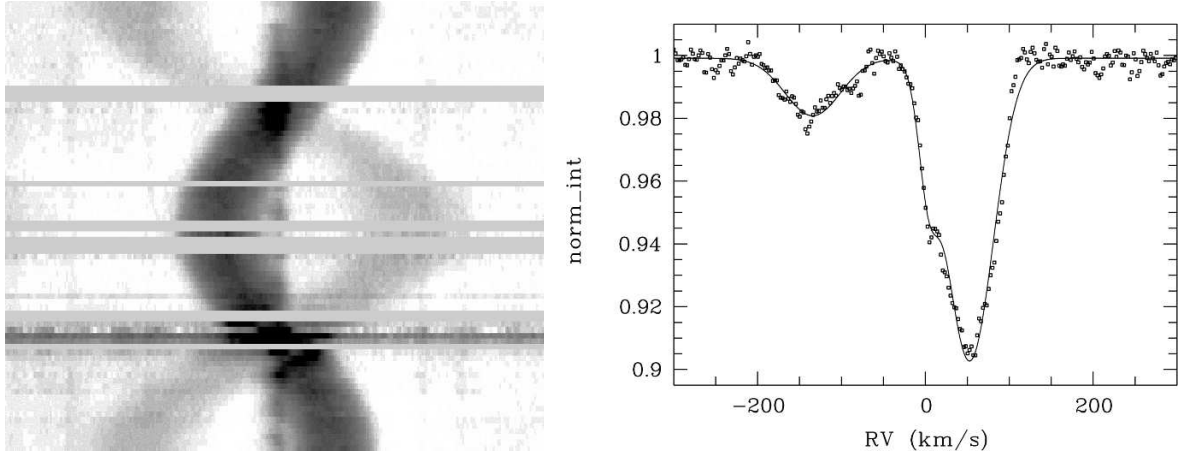
Figure 5.1: **Left:** Time-series of co-added line profiles folded with the orbital period. The horizontal axis spans ± 300 km s^{-1}, the vertical axis gives the orbital phase from -0.25 (bottom) to +0.75 (top). **Right:** Fit of one composite line profile by three Gaussians (example)

5.2   Determination of basic parameters using KOREL

The KOREL program (Hadrava 2004a) provides a unique possibility to disentangle the unpredictable contributions of the third component from the observed composite spectra by calculating the timely varying line strengths in the third component's spectra. We used KOREL to obtain the orbital solution and the extracted spectra of the three components by using a model that includes the two components of the Algol-type system in its close orbit and the third component in a wide orbit of practically infinite orbital period. The analysis is based on the wavelength range 4895-5670 Å that is almost free of telluric lines. The separate KOREL solutions for the years 2007 and 2008 showed that the obtained periods and epochs of minimum light do not differ significantly from each other. Assuming that the values derived from the times of minima will be more precise than those attainable from the time sampling of our spectra, we fixed the epoch of Min I and the orbital period to the values computed from Zejda's ephemeris (Zejda et al. 2008) for the middle of all our observations, obtaining $MinI = 2\,454\,400.97997$, $P = 2.8068491$ d.

Table 5.1: Orbital elements of TW Dra derived with KOREL.

element		primary	secondary	third
P	(d)	2.8068491 (fixed)		
T		2 454 400.97997 (fixed)		
K_1	(km s^{-1})	64.05(34)	150(2.3)	
γ	(km s^{-1})	0.68(71)	0.7(1.1)	1.93(41)
q		0.427(11)		
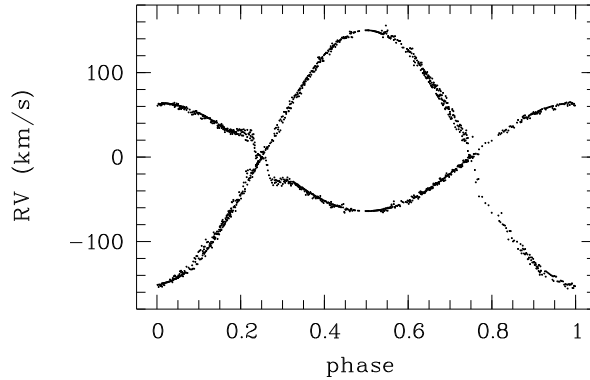
Figure 5.2: RVs of the primary and the secondary of TW Dra obtained with KOREL, folded with the orbital period.
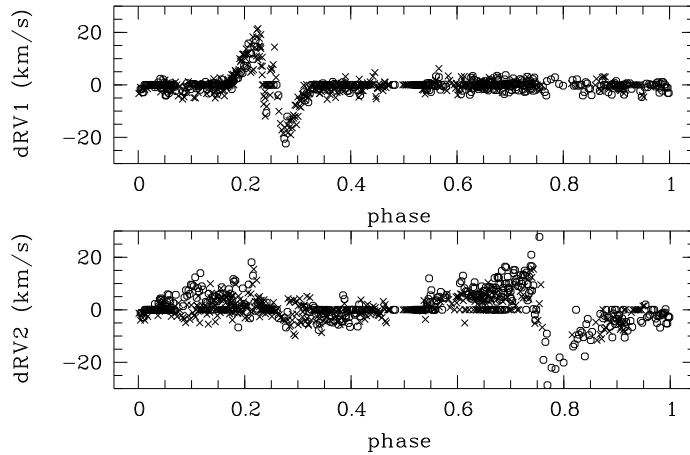

Figure 5.3: As Figure 5.2 but for the deviation of KOREL-RVs from the calculated orbital solutions, shown for the primary (top) and the secondary (bottom), for the data from 2007 (circles) and from 2008 (crosses).

5.2.1   Orbital solution

The orbital elements derived with KOREL from the combined data set including the spectra from 2007 and 2008 are listed in Table 5.1 where T gives the time of Min I. Errors in units of the last digits are given in parentheses. The computed RVs are shown in Figure 5.2. For a better visualization, phase zero corresponds in Figures 5.2 to 5.4 to the orbital phase of largest RV-separation. Figure 5.3 shows the deviations of the obtained RVs from the calculated orbital solution. Note that this deviation is identical to zero for the majority of data points which means that in most cases KOREL shifted the corresponding spectra by exactly the value of the calculated orbital RV to build the decomposed spectra of the components. For this reason it is not possible to use the RVs computed by KOREL for an error estimation of the calculated elements. The errors of K_1 and q as listed in Table 5.1 have been estimated from the χ^2-distribution obtained from running KOREL with fixed input parameters on a two dimensional grid in K_1 and q. Absolute values of the γ-velocity have
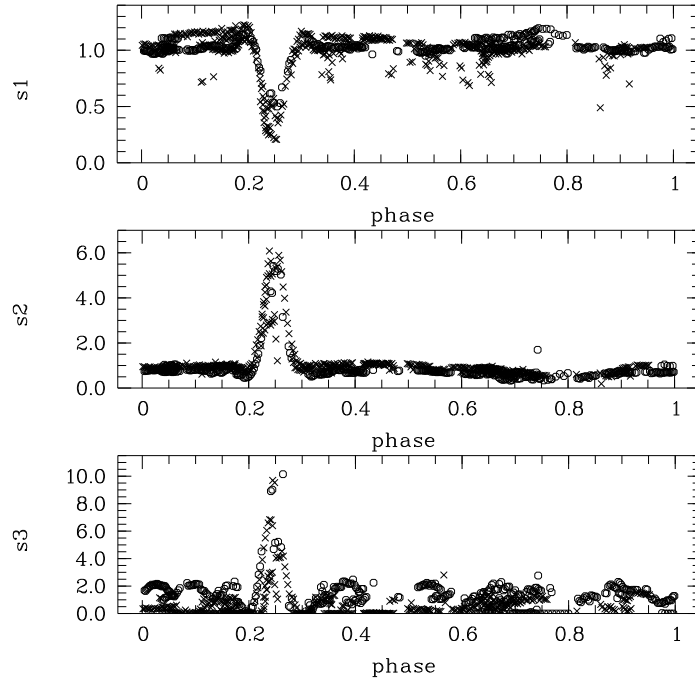
Figure 5.4: As Figure 5.2 but for the calculated line strengths, from top to bottom for the primary, secondary, and third component.

been measured from the decomposed spectra by comparing the positions of a large number of metal lines with the corresponding laboratory wavelengths.

From Figure 5.3 it can be seen that there is no systematic difference between the data from 2007 and 2008. We see a pronounced Rossiter effect in the RVs of both stars during the corresponding eclipses.

Zejda et al. (2010) derived photometric solutions using the two programs FOTEL (Hadrava 2004b) and PHOEBE (Prša & Zwitter 2005) and obtained the orbital inclinations of $86.°74 \pm 0.°03$ and $87.°10 \pm 0.°08$, respectively. Using the weighted mean of $i = 86.°8 \pm 0.°3$ and inserting the derived elements into

$$
\begin{aligned}
M_1 &= \frac{P K_1^3 (1+q)^2}{q^3 \sin^3 i} \cdot 1.035793 \cdot 10^{-7} M_\odot \\
M_2 &= q M_1 \\
a &= \frac{P K_1 (1+q)}{q \sin i} \cdot 0.0197714 R_\odot,
\end{aligned}
\tag{5.1}
$$

we get for the absolute masses and the separation of the TW Dra system $M_1 = (2.01 \pm 0.22)$ M$_\odot$, $M_2 = (0.89 \pm 0.07)$ M$_\odot$, and $a = (12.10 \pm 0.47)$ R$_\odot$.

Figure 5.4 shows the variation of the line strengths with orbital phase computed with KOREL. The line strengths of the primary have a minimum during primary eclipse and a maximum during secondary eclipse. As expected, the line strengths of the secondary behave in the opposite way. The bottom panel of Figure 5.4 shows the more or less random variation of the line strength of the third component, in dependence on nightly seeing conditions and orientation of the entrance slit of the spectrograph. Only during primary eclipse where the

light of the primary is dimmed by more then two magnitudes a pronounced maximum can be seen. From the line strengths of the primary and secondary of TW Dra we see no systematic differences between the years 2007 and 2008 but variations on a short-term scale between different orbital revolutions. We cannot directly decide, however, if the short-term variations are intrinsic or feigned by the varying influence of the third component.

5.2.2   Normalization of the decomposed spectra

Whereas the orbital elements have been determined using the full data set, it was not possible to separate the spectra of the three components in this way. The reason is that, due to the inconvenient time sampling, we always observed a strong ripple (wavelike structure) in the continua of the decomposed spectra. Only by restricting the calculation to the data obtained in 2007, the resulting extracted spectra showed sufficiently straight and smooth continua.

Since the individual continua of the KOREL-extracted spectra are a priori unknown, we have to renormalize the spectra. Let r_i be the KOREL output spectra and R_i the spectra normalized to the individual continua, and $l_i = 1 - r_i$, $L_i = 1 - R_i$ the corresponding line depths. The decomposed spectra are normalized to the common continuum C of all three stars, it is

$$l_i = \alpha_i L_i, \quad \sum \alpha_i = 1, \quad i = 1...3, \tag{5.2}$$

where $\alpha_i = C_i/C$ is the ratio between the continuum flux of component i and the total continuum $C = \sum C_i$.

We want to compute the intensities R_i that are normalized to the individual continua C_i. This nontrivial task that is usually solved by assuming some flux ratio values between the components approximated from photometry is complicated here by the fact that the third component's light contributes in a more or less random way to the spectra. We could solve the problem by using two advantageous facts. First, we have one spectrum at our disposal that contains only the light from the third component. It was taken during primary eclipse under good seeing conditions by guiding the telescope on the third component. We will call the line intensities of this spectrum R_3^s . And second, the primary eclipse of TW Dra is a total one and the spectra taken during Min I do not contain any light from the primary.

In the following we will assume that the wavelength dependence of the continuum flux ratio along our wavelength region of interest can be neglected. The results will show that this approximation is justified. From the single spectrum of the third component we find

$$\alpha_3 = \langle l_3/L_3^s \rangle \tag{5.3}$$

where the brackets mean the averaged mean. Concerning the uncertainty in the continuum levels in the KOREL and in the measured spectra, a more convenient way to normalize the KOREL spectra is to use a linear regression and σ-clipping according to

$$L_3^s = a + b\,l_3 \tag{5.4}$$

where $b = 1/\alpha_3$ and a corresponds to some continuum shift. From the regression, we obtain α_3=0.0840. Figure 5.5 shows a comparison between the single observed spectrum of the third component and its normalized, extracted KOREL spectrum. The fit is almost perfect.
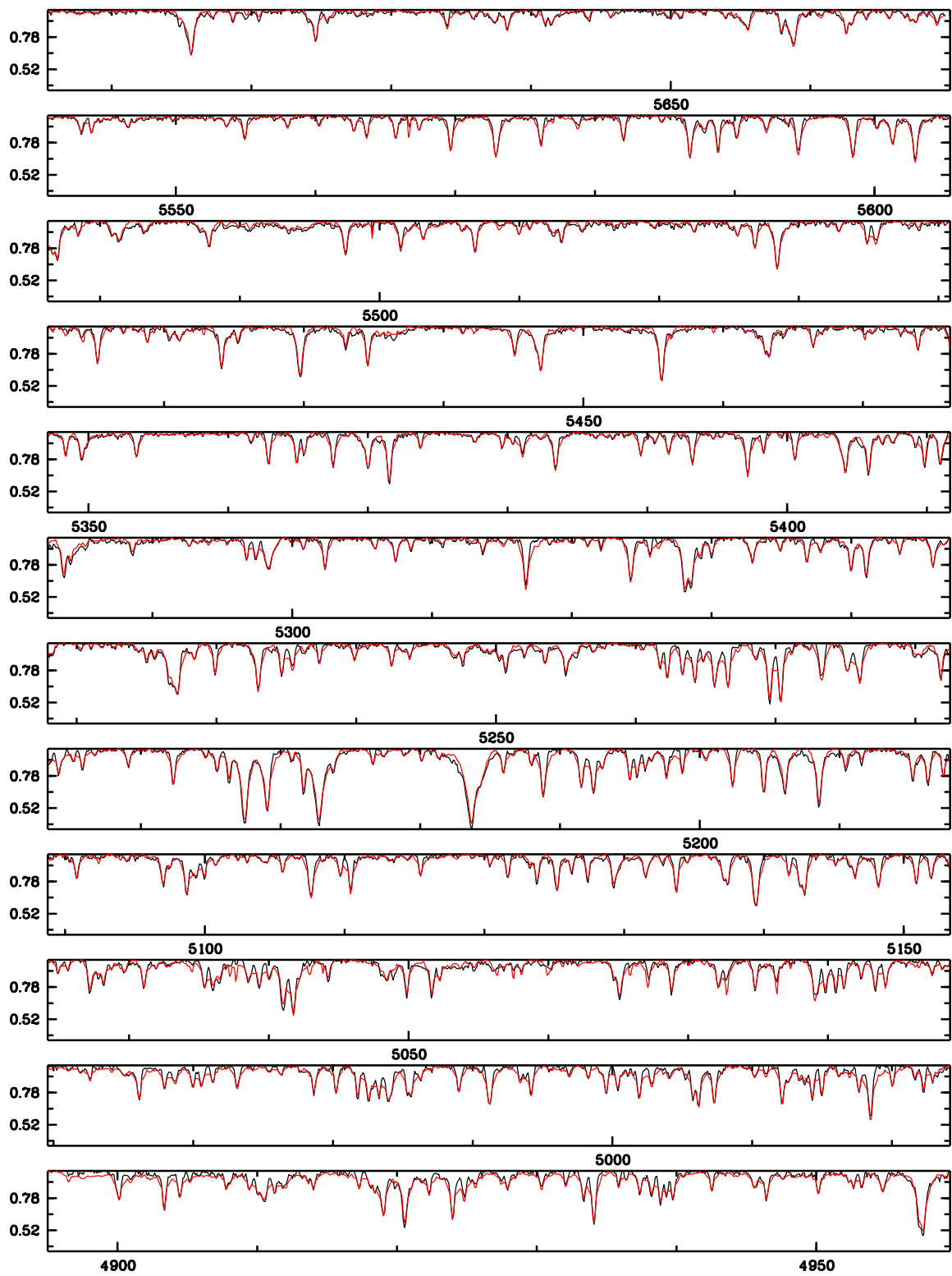
Figure 5.5: Comparison of the single, sharp-lined spectrum of the third component (black) with the renormalized decomposed spectrum (red). The wavelength is given in Å.

Now we know the normalized spectrum of the third component, i.e. R_3 and L_3. Spectra observed during the total primary eclipses do not contain any contribution from the primary and we have

$$r^{MinI} = \frac{R_2\, C_2 + R_3\, C_3^{MinI}}{C_2 + C_3^{MinI}} \tag{5.5}$$

Introducing the ratio $\alpha_3' = C_3^{MinI}/C_2$ of the continuum fluxes between the third component in the spectra during primary minimum (note that this contribution varies in a random way) and the continuum flux of the secondary, we get

$$R_2 = \left(1 + \alpha_3'\right) r^{MinI} - \alpha_3' R_3 \tag{5.6}$$

This can be transformed by using Eq. 5.2 to

$$l^{MinI} = \frac{l_2}{\alpha_2} + \alpha_3'\left(L_3 - l^{MinI}\right) \tag{5.7}$$

We used Eq. 5.7 to obtain the continuum flux ratios α_2 and α_3' by a least squares fit between the spectrum l^{MinI} observed during primary minimum, the KOREL-extracted spectrum of the secondary l_2, and the already renormalized spectrum of the third component L_3 and yield α_2=0.100, α_3'=0.283.

Figure 5.6 compares the spectrum observed during primary minimum (black) and the fit obtained from

$$r^{MinI} = \frac{1 + \alpha_3' R_3 - \left(1 - r_2\right)/\alpha_2}{1 + \alpha_3'} \tag{5.8}$$

(black) that counts for the influence of the third component according to the derived flux ratios. To visualize the influence of the third component during primary eclipse, we additionally computed the spectrum shown in Figure 5.6 in red color by setting R_3 to unity. The influence of the third component on the line profiles can be clearly seen from the difference between the almost perfect fit by the spectrum shown in green and the fit by the spectrum shown in red color. From the goodness of fit we conclude that it is not necessary to account for the wavelength dependence of the flux ratios within the given wavelength interval. The fact that the fit of the spectrum observed during primary minimum as well as those of the single spectrum of the third component is almost perfect proves that KOREL performs the separation of spectra very well and that our approach to the problem of renormalization gives reliable results.

Now we know α_2 and α_3, from which we get α_1=0.816. The continuum flux ratios with regard to the primary follow to C_2/C_1=0.123 and C_3/C_1=0.103. Whereas the first value gives the flux ratio in the observed passband between the secondary and the primary, the second value is the mean ratio during the observations on/off the slit and does not correspond to the real flux ratio between the third component and the primary.

5.3   Spectrum analysis with SynthV

We used the normalized, decomposed spectrum of the primary to determine its atmospheric parameters and elemental abundances. For the calculation of model atmospheres we used the
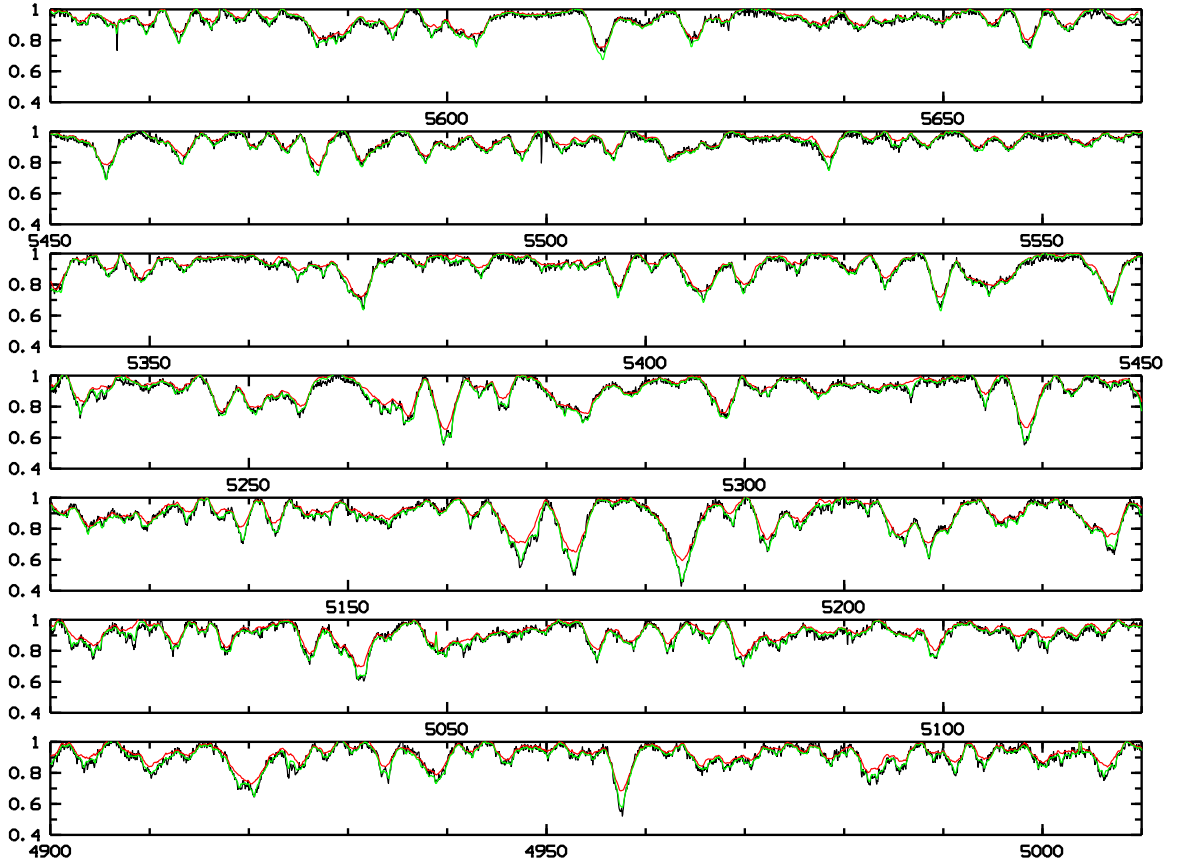
Figure 5.6: Fit of the observed spectrum during Min I (black) by the decomposed spectrum of the secondary (red) and by adding the third component's contribution (green). The wavelength is given in Å.

program LLmodels (Shulyak et al. 2004) (see § 2.3.3) and for the computation of synthetic spectra the SynthV code (Tsymbal 1996) (see § 2.3.2). The parameters were derived in an iterative procedure. We started with the computation of model atmospheres on a grid in T_{eff} (7500 - 8500 K, steps of 100 K) and $\log g$ (3.6 - 4.1, steps of 0.1), based on solar abundances and a micro-turbulent velocity of ξ=2 km s^{-1}. From each model atmosphere we computed synthetic spectra with the SynthV code in the range from 4890 to 5670 Å for different $v \sin i$ and compared them with the observed spectrum applying the χ^2 criterion. In this way we obtained first optimized values of T_{eff} and $\log g$. In the next step we varied the micro-turbulence and the abundances of all chemical elements for which we found a contribution in the observed spectral range, using SynthV to derive the optimum values. These have been given as new input parameters to LLmodels to compute new model atmospheres, again on a grid in T_{eff} and $\log g$.

The described procedure was repeated four times, refining the grid in each step and using $\Delta T_{\mathrm{eff}} = 25$ K, $\Delta \log g = 0.02$ in the last step. No further changes in χ^2 could be detected after the third iteration. In this way we finally obtained the best parameters based on a consistent model atmosphere. Realistic errors of the parameters can only be obtained

Table 5.2: Elemental abundances of the primary of TW Dra. Values in parentheses give the deviation from standard solar abundance.

C	O	Mg	Si
-3.56 (+0.09)	-3.56 (-0.14)	-4.16 (+0.35)	-4.66 (-0.13)
Ca	Sc	Ti	Cr
-5.63 (+0.10)	-8.73 (+0.26)	-7.07 (+0.07)	-6.20 (+0.20)
Fe	Ni	Y	
-4.43 (+0.16)	-5.61 (+0.20)	-9.74 (+0.09)	

by computing synthetic spectra on a multidimensional grid of all parameters including the elemental abundances. Since we had not the computer power to do this, we computed the error of each single parameter from the χ^2 statistics based on a one-dimensional grid centered at minimum χ^2 by fixing all other parameters to their optimum values. The errors obtained in this way are only lower limits.

We obtained T_{eff}=(8150±20) K, $\log g$=3.88±0.02, $v \sin i$=(47.1±0.5) km s^{-1}, and ξ=(2.9±0.3) km s^{-1}. Table 5.2 lists the derived abundances, the error was estimated to ±0.03 dex for Fe and ±0.05 dex for the other elements. The abundances are close to solar ones. Slight overabundances have been found for Mg, Sc, Cr, Fe and Ni with 0.35, 0.26, 0.20, 0.16 and 0.20 dex, respectively, while O (-0.14 dex) and Si (-0.13 dex) are slightly under-abundant. Figure 5.7 shows the best fit of the renormalized, decomposed spectrum of the primary based on the derived abundances and atmospheric parameters. We conclude that the primary of the Algol-type system is a normal A-type star.

5.4   Spectroscopic modeling of TW Dra

We used the Shellspec07_inverse program for the computation of the synthetic, composite spectra of TW Dra at arbitrary orbital phases. The existence of the third, visual component complicates the modeling of the close binary system, as can be strikingly seen from Figure 5.6. To count for the third light, we implemented an additional subroutine into the Shellspec07_inverse program. It solves for the problem by means of a least-squares fit in the sense of

$$(R_{obs} - \alpha_1 R_c - \alpha_2 R_3)^2 \to min \tag{5.9}$$

where R_{obs} is the observed composite spectrum that includes some random amount of light from the third component, R_c is the spectrum computed by Shellspec07_inverse at the corresponding orbital phase, and R_3 is the normalized observed spectrum of the third component. The free parameters α_1 and α_2 represent two physical parameters: the ratio of the continuum flux from the third component in the spectrum to the continuum flux of the Algol-type system $C_3/(C_1 + C_2) = \alpha_2/\alpha_1$, and a correction factor for a possibly inaccurate continuum normalization of the observed spectra $\beta = (\alpha_1 + \alpha_2)^{-1}$.

We used the LLmodels code (Shulyak et al. 2004) for the calculation of atmosphere models for the more massive hot primary component and MARCS models (Gustafsson et al. 2008)
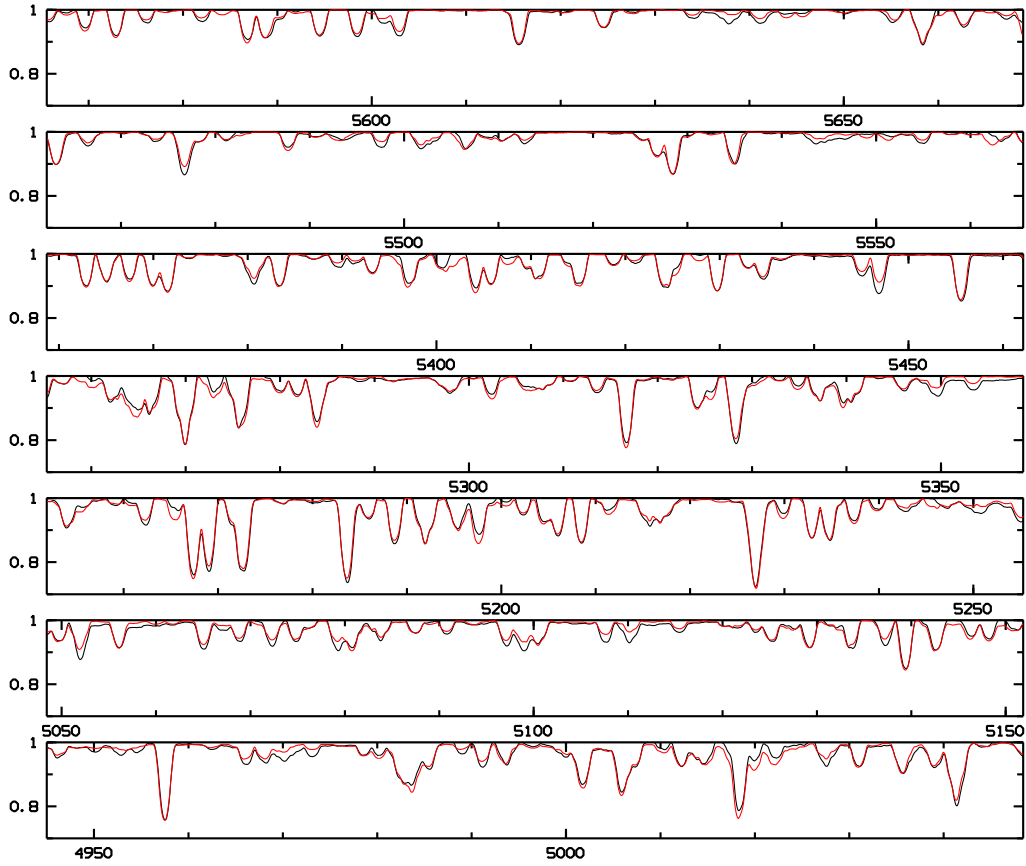
Figure 5.7: Best fit (red) of the decomposed spectrum of the primary (black). The wavelength is given in Å.

for the cool secondary. In the case of the secondary, the molecular line list by Kurucz (Kurucz 1995) was used, additionally to the list of atomic lines taken from the VALD database (Kupka et al. 2000). Intrinsic line profiles have been calculated with the SynthV program (Tsymbal 1996) on a grid of different temperatures and nine different angles θ between the line of sight and the normal of the stellar surface and provided to Shellspec07_inverse.

In the Shellspec07_inverse calculations we used the elemental abundances and $\log g$ of both stars as derived from the analysis of the extracted spectra to determine the following free parameters: effective temperatures $T_{\mathrm{eff}_{1,2}}$ and RV semi-amplitudes $K_{1,2}$ of both components, $v_1 \sin i$ and radius R_1 of the primary, systemic γ-velocity, and orbital inclination i. For the cool secondary we assumed synchronous rotation and Roche-lobe filling geometry; the deviation of the shape of the primary from sphericity was neglected. For the analysis we used mean profiles built from the four Fe I lines at 4958, 5056, 5616, and 5625 Å and averaged them into 100 orbital phase bins calculated with P=2.8068491 d and Min I=2 454 400.97997 as given in Section 5.2.

Figure 5.8 shows in its upper part the observed and synthetic line profiles for the spectra from 2007. Each column corresponds to one orbital phase binned, composite line profile. The vertical dark stripes indicate gaps in the phase coverage. The phase of primary minimum was shifted to 0.25 for better visualization. At this phase, strong distortions of the line of
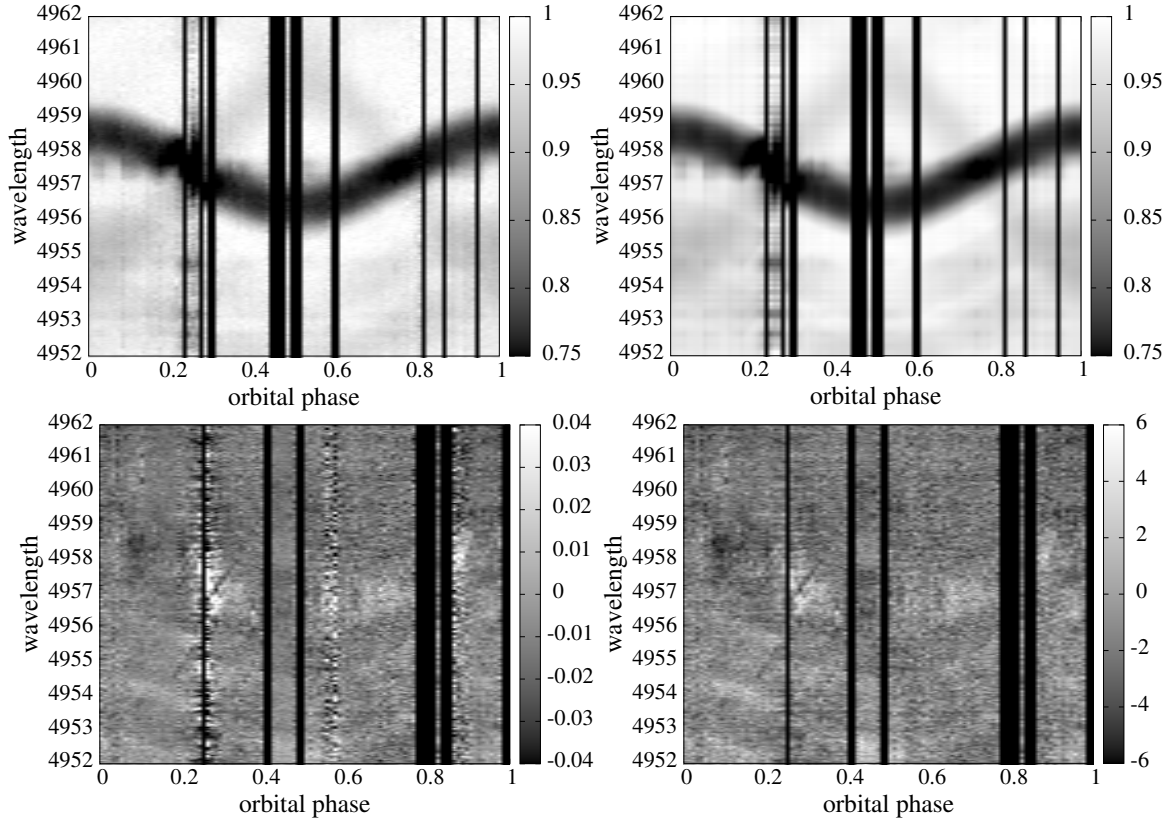
Figure 5.8: **Top:** Fe I 4957 Å line profiles of TW Dra observed in 2007 (left) and calculated with Shellspec07_inverse (right), folded with the orbital period. **Bottom:** O-C line intensity residuals of the fit of the spectra taken in 2008 (left) and the corresponding χ^2-distribution (right).

the primary due to the Rossiter effect can be seen. The lower part compares the O-C line intensity residuals of the fit with the corresponding χ^2-distribution that is independent of the S/N of the data and used, like in the case of RZ Cas, as the measure of the goodness of fit.

The finally derived stellar and system parameters are listed in the last row of Table 5.3 that will be used in the next section for a comparison with previous determinations. Figure 5.9 compares selected calculated line profiles with the observed ones. Each profile is shifted by a constant value for a better visualization, the orbital phases are given to the right. As can be seen from Figures 5.8 and 5.9, our model matches the observations very well and there are no obvious differences between the results obtained from the data from 2007 and from 2008. The resulting mean value of χ^2 is 1.47 for the spectra from 2007 and 1.77 for those from 2008. Only during primary eclipse a small bright region can be seen in the O-C distributions, the computed line strengths are stronger than the observed ones in this case. Figure 5.10 allows for a closer look at this problem. It shows, for a single profile observed during primary eclipse, that the line core of the computed fit is clearly too strong compared to the observed one, whereas all other parts of the line are well fitted. When we compare the observed spectrum with the spectrum computed by Shellspec07_inverse without including the third component, we see a large offset in the continua. This offset comes mainly from the fact that TW Dra is by 2 mag fainter during the total eclipse so that the light contributions
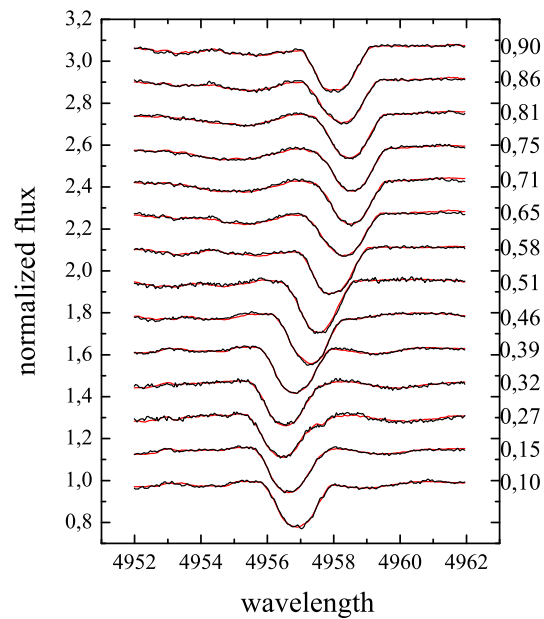
Figure 5.9: Comparison of observed (black) and calculated (red) composite line profiles of TW Dra. The orbital phase is indicated to the right. Primary minimum occurs at phase 0.0.
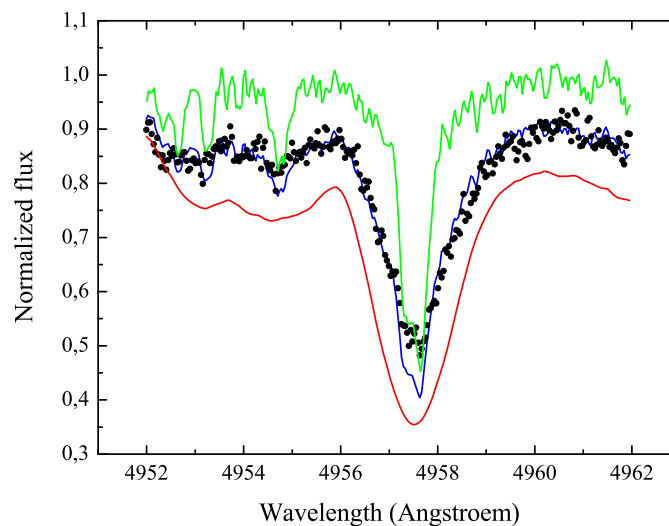

Figure 5.10: Line profiles of TW Dra observed during primary eclipse (black dots) and calculated with Shellspec07_inverse including all three components (blue) and without the third component (red), and the observed profile of the third component (green).

Table 5.3: Compilation of parameters of the RZ Cas system from literature and the values obtained with Shellspec07_inverse (see text for a detailed explanation).

ref	T_1 (K)	T_2 (K)	$\log g_1$	$\log g_2$	R_1 ($R_\odot$)	M_1 ($M_\odot$)	M_2 ($M_\odot$)	q	a ($R_\odot$)	i (deg)
A)					2.4	1.9	0.82	0.43	12.0	
B)						1.7	0.80	0.47		
C)	8060	4450			2.4			0.47		86.1(2)
D)					2.5				12.0	
E)	8180	4407	3.96	3.23	2.53(3)	2.11(5)	0.85(2)	0.403(2)	12.0124(3)	87.13(3)
F)	8160(15)	4538(11)	3.88	3.25	2.58(2)	2.2(1)	0.90(5)	0.411(4)	12.2(2)	86.8(3)

The sources are A) Kopal & Shapley 1956, B) Popper 1978, C) Giuricin et al. 1980, D) Al-Naimiy & Al-Sikab 1984, E) Zejda et al. 2010, and F) this work.

from the secondary and the third component become of the same order, and possibly from an inaccurate normalization of the observed late-type spectrum at this phase. Normally, both problems should have been solved by including the observed spectrum of the third component into the calculations by means of the least-squares fit described before. Since the structure of the overestimated part of the computed profile resembles the line core of the third component, we assume that our fitting procedure overestimates the light contribution from the third component in this special case, but do not have an explanation why.

5.5   Discussion

We derived the orbital solution by means of the KOREL program based on all spectra of TW Dra taken in 2007 and 2008. It was not possible to separate the spectra of the individual components using the full data set, however, wavelike structures appeared in the computed continua of the extracted spectra in this case. We assume that this behaviour is caused by the time sampling of the spectra that includes a large gap between the two epochs of observations. Only by restricting the calculations to the data from 2007 were we able to obtain the straight and smooth continua shown in Section 5.2.

The almost perfect fit achieved for the observed spectrum of the third (visual) component of TW Dra shows first that the KOREL program delivers reliable results with respect of the separation of the observed, composite spectrum into the individual spectra even in our very special case of three components, where the contribution of one component shows unpredictable changes. And second, that our approach to renormalize the spectra works well.

In the framework of this renormalization we obtained the specific flux ratio between secondary and primary of 0.123, valid for a central wavelength of 5 300 Å. Zejda et al. (2010) derived the wavelength dependent flux ratio between the components from UBVRI photometry using different methods like FOTEL (Hadrava 2004b) and PHOEBE (Prša & Zwitter 2005), with the detached system and the Algol-type option in the second program. In Figure 5.11 we show the flux ratios resulting for the different passbands versus wavelength, together with our spectroscopically derived value. It can be seen that our value fits well into the diagram.
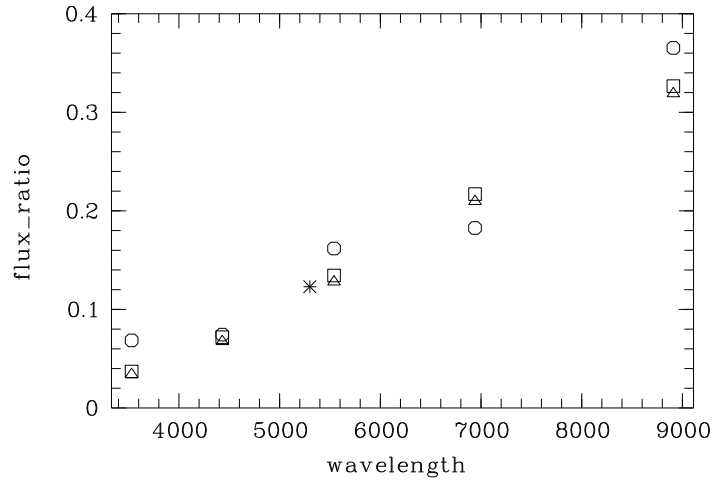
Figure 5.11: Flux ratios between secondary and primary of TW Dra obtained by Zejda et al. (2010) from UBVRI photometry using FOTEL (circles) and PHOEBE (squares for detached systems, triangles for Algol-type systems), and our value (asterisk).

The Shellspec07_inverse program has been used to optimize the stellar and system parameters of the TW Dra system. The existence of the third component in the system strongly complicated the modeling of the close binary, however. Table 5.3 collects all the parameters derived in the present work, together with the values that can be found in the literature. The errors of measurement (if known) are given in units of the last digit in parentheses. The effective temperature of the primary of 8 160 K derived with Shellspec07_inverse is consistent, within the errors of measurement, with that obtained from the analysis of the decomposed spectrum. It is also in good agreement with the value of 8 180 K found by Zejda et al. (2010). Since the SynthV program used to compute the synthetic spectra does not consider the effects of non-sphericity and gravity darkening of the cool secondary, we did not estimate its temperature from its decomposed spectrum but determined it only with Shellspec07_inverse. The resulting T_{eff} of 4 540 K is about 100 K higher than given by Zejda et al. (2010) and Giuricin et al. (1980). The radius of the primary of 2.58 $R_\odot$ is in good agreement with the values of 2.53 $R_\odot$ and 2.50 $R_\odot$ found by Zejda et al. (2010) and Al-Naimiy & Al-Sikab (1984), respectively. For the orbital inclination we derive 86°.8, a value lying in between the values given by Zejda et al. (2010) and Giuricin et al. (1980).

Whereas the scatter in the separation of the components derived by different authors is small, there is a large scatter in the mass ratios. The values of the absolute masses and of the mass ratio determined in the two most recent investigations (Zejda et al. (2010) and this work), on the other hand, agree well within the errors of measurement. The RV semi-amplitudes of K_1=(64.0±0.02) km s^{-1}, K_2=156±1 km s^{-1}, the projected rotational velocity of the primary $v \sin i$=(49.9±0.2) km s^{-1} and the systemic velocity γ=(−0.8±0.1) km s^{-1} derived with Shellspec07_inverse are consistent with those obtained from the KOREL orbital solution and from the analysis of the decomposed spectrum of the primary. From the derived radius of the primary and its $v \sin i$ we obtain a rotation period of P_{rot}=(2.62±0.03) d. Thus, the primary rotates supersynchronous, its rotational angular velocity is by a factor of

(1.07±0.01) faster than the orbital one. For the secondary, we assumed synchronized rotation and a Roche-lobe filling configuration. We determined in the equatorial plane the three radii R_point=5.00 $R_\odot$, R_back=4.02$R_\odot$, and R_side=3.62 $R_\odot$ so that the local $v \sin i$ varies between 65 and 90 km s^{-1}. R_pole is of 3.47 $R_\odot$, and for the effective radius of the secondary that approximates the spherical case we estimate 3.7 $R_\odot$.

We compared the obtained stellar parameters with standard values given by Schmidt-Kaler (1982) and used the tables by de Jager & Nieuwenhuijzen (1987) for the temperature calibration to deduce spectral types and evolutionary states. The derived temperature of the primary corresponds to spectral type A5 for a mean sequence or slightly evolved star. The derived mass is in agreement with this assumption. According to the obtained radius and $\log g$ the primary is slightly evolved. From the mass, radius, and $\log g$ of the secondary we conclude that it is a subgiant, and the derived temperature gives spectral type K1.

The line profile fit shown in Figure 5.9 and the O-C value distributions shown in Figure 5.8 are based on the parameters as listed in the last row of Table 5.3. From both Figures it can be seen that our model matches the observations very well. Only during primary eclipse we observe a discrepancy between the model and the observations (Figure 5.10), as already discussed in the previous paragraph. We checked for two possible explanations of the observed effect: first, the problem could be solved if there would exist some additional light source acting only during primary eclipse. But any hot spot of arbitrary size on the surface of the secondary pointing towards the observer (away from the primary) or other source of such additional light could be seen from a large range in orbital phase around primary minimum. And we can fit the observed profiles perfectly without such an assumption in all orbital phases except for the primary minimum. Second, some of the derived system parameters could be wrong. There are three parameters that influence the line shape in particular during primary minimum: the radius of the primary R_1, the orbital inclination i, and the inclination ϕ of the rotation axis in the tangential plane of the observer (ϕ is measured in a plane perpendicular to those of i). It is possible to reproduce the line profiles observed during primary eclipse by adjusting R_1 or i accordingly. But in both cases we end up with a partial eclipse instead of a total one. And in case of a changed orbital inclination, the fit is worse in the out-of-eclipse phases, due to the fact that it changes the mass of the primary and the separation between the components. The third parameter is also out of question because any deviation of the rotation axis from 90° causes asymmetric line profiles (see Section 1.6). Actually, we cannot give an explanation for the overfitting of the line profiles during the primary eclipse.

There are no obvious differences between the results obtained from the spectra taken in 2007 and in 2008. The resulting mean value of χ^2 is 1.47 for the spectra from 2007 and 1.77 for those from 2008. We assume that TW Dra was in both epochs in a quiet state without showing any signs of rapid mass transfer.

The results presented in this chapter have been published in Tkachenko et al. (2010).

Chapter 6

The spatial filtration effect

One of the reasons that the oEA stars are outstanding objects for asteroseismic investigations (see § 1.4.2) is the occurrence of the *spatial filtration effect* observed during the eclipse of the oscillating primary component. The secondary component acts then as a spatial filter and produces characteristic amplitude and phase changes in the brightness and line profile variations, in dependence on the observed oscillation modes. Unno et al. (1989) were the first who suggested to use the spatial filtration effect for a mode identification in oscillating eclipsing binaries. As described in Chapter 1, this method was photometrically applied to the oEA stars AB Cas (Rodriguez et al. 2004a) and RZ Cas (Gamarova et al. 2003) to identify low-degree modes. An extended work describing the photometric investigation of the screening effect was published by Reed et al. (2005). The first who detected the spatial filtration effect spectroscopically were Lehmann & Mkrtichian (2008a), investigating the RZ Cas system.

Our spectroscopic investigation of the spatial filtration effect is based on numerical simulations. It is included into the thesis to give an outlook on what can be achieved by a future implementation of non-radial pulsations into the Shellspec07_inverse program and by its application to oscillating eclipsing binary stars when the program will run as a parallelized code on a cluster PC. Our actually available computer power does not allow to include the non-radial pulsations with all of their physical implications into the already computing time consuming Shellspec07_inverse program to derive pulsation parameters from the observed time series of spectra. That is why we had to restrict our calculations by using a simple approach and by applying it to integral values obtained from the spectra like the RVs.

6.1 Numerical simulations

Our calculations cover half of the orbit, including the two phases of largest RV separation and the primary eclipse. We compute synthetic line profiles based on the parameters determined for RZ Cas as listed in Table 4.3. In this first, simple approach we consider only the surface velocity field perturbations introduced by the non-radial pulsations and neglect the influence of the temperature and projected surface area perturbations on the line profiles. This is a relatively rough approximation with respect to the temperature, whereas the surface area perturbations are a third order effect, as it is shown by Townsend (1997). With regard to the strong tidal interaction in semi-detached systems, we assume that the pulsation (or rotation) axis of the primary is aligned with the normal to the orbital plane. The light contribution of
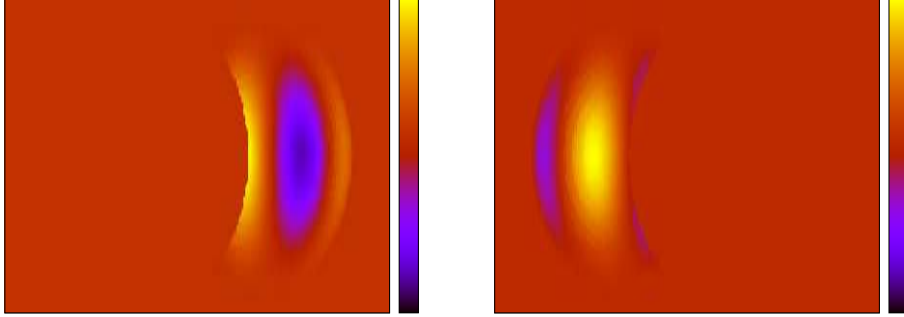
Figure 6.1: The radial velocity field on the surface of the primary for a sectoral $l=4$ mode during primary eclipse, shown for the orbital phases -0.05 (left) and +0.05 (right). Yellow and blue regions indicate positive and negative RVs, respectively.
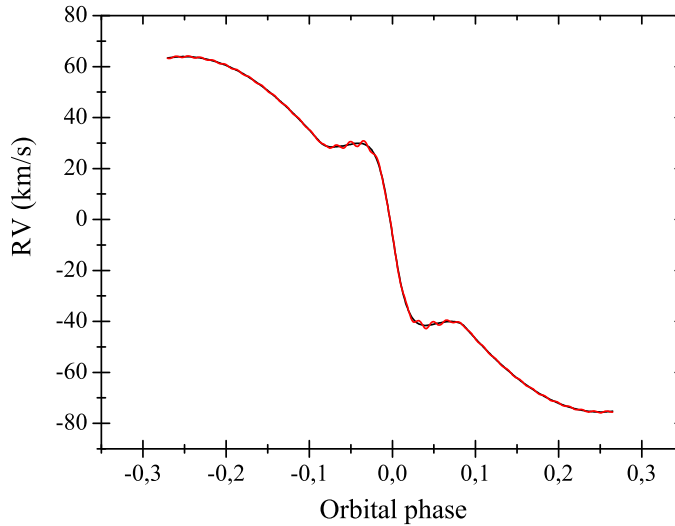

Figure 6.2: The orbital RV curve around primary eclipse showing the Rossiter effect (black) and the same curve additionally perturbed by a sectoral $l=3$ oscillation mode (red).

the secondary is set to zero, which can be done easily because the Shellspec07_inverse program works with pre-computed line and continuum fluxes. In the result, we simulate the influence of the secondary moving in a Keplerian orbit with the oscillating primary and acting during the eclipse phases as a black disk that causes the timely variable obscuration of the primary (Figure 6.1). The orbital period of RZ Cas is roughly 1.2 d, the total duration of the primary eclipse is of about 0.2 d, and the three pulsation modes observed in 2006 spectroscopically (Lehmann & Mkrtichian 2008a) are roughly 57, 62, and 64 c d^{-1}. Thus we observe between 11 and 13 oscillation cycles during one eclipse. To obtain a sufficient resolution, the step width of our calculations was chosen in a way that one pulsation cycle covers 14 steps. All calculations are based on an intrinsic pulsation velocity amplitude of 15 km s^{-1}. The absolute amount of this velocity amplitude will play no role in the interpretation of the results as long it is small compared to the rotation velocity, because at the end we will compare only relative values. After computing the synthetic spectra in the different orbital phases and on a grid of different combinations of (l, m) wavenumbers, we determine the RVs of the primary as the
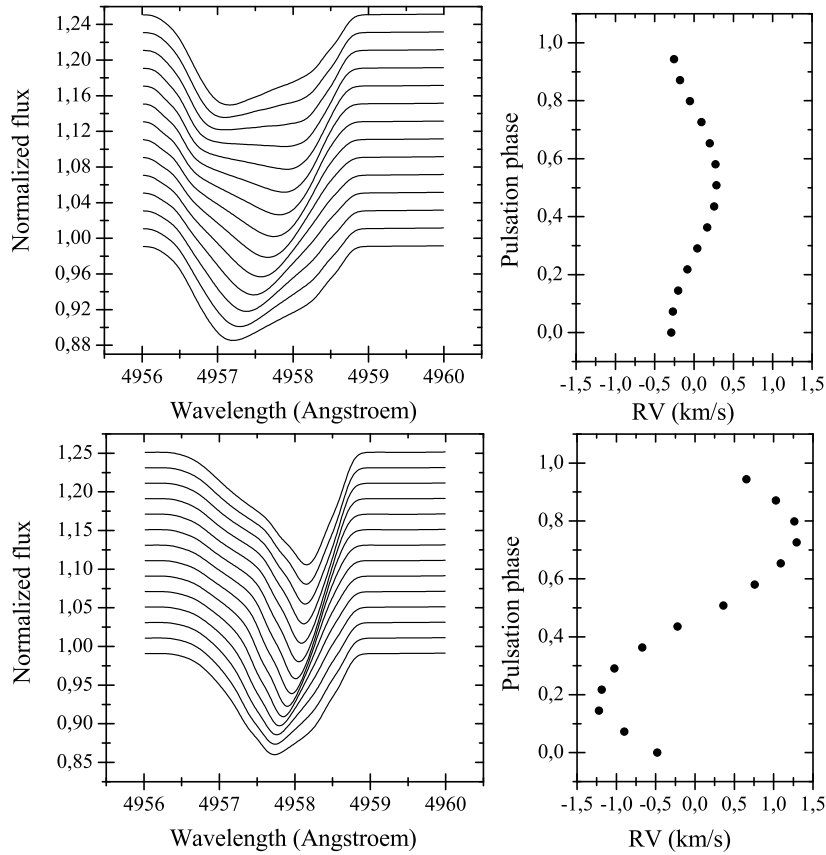
Figure 6.3: Time series of line profiles computed over one pulsation cycle of a sectoral $l=3$ mode (left) and the corresponding RVs measured from these lines (right) at out-of-eclipse phases (top) and at in-eclipse phases (bottom).

center of gravity of the line profiles by calculating its first moments.

Figure 6.2 shows the RVs computed in this way from line profiles that are perturbed (red) and unperturbed (black) by non-radial oscillations, in this case by a sectoral $l=3$ mode. The obtained RVs are then corrected for the Rossiter effect by subtracting the RVs calculated from the unperturbed profiles from the perturbed ones, in our example by subtracting the black curve from the red one. Figure 6.3 shows in its left panels time series of line profiles computed for a sectoral $l=3$ mode at out-of-eclipse and at in-eclipse phases. In the first case we see the distortions introduced by the pulsation as bumps traveling across the line profile. The RVs calculated from the first moment of the line profiles are shown in the right panel. During the eclipse phases, in the result of the timely varying obscuration of the primary, the line profiles are dominated by the sharp line core that moves from blue to red. The right panel shows the RVs after subtracting the RVs measured from the unperturbed profiles at the same eclipse phases. In the result of this subtraction we obtain pure pulsation RV curves. Figure 6.4 shows two examples. In the left panel we see the amplitude amplification of the RV variations during primary eclipse as we found to be typical for all zonal and tesseral modes in the case of a partial eclipse. There is one maximum centered at the time of minimum light. For all the sectoral modes, and only for these, we observe a double-peaked behavior. The
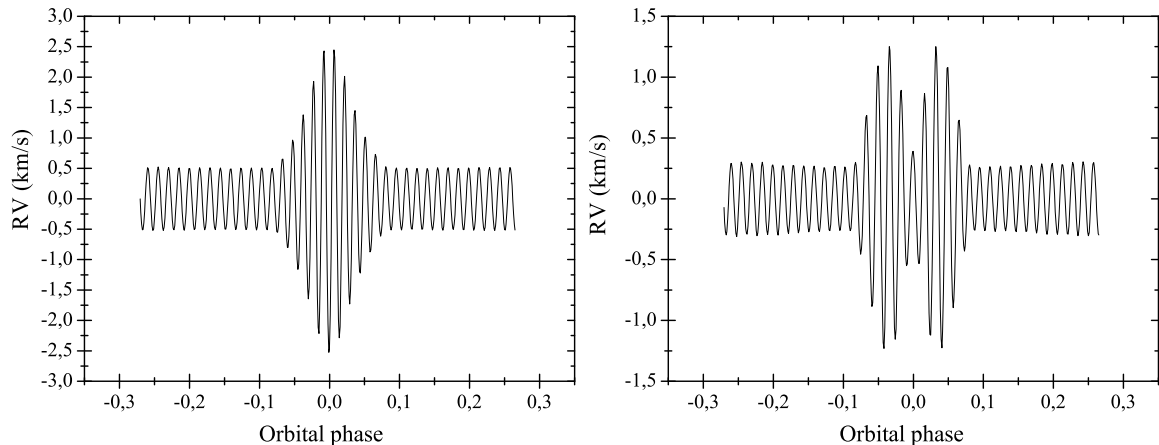
Figure 6.4: RV curves corrected for the Rossiter effect and folded with the orbital period. The primary minimum occurs at phase zero. **Left:** For a zonal (l,m)=(1,0) mode. **Right:** For a sectoral (l,m)=(3,3) mode.

strongest amplification is observed during the first and the last parts of the eclipse outside its central part (Figure 6.4 right).

In practice, we will measure the amplification of the RV variations by determine the RVs from the observed spectra. In this case, we have to compensate for the Rossiter effect in a different way. Lehmann & Mkrtichian (2008a), for instance, did this by removing the distortions by the Rossiter effect by removing nightly trends from the RVs observed for RZ Cas. Such a procedure will work as long as the pulsation period is much shorter than the duration of the eclipse.

In the following, we search for systematic correlations between stellar, system and pulsation parameters and the amplitudes of the oscillation modes. Since RV measurements are only sensitive to low-degree modes, we limit our calculations to $l \leq 4$. The results will be shown for prograde modes $(m > 0)$ only, but they are valid for retrograde modes as well because no dependence on the direction of the propagation was found. To determine the relationship between the amplitudes of the oscillation modes and the fraction of the primary's surface that is obscured by the secondary during the phase of minimum light, we consider three different orbital inclinations of $i = 68°$, $75°$, and $82°$. The last value corresponds to the orbital inclination of RZ Cas. Figure 6.5 gives an impression of the fraction of the visible surface of the primary that is covered by the secondary at the center of the primary eclipse for the three different inclinations.

6.2   Results

As mentioned above, we restricted our calculations to $l \leq 4$. The numerical simulations showed, however, that for l=4 the resulting RV amplitudes at the out-of-eclipse phases are very small and of low accuracy, insufficient to derive reliable amplification factors. Thus we give the results for l=4 only for the eclipse phases, where the corresponding amplitudes are enhanced by the spatial filtration effect and become measurable. Figure 6.6 shows a
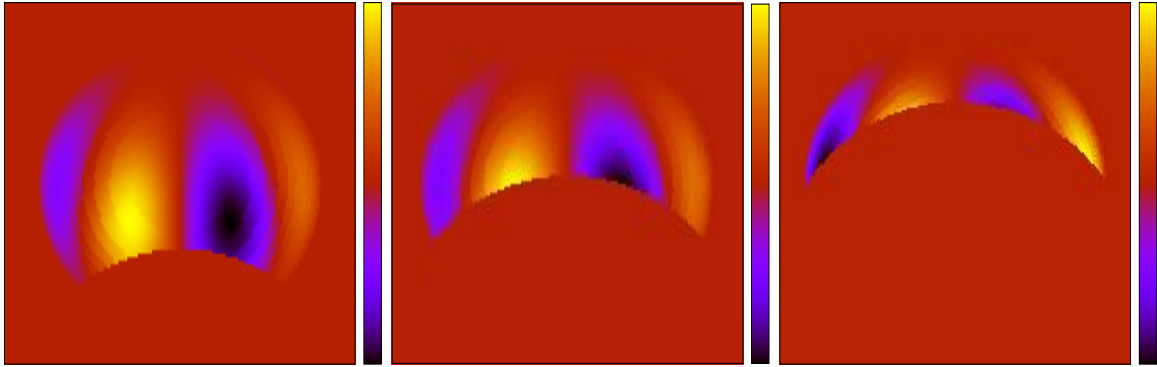
Figure 6.5: The radial velocity field on the surface of the primary for a sectoral $l=4$ mode at the center of the primary eclipse for orbital inclinations of 68°, 75°, and 82° (from left to right).

compilation of the results obtained for different non-radial pulsation modes in dependence on the orbital inclination. It shows in the first row the RV amplitudes calculated at the out-of-eclipse phases. The different (l, m) combinations are marked to the right. The second row shows the maximum amplitudes calculated during the primary eclipse. The third row shows the corresponding amplification factors which we define as the difference between the maximum amplitude during the eclipse and the amplitude at out-of-eclipse phases, normalized to the latter one. The columns represent the results for zonal, sectoral, and tesseral modes (from left to right).

Before we interpret the behavior of the different modes in Figure 6.6, we have to mention that a different inclination of the orbit always also means a different inclination of the rotation axis of the pulsating star. Thus the behavior of the modes in the out-of-eclipse phases for different inclinations of the orbit results only from the different inclinations of the rotation axis of the star. The pulsation amplitudes observed during the eclipses, on the other hand, are influenced by the inclination of the rotation axis as well as by the different fractions of the surface of the primary that are covered by the secondary for different orbital inclinations.

Mkrtichian et al. (2004) showed (see § 1.4.2) that for all eclipsing binaries that are seen nearly equator-on all oscillation modes with $l+|m|=$ odd are smeared out in the disk integrated light which restricts the number of pulsation modes that can be observed at out-of-eclipse phases. Our results confirm this conclusion, as we can see from the first row of Figure 6.6. All modes with odd combinations of l and m show low amplitudes at large inclinations. We further see that the sectoral modes of lowest degree ($l=1$) give rise to the largest amplitudes, followed by the $(l, m)=(2,2)$ mode. All sectoral modes show an increase of the amplitudes with the inclination of the rotation axis, but this increase is only small. Also the zonal $(l, m)=(2,0)$ mode shows this behavior, whereas all the modes with odd l, m combinations behave in the opposite way, the amplitudes decrease with increasing inclination of the rotation axis, confirming the conclusion by Mkrtichian as mentioned before.

Although there are some exceptional cases like the $(l, m)=(2,0)$ mode, one can say that in general the amplitudes outside the eclipse decrease with increasing l, as it is expected from a calculation or observation in the disk-integrated light. For a given l, the sectoral modes show the largest amplitudes if the star is seen nearly equator-on. The behavior is more complex in the case of lower inclinations, where e.g. the $(l, m) = (3, 2)$ mode shows a larger amplitude
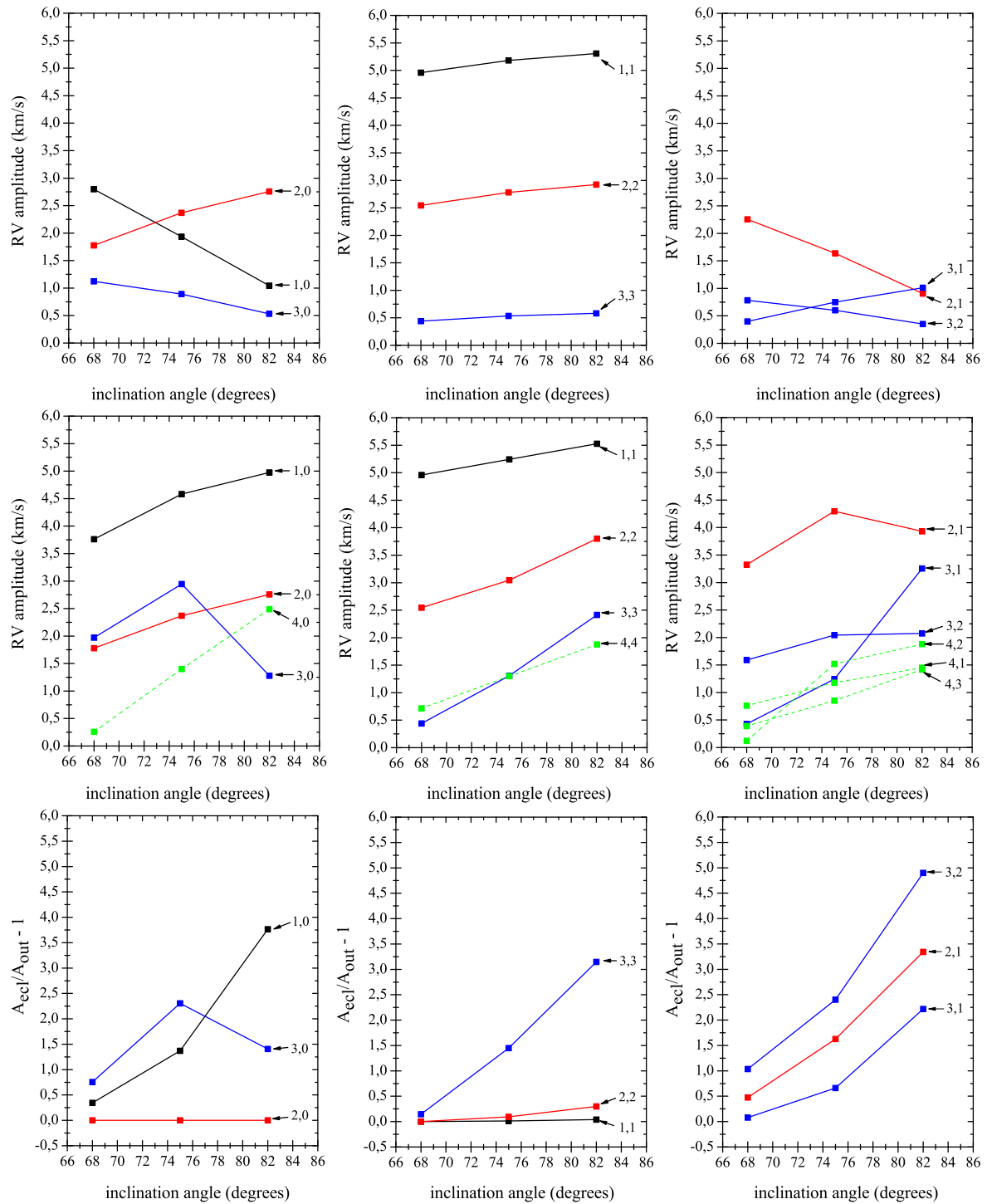
Figure 6.6: RV amplitudes at out-of-eclipse phases (top) and during the eclipses (center row), and the corresponding amplification factors (bottom) versus orbital inclination. The results are shown for zonal, sectoral, and tesseral modes (from left to right).

than the $(l, m) = (3, 3)$ mode.

From Figure 6.6 it can be seen that in most cases the amplification of the RV amplitudes is largest if the star is seen nearly equator-on, which is expected when a larger fraction of the primary's surface is eclipsed by the companion and the spatial filtration effect works more efficiently. Only for the (l, m)=(3,0) mode, the maximum amplification occurs at a lower inclination of $75°$. In the case of the sectoral modes, the l=3 mode which shows the smallest amplitudes outside the eclipse, is the most enhanced one. Such a behavior can also be observed for the modes with odd l, m combinations. These are the weakest modes in the out-of-eclipse phases and show the strongest amplification during the eclipse. Thus, due to the spatial filtration effect, we can detect also non-radial pulsation modes during the eclipse which amplitudes may be below the detection limit outside the eclipse. For that reason we included in the middle row of Figure 6.6 also the l=4 modes, although their amplitudes outside the eclipse are near to zero, which prevented us from calculating reliable amplification factors for these modes.

On the other hand, the appearance of pulsation modes during the eclipse phases that cannot be detected outside the eclipse may complicate an identification of the modes from the observed amplification factors alone. But there are additional possibilities to come to a unique identification. First, we found that only the sectoral modes show the double-peaked behavior in their RV-curves during the eclipse as it is illustrated in the right panel of Figure 6.4. The zonal and tesseral modes show only one peak centered at the phase of minimum light. In this way we detected a unique tool to distinguish the sectoral modes from all other modes. And second, we will have the information from the analysis at the out-of-eclipse phases by the usual mode identification techniques like the moment method (Balona 1986; Briquet & Aerts 2003) or the pixel-by-pixel method (Gies & Kullavanijaya 1988) which are both included in the FAMIAS program package (Zima 2008). One will use in general all possible information available from photometry and spectroscopy and apply a combination of various methods. The investigation of the spatial filtration effect adds on method more and can give additional constraints on the possible l, m combinations.

Finally, we want to mention that we found one mode, the $(l, m) = 2, 0$ mode, that shows no amplification of its RV variation at all, independent of the orbital inclination. The RV oscillations are damped at the very center of the partial eclipse, but not enhanced. Actually, we have no explanation why one of the zonal modes shows such a different behavior.

Chapter 7

Conclusions

Asteroseismology is a young and powerful domain in modern astrophysics allowing for probing the interiors of the stars by the interpretation of the frequencies, amplitudes and phases of their non-radial oscillation modes. Besides a unique mode identification in terms of n, l and m quantum numbers, the precise knowledge of stellar parameters like mass, radius, effective temperature, gravity, and metalicity is needed for a subsequent construction of an asteroseismic model of a star. The best way to get as much information about stellar parameters as possible and to be able to compare the results obtained from two independent methods is to combine spectroscopic and photometric observations. There is a lack of appropriate programs for a complete analysis of spectroscopic data, however. The aim of this work was twofold. First, to establish a computer program that is capable of analyzing the composite spectra of double-lined, eclipsing binaries taken in all orbital phases including the eclipses and of deriving optimized stellar and system parameters from this analysis. And second, to use the program for a detailed investigations of the two oEA stars RZ Cas and TW Dra.

In the first step, we developed the new computer program Shellspec07_inverse that solves the inverse problem of finding stellar and system parameters of eclipsing binaries from observed time-series of high-resolution spectra. Shellspec07_inverse analyses the full information content of the line profiles observed at all orbital phases, including the eclipses. It counts for the non-sphericity of the Roche lobe filling secondary and uses an improved modeling of the gravity and limb darkening effects. The desired parameters like effective temperatures, masses, radii and $v \sin i$ of the components, its separation, or the orbital inclination are calculated by means of a non-linear optimization procedure using a fast version of the Levenberg-Marquardt algorithm. To derive the necessary input parameters, we additionally used the KOREL and the SynthV programs together with the LLmodels code.

The KOREL program delivered precise orbital solutions for both target stars. In the case of RZ Cas, we find that the orbital period increased by (2.0 ± 0.1) s between the two epochs of observations in 2001 and 2006. A significant change in the RV semi-amplitudes of RZ Cas as presumed by Lehmann & Mkrtichian (2008a) could be excluded. The increase of the orbital period can be explained by the transfer of the angular momentum that was stored during the rapid mass transfer episode in 2001 in the accelerated rotation of the outer layers of the primary back to the orbit. No differences could be found between the orbital elements of TW Dra derived from the spectra taken in 2007 and 2008. The advantage of the KOREL program to calculate time-dependent relative line strengths was in particular useful to handle

the unpredictable light contributions of the third component in the spectra of TW Dra. Due to the fact that we had two special spectra of the components at our disposal - the single, observed spectrum of the third component and the spectrum of TW Dra observed during the total eclipse, we could show that our approach of the renormalization of the KOREL output spectra works well. At the same time we really proved, may be for the first time, that the decomposing of spectra with KOREL gives reliable results.

The decomposed spectra of both stars have been analyzed with the SynthV program based on atmosphere models computed with LLmodels for the hot primary components and on MARCS atmosphere models for the cool secondaries. By an iterative adjustment of the atmospheric parameters, in particular of the elemental abundances, to the observed spectra and a recalculation of the atmosphere models we ended up with consistent model atmospheres and synthetic spectra. The obtained fit of the decomposed spectra of the hot primaries of the two stars was almost perfect. In the case of the late-type secondaries, the less precise determined local continuum and the fact that SynthV assumes a spherical configuration of the stars lead to a lower but still reliable quality of the fit. In the result of the abundance analysis we could show that the primary of RZ Cas has abundances that are close to the solar ones. Only silicon is depleted by a factor of 2.5. The secondary of RZ Cas shows an underabundance of Fe and Cr by factors of 3 to 4 and may have a lower metalicity by -0.5 dex compared to the sun. A slightly enhanced metalicity of about +0.15 dex was found for the primary of TW Dra. For the secondary we assumed solar abundances. We can say in general that the primaries of both systems are normal A stars with abundances close to the solar values. In particular, we did not find any λ Boo signatures of the primary of RZ Cas as reported by Narusawa et al. (2006).

The orbital elements derived with KOREL and the stellar parameters obtained from the analysis of the decomposed spectra have been used as starting values for the Shell-spec07_inverse program. By means of this program we fine-tuned the stellar and system parameters based on the observed composite spectra of the spectroscopic binaries in all orbital phases and taking the non-spherical shapes of the Roche-lobe filling secondaries and the resulting gravity darkening into account. Whereas the spectra of TW Dra could be well fitted by assuming a value of the gravity darkening exponent of β=0.08 as predicted for a star with a convective envelope (Lucy 1967), we had to use for the hemisphere of RZ Cas that points toward the primary the ultra-high value of β=0.5. The latter finding partly confirms the results by Varricatt et al. (1998), who derived for RZ Cas β=0.56 as a global value from photometry. On the other hand, such a high value cannot be interpreted in terms of some unusual gravity darkening. Our interpretation is that the secondary of RZ Cas exhibits a large cool and dark spot centered on its surface at the inner Lagrangian point, as already pointed out by Unno et al. (1994). The authors calculated that cool dark spots should appear in the low-gravity surface regions of the secondary of Algol-type systems in the result of the enthalpy transport via the inner Lagrangian point. They expected two spots in this way, one pointing toward the primary, and the other on the opposite side. According to our results, RZ Cas shows only one such spot pointing toward the primary, both in its quiet state in 2006 and in its active phase in 2001. No hints to any unusual gravity darkening were found for TW Dra.

Our usage of the two-dimensional O–C line intensity residual distributions shown in § 4.3.1

and Section 5.4 was twofold. First, we used the integrated value as a measure of the goodness of the fit. And second, the two-dimensional representation allowed us to see all the effects that were not covered by our model. In the case of TW Dra we ended up with very smooth fits for both epochs of observations in 2007 and 2008, pointing to quiet states of the system in both years. The same result we obtained from the analysis of the spectra of RZ Cas taken in 2006. In all these cases it was not necessary to include Algol-typically effects like a gas stream or an accretion annulus into the calculations to improve the results. When we applied the model obtained for RZ Cas from 2006 to the spectra from 2001, however, we saw that the model does not fit the observations. Although the results could be improved by introducing an accretion annulus of varying density into the calculations, orbital phase dependent structures in the O–C distribution remained. This result confirms the assumption by Lehmann & Mkrtichian (2008a) that RZ Cas was observed in 2001 in or shortly after an episode of rapid mass transfer, leading to a complex distribution of circumbinary matter that cannot be explained by our simple model.

In most cases, the finally obtained stellar and system parameters agree well with those previously found from photometry. In the case of RZ Cas, the mass of the primary and the separation of the components are slightly smaller, whereas the temperatures of both components are higher. All other system parameters agree with at least one of the previous determinations. For the primary, we deduce a spectral type of A2 V. Based on our results obtained from the analysis of the decomposed spectrum of RZ Cas as well as from Shellspec07_inverse we can exclude the lower temperatures that lead to spectral type A3 as derived by the other authors. Because of the large cool spot, expressed in our model by the ultra-high gravity darkening exponent, we can not define a spectral type for the secondary. The derived effective temperature at the pole of 4 800 K would correspond to spectral type G8 III.

Comparing the values of the rotational period of the primary derived from the radius and the $v \sin i$ with the orbital period, we find, within the errors of measurement, that the primary of RZ Cas rotates synchronously, the synchronization factor follows to 1.00±0.01. For TW Dra, we obtain about the same accuracy in deriving the synchronization factor and can show that its rotational angular velocity is (1.07±0.01) times faster than the orbital one.

For TW Dra, all spectroscopically derived parameters agree very well with those from the most recent photometric investigation by Zejda et al. (2010) using the Wilson-Devinney program. In cases of the radius of the primary and the orbital inclination, we reach the same accuracy as obtained from photometry. For the masses and the mass ratio, the derived errors are about twice the photometric errors. According to the obtained stellar parameters, the primary of TW Dra is a slightly evolved A5 V star and the secondary a K1 IV subgiant.

The results of the analysis of the two oEA stars using the newly developed computer program Shellspec07_inverse showed that the stellar and system parameters can be derived with high accuracy, comparable to that achieved with the WD code from the light curve analysis. A necessary precondition was, of course, that we had extended time-series of high-resolution spectra of a good orbital phase coverage at our disposal. This fact encouraged us to think about a further development of the program by including the line profile perturbations due to the non-radial pulsations with the aim to derive the stellar and system parameters together with the amplitudes, phases, and l, m wavenumbers of the pulsations from the observed spec-

tra. Actually, the available computer power (single PCs using a LINUX platform) is not sufficient to realize such a project, however. Nevertheless, we did a first attempt to check for the influence of the pulsations onto the computed line profiles by restricting our calculations to a simple model, including only the radial velocity field perturbations due to the non-radial pulsations and did not try to solve the inverse problem of the determination of the parameters from the observations. After some attempts to show the influence of the spatial filtration effect on the oscillations observed in the light curves of pulsating eclipsing binaries (e.g., Gamarova et al. (2003), Rodriguez et al. (2004a), Reed et al. (2005)), our spectroscopic investigation is the first systematic search for similar effects in the line profiles.

In the result of the numerical simulations we find relationships between the RV amplitudes in the out-of-eclipse and eclipse phases and the different non-radial pulsation modes in dependence on the inclinations of the rotation axis and the orbital plane. Our most important finding is that the modes that show the lowest amplitudes outside the eclipse are most amplified by the spatial filtration effect during the eclipses. We conclude that we can observe in this way non-radial pulsation modes during the eclipses whose amplitudes are normally below the detection limit. This is in particular the case for the oscillation modes with $l + |m| = $ odd. Their influence on the line profiles is smeared out in the disk-integrated light outside the eclipses as also found by Mkrtichian et al. (2004) but strongly amplified during the eclipse phases if the primary is seen nearly equator-on.

A unique identification of the non-radial pulsation modes is one of the basic preconditions for a successful asteroseismic modeling of the stars. The spatial filtration effect observed in oscillating Algol-type stars allows to constrain the number of possible oscillation modes in terms of l, m numbers considerably. We have found that only the sectoral modes give rise to a double-peaked amplification feature in the RV curves centered at the primary minimum while the zonal and tesseral modes produce only a single peak. Thus both the shape of the envelope of the RV curve and the mode-typical values of the RV amplitude amplification factor during the eclipse that we derived in dependence on the l, m wavenumbers can be used for a mode identification.

The results of this work, in particular the high accuracy obtained for the spectroscopically derived stellar and system parameters and the possibilities offered by the spatial filtration effect in investigating the stellar pulsations of eclipsing binaries encouraged us to think about a further development of the Shellspec07_inverse program in the future. We plan to apply different improvements. One is to derive the parameters of the non-radial pulsations like intrinsic velocity amplitudes, phases, and the l, m wavenumbers together with the stellar and system parameters from the observed time series of spectra. For that we have to treat the effect of the pulsations on the line profiles in a more physical way by including the surface temperature and area perturbations into the calculations. And we do not want to use computed RVs but compare the calculated line profiles directly with the observed ones. For this task we need line profiles of high S/N which we want to obtain from the calculation of least-squares deconvolved (LSD, Donati et al. (1997)) profiles from the observed spectra. The usage of such mean profiles together with the orbital phase binning will enhance the S/N drastically and even high-degree l modes will become measurable, as could be shown by Lehmann et al. (2009) in the case of TW Dra. To be able to compute the required large number of line profiles in a reasonable time the Shellspec07_inverse program will be

parallelized to run it on a cluster PC that will be available in next time at the Thüringer Landessternwarte. We plan to apply the improved Shellspec07_inverse program to oEA stars as well as to spectra of brighter eclipsing binaries detected by the Kepler space satellite to add the urgently needed spectroscopic information to its high-accuracy photometric data.

Bibliography

Acknowledgements

Ehrenwörtliche Erklärung

Ich erkläre hiermit ehrenwörtlich, dass ich die vorliegende Arbeit selbständig, ohne unzulässige Hilfe Dritter und ohne Benutzung anderer als der angegebenen Hilfsmittel und Literatur angefertigt habe. Die aus anderen Quellen direkt oder indirekt übernommenen Daten und Konzepte sind unter Angabe der Quelle gekennzeichnet.

Bei der Auswahl und Auswertung folgenden Materials haben mir die nachstehend aufgeführten Personen in der jeweils beschriebenen Weise unentgeldlich geholfen:

- Dr. Holger Lehmann: Betreuung der vorliegenden Arbeit

- Dr. Denis Shulyak: Unterstützung bei der Anwendung des Rechnerprogramms LLModels.

- Prof. Vadim Tsymbal: Unterstützung bei der der Anwendung des Rechnerprogramms SynthV.

Weitere Personen waren an der inhaltlich-materiellen Erstellung der vorliegenden Arbeit nicht beteiligt. Insbesondere habe ich hierfür nicht die entgeltliche Hilfe von Vermittlungs bzw. Beratungsdiensten (Promotionsberater oder andere Personen) in Anspruch genommen. Niemand hat von mir unmittelbar oder mittelbar geldwerte Leistungen für Arbeiten erhalten, die in Zusammenhang mit dem Inhalt der vorgelegten Dissertation stehen.

Die Arbeit wurde bisher weder im In- noch im Ausland in gleicher oder ähnlicher Form einer anderen Prüfungsbehörde vorgelegt.

Die geltende Promotionsordnung der Physikalisch-Astronomischen Fakultät ist mir bekannt.

Ich versichere ehrenwörtlich, dass ich nach bestem Wissen die reine Wahrheit gesagt und nichts verschwiegen habe.

Tautenburg, den 29. März 2010   Andrii Tkachenko

Lebenslauf

Zur Person:

Name: Tkachenko
Vorname: Andrii
Geburtsdatum: 03.09.1985
Geburtsort: Simferopol (Ukraine)

Werdegang:

seit Oktober 2007:	Doktorand an der Thüringer Landessternwarte Tautenburg
	Betreuer: Prof. Dr. Artie Hatzes
	Titel: Spectroscopic analysis of oscillating Algol-type stars
Sept. 2002 - June 2007	Physikstudium und Diplomarbeit an der Taurian National University in Simferopol (Ukraine)
	Betreuer: Prof. Dr. Vadim Tsymbal
	Titel: Doppler imaging analysis of the helium-weak silicon star HR 7224
	Abschluß: Master of Science
Sep. 1992 - June 2002	Schulbesuch in Simferopol (Ukraine)
	Abschluß: Hochschulzugangsberechtigung

Tautenburg, den 29. März 2010   Andrii Tkachenko

List of publications

1. Lehmann, H., **Tkachenko, A.**, Fraga, L., Tsymbal, V., Mkrtichian, D. E.: *The helium weak silicon star HR 7224. II. Doppler Imaging analysis*, 2007, Astronomy and Astrophysics, 471, 941

2. Lehmann, H., Mkrtichian, D., **Tkachenko, A.**: *Spectroscopic eclipse mapping of oEA stars*, 2008, Journal of Physics: Conference Series, 118, 2062

3. Lehmann, H., **Tkachenko, A.**, Tsymbal, V., Mkrtichian, D. E.: *The oEA star TW Dra – a spectroscopic analysis*, 2008, Communications in Asteroseismology, 157, 332

4. **Tkachenko, A.**, Lehmann, H., Tsymbal, V., Mkrtichian, D.: *Spectroscopic solution for the oEA star RZ Cas using the SHELLSPEC code*, 2008, Communications in Asteroseismology, 157, 377

5. **Tkachenko, A.**, Lehmann, H., Tsymbal, V., Mkrtichian, D. E.: *Ultra-High Gravity Darkening in the oEA Star RZ Cas*, 2008, YSC'15 Proceedings of Contributed Papers, p.33

6. Lehmann, H., **Tkachenko, A.**, Mkrtichian, D. E.: *TW Dra: NRP mode identification with FAMIAS*, 2009, Communications in Asteroseismology, 159, 45

7. **Tkachenko, A.**, Lehmann, H., Mkrtichian, D. E.: *Spectroscopic modeling of oscillating Algol-type stars: I. RZ Cassiopeia*, 2009, Astronomy and Astrophysics, 504, 991

8. **Tkachenko, A.**, Lehmann, H., Mkrtichian, D. E.: *Spectroscopic modeling of the Algol-type star TW Draconis*, 2010, Astronomical Journal, 139, 1327

Talks

I presented the following talks:

1. 2007, June 17-23, international conference "Physics of stellar atmospheres: chemical composition, magnetics and surface inhomogeneities", Crimean Astrophysical Observatory (Ukraine), "Doppler Imaging analysis of the helium weak silicon star HR 7224"

2. 2008, February 1, Dr. Remeis-Sternwarte Bamberg (Germany), "Doppler Imaging analysis of the helium weak silicon star HR 7224"

3. 2008, April 14-19, international conference "15-th Young Scientists' Conference on Astronomy and Space Physics", Department of Astronomy & Space Physics of National Taras Shevchenko University of Kyiv (Ukraine), "Ultra-high gravity darkening in the oEA star RZ Cas".

4. 2009, May 29, Thüringer Landessternwarte Tautenburg (Germany), "A new computer program for the analysis of eclipsing binary stars and its application to oscillating Algols".